

Jordan Journal of P H Y S I C S

An International Peer-Reviewed Research Journal

Volume 13, No. 1, April 2020, Ramadan 1441 H

Jordan Journal of Physics (JJP): An International Peer-Reviewed Research Journal funded by the Scientific Research Support Fund, Jordan, and published biannually by the Deanship of Research and Graduate Studies, Yarmouk University, Irbid, Jordan.

EDITOR-IN-CHIEF:

Ibrahim O. Abu Al-Jarayesh

Department of Physics, Yarmouk University, Irbid, Jordan.

ijarayesh@yu.edu.jo

EDITORIAL BOARD:	ASSOCIATE EDITORIAL BOARD
<p>Prof. Nabil Y. Ayoub <i>President, American University of Madaba, Madaba, Jordan.</i> nabil.ayoub@ju.edu.jo</p> <p>Prof. Jamil M. Khalifeh <i>Department of Physics, University of Jordan, Amman, Jordan.</i> jkhalifa@ju.edu.jo</p> <p>Prof. Tareq F. Hussein <i>Department of Physics, The University of Jordan, Amman, Jordan.</i> t.hussein@ju.edu.jo</p> <p>Prof. Marwan S. Mousa <i>Department of Physics, Mu'tah University, Al-Karak, Jordan.</i> mmousa@mutah.edu.jo</p> <p>Prof. Mohammad Al-Sugheir <i>Department of Physics, The Hashemite University, Zarqa, Jordan.</i> msugheir@hu.edu.jo</p> <p>Prof. Abdalmajeid M. Alyassin <i>Department of Physics, Yarmouk University, Irbid, Jordan.</i> alyassin@yu.edu.jo</p> <p>Prof. M-Ali H. Al-Akhras (AL-Omari) <i>Department of Physics, Jordan University of Science & Technology, Irbid, Jordan.</i> alakmoh@just.edu.jo</p> <p>Prof. Ibrahim A. Bsoul <i>Department of Physics, Al al-Bayt University, Mafrqa, Jordan.</i> Ibrahimbsoul@yahoo.com</p>	<p>Prof. Mark Hagmann <i>Desert Electronics Research Corporation, 762 Lacey Way, North Salt Lake 84064, Utah, U. S. A.</i> MHagmann@NewPathResearch.Com</p> <p>Dr. Richard G. Forbes <i>Dept. of Electrical and Electronic Engineering, University of Surrey, Advanced Technology Institute and Guildford, Surrey GU2 7XH, UK.</i> r.forbes@surrey.ac.uk</p> <p>Prof. Roy Chantrell <i>Physics Department, The University of York, York, YO10 5DD, UK.</i> roy.chantrell@york.ac.uk</p> <p>Prof. Susamu Taketomi <i>2-35-8 Higashisakamoto, Kagoshima City, 892-0861, Japan.</i> staketomi@hotmail.com</p>

Editorial Secretary: Majdi Al-Shannaq.

Languages Editor: Haider Al-Momani

Manuscripts should be submitted to:

Prof. Ibrahim O. Abu Al-Jarayesh
Editor-in-Chief, Jordan Journal of Physics
Deanship of Research and Graduate Studies
Yarmouk University-Irbid-Jordan
Tel. 00 962 2 7211111 Ext. 2075
E-mail: jjp@yu.edu.jo
Website: <http://Journals.yu.edu.jo/jjp>

Jordan Journal of P H Y S I C S

An International Peer-Reviewed Research Journal

Volume 13, No. 1, April 2020, Ramadan 1441 H

INTERNATIONAL ADVISORY BOARD

Prof. Dr. Ahmad Saleh

Department of Physics, Yarmouk University, Irbid, Jordan.
salema@yu.edu.jo

Prof. Dr. Aurore Savoy-Navarro

LPNHE Université de Paris 6/IN2P3-CNRS, Tour 33, RdC 4,
Place Jussieu, F 75252, Paris Cedex 05, France.
auore@lphnhep.in2p3.fr

Prof. Dr. Bernard Barbara

Laboratoire Louis Neel, Salle/Room: D 108, 25, Avenue des
Martyrs BP 166, 38042-Grenoble Cedex 9, France.
Barbara@grenoble.cnrs.fr

Prof. Dr. Bruno Guiderdoni

Observatoire Astronomique de Lyon, g, avenue Ch. Antre-F-69561,
Saint Genis Laval Cedex, France.
Bruno.guiderdoni@olos.univ-lyon1.fr

Prof. Dr. Buford Price

Physics Department, University of California, Berkeley, CA 94720,
U. S. A.
bprice@berkeley.edu

Prof. Dr. Colin Cough

School of Physics and Astronomy, University of Birmingham, B15
2TT, U. K.
c.cough@bham.ac.uk

Prof. Dr. Desmond Cook

Department of Physics, Condensed Matter and Materials Physics
Research Group, Old Dominion University, Norfolk, Virginia
23529, U. S. A.
Dcook@physics.odu.edu

Prof. Dr. Evgeny Sheshin

MIPT, Institutskij per. 9, Dogoprudnyi 141700, Russia.
sheshin@lafaet.mipt.ru

Prof. Dr. Hans Ott

Laboratorium fuer Festkorperphysik, ETH Honggerberg, CH-
8093 Zurich, Switzerland.
ott@solid.phys.ethz.ch

Prof. Dr. Herwig Schopper

President SESAME Council, Chairman Scientific Board UNESCO
IBSP Programme, CERN, 1211 Geneva, Switzerland.
Herwig.Schopper@cern.ch

Prof. Dr. Humam Ghassib

Department of Physics, The University of Jordan, Amman 11942,
Jordan.
humamg@ju.edu.jo

Prof. Dr. Khalid Tougan

Chairman of Jordan Atomic Energy Commission, Amman, Jordan.

Prof. Dr. Nasr Zubeidev

President: Al-Zaytoonah University of Jordan, Amman, Jordan.
President@alzaytoonah.edu.jo

Prof. Dr. Patrick Roudeau

Laboratoire de l'Accelérateur, Lineaire (LAL), Université Paris-
Sud 11, Batiment 200, 91898 Orsay Cedex, France.
roudeau@mail.cern.ch

Prof. Dr. Paul Chu

Department of Physics, University of Houston, Houston, Texas
77204-5005, U. S. A.
Ching-Wu.Chu@mail.uh.edu

Prof. Dr. Peter Dowben

Nebraska Center for Materials and Nanoscience, Department of
Physics and Astronomy, 255 Behlen Laboratory (10th and R
Streets), 116 Brace Lab., P. O. Box 880111, Lincoln, NE 68588-
0111, U. S. A.
pdowben@unl.edu

Prof. Dr. Peter Mulser

Institute fuer Physik, T.U. Darmstadt, Hochschulstr. 4a, 64289
Darmstadt, Germany.
Peter.mulser@physik.tu-darmstadt.de

Prof. Dr. Rasheed Azzam

Department of Electrical Engineering, University of New Orleans
New Orleans, Louisiana 70148, U. S. A.
razzam@uno.edu

Prof. Dr. Shawqi Al-Dallal

Department of Physics, Faculty of Science, University of Bahrain,
Manamah, Kingdom of Bahrain.

Prof. Dr. Wolfgang Nolting

Institute of Physics / Chair: Solid State Theory, Humboldt-
University at Berlin, Newtonstr. 15 D-12489 Berlin, Germany
Wolfgang.nolting@physik.hu-berlin.de

Prof. Dr. Ingo Hofmann

GSI Darmstadt, Planckstr. 1, 64291, Darmstadt, Germany.
i.hofmann@gsi.de

Prof. Dr. Jozef Lipka

Department of Nuclear Physics and Technology, Slovak University
of Technology, Bratislava, Ilkovicova 3, 812 19 Bratislava,
Slovakia.
Lipka@elf.stuba.sk



The Hashemite Kingdom of Jordan



Yarmouk University

Jordan Journal of PHYSICS

An International Peer-Reviewed Research Journal
Funded by the Scientific Research Support Fund

Volume 13, No. 1, April 2020, Ramadan 1441 H

Instructions to Authors

Instructions to authors concerning manuscript organization and format apply to hardcopy submission by mail, and also to electronic online submission via the Journal homepage website (<http://jjp.yu.edu.jo>).

Manuscript Submission

1- **E-mail to :** jjp@yu.edu.jo

2- **Online:** Follow the instructions at the journal homepage website.

Original *Research Articles*, *Communications* and *Technical Notes* are subject to critical review by minimum of two competent referees. Authors are encouraged to suggest names of competent reviewers. *Feature Articles* in active Physics research fields, in which the author's own contribution and its relationship to other work in the field constitute the main body of the article, appear as a result of an invitation from the Editorial Board, and will be so designated. The author of a *Feature Article* will be asked to provide a clear, concise and critical status report of the field as an introduction to the article. *Review Articles* on active and rapidly changing Physics research fields will also be published. Authors of *Review Articles* are encouraged to submit two-page proposals to the Editor-in-Chief for approval. Manuscripts submitted in *Arabic* should be accompanied by an Abstract and Keywords in English.

Organization of the Manuscript

Manuscripts should be typed double spaced on one side of A4 sheets (21.6 x 27.9 cm) with 3.71 cm margins, using Microsoft Word 2000 or a later version thereof. The author should adhere to the following order of presentation: Article Title, Author(s), Full Address and E-mail, Abstract, PACS and Keywords, Main Text, Acknowledgment. Only the first letters of words in the Title, Headings and Subheadings are capitalized. Headings should be in **bold** while subheadings in *italic* fonts.

Title Page: Includes the title of the article, authors' first names, middle initials and surnames and affiliations. The affiliation should comprise the department, institution (university or company), city, zip code and state and should be typed as a footnote to the author's name. The name and complete mailing address, telephone and fax numbers, and e-mail address of the author responsible for correspondence (designated with an asterisk) should also be included for official use. The title should be carefully, concisely and clearly constructed to highlight the emphasis and content of the manuscript, which is very important for information retrieval.

Abstract: A one paragraph abstract not exceeding 200 words is required, which should be arranged to highlight the purpose, methods used, results and major findings.

Keywords: A list of 4-6 keywords, which expresses the precise content of the manuscript for indexing purposes, should follow the abstract.

PACS: Authors should supply one or more relevant PACS-2006 classification codes, (available at <http://www.aip.org/pacs/pacs06/pacs06-toc.html>)

Introduction: Should present the purpose of the submitted work and its relationship to earlier work in the field, but it should not be an extensive review of the literature (e.g., should not exceed 1 ½ typed pages).

Experimental Methods: Should be sufficiently informative to allow competent reproduction of the experimental procedures presented; yet concise enough not to be repetitive of earlier published procedures.

Results: should present the results clearly and concisely.

Discussion: Should be concise and focus on the interpretation of the results.

Conclusion: Should be a brief account of the major findings of the study not exceeding one typed page.

Acknowledgments: Including those for grant and financial support if any, should be typed in one paragraph directly preceding the References.

References: References should be typed double spaced and numbered sequentially in the order in which they are cited in the text. References should be cited in the text by the appropriate Arabic numerals, enclosed in square brackets. Titles of journals are abbreviated according to list of scientific periodicals. The style and punctuation should conform to the following examples:

1. Journal Article:

- a) Heisenberg, W., Z. Phys. 49 (1928) 619.
- b) Bednorz, J. G. and Müller, K. A., Z. Phys. B64 (1986) 189
- c) Bardeen, J., Cooper, L.N. and Schrieffer, J. R., Phys. Rev. 106 (1957) 162.
- d) Asad, J. H., Hijjawi, R. S., Sakaji, A. and Khalifeh, J. M., Int. J. Theor. Phys. 44(4) (2005), 3977.

2. Books with Authors, but no Editors:

- a) Kittel, C., "Introduction to Solid State Physics", 8th Ed. (John Wiley and Sons, New York, 2005), chapter 16.
- b) Chikazumi, S., C. D. Graham, JR, "Physics of Ferromagnetism", 2nd Ed. (Oxford University Press, Oxford, 1997).

3. Books with Authors and Editors:

- a) Allen, P. B. "Dynamical Properties of Solids", Ed. (1), G. K. Horton and A. A. Maradudin (North-Holland, Amsterdam, 1980), p137.
- b) Chantrell, R. W. and O'Grady, K., "Magnetic Properties of Fine Particles" Eds. J. L. Dormann and D. Fiorani (North-Holland, Amsterdam, 1992), p103.

4. Technical Report:

Purcell, J. "The Superconducting Magnet System for the 12-Foot Bubble Chamber", report ANL/HEP6813, Argonne Natl. Lab., Argonne, III, (1968).

5. Patent:

Bigham, C. B., Schneider, H. R., US patent 3 925 676 (1975).

6. Thesis:

Mahmood, S. H., Ph.D. Thesis, Michigan State University, (1986), USA (Unpublished).

7. Conference or Symposium Proceedings:

Blandin, A. and Lederer, P. Proc. Intern. Conf. on Magnetism, Nottingham (1964), P.71.

8. Internet Source:

Should include authors' names (if any), title, internet website, URL, and date of access.

9. Prepublication online articles (already accepted for publication):

Should include authors' names (if any), title of digital database, database website, URL, and date of access.

For other types of referenced works, provide sufficient information to enable readers to access them.

Tables: Tables should be numbered with Arabic numerals and referred to by number in the Text (e.g., Table 1). Each table should be typed on a separate page with the legend above the table, while explanatory footnotes, which are indicated by superscript lowercase letters, should be typed below the table.

Illustrations: Figures, drawings, diagrams, charts and photographs are to be numbered in a consecutive series of Arabic numerals in the order in which they are cited in the text. Computer-generated illustrations and good-quality digital photographic prints are accepted. They should be black and white originals (not photocopies) provided on separate pages and identified with their corresponding numbers. Actual size graphics should be provided, which need no further manipulation, with lettering (Arial or Helvetica) not smaller than 8 points, lines no thinner than 0.5 point, and each of uniform density. All colors should be removed from graphics except for those graphics to be considered for publication in color. If graphics are to be submitted digitally, they should conform to the following minimum resolution requirements: 1200 dpi for black and white line art, 600 dpi for grayscale art, and 300 dpi for color art. All graphic files must be saved as TIFF images, and all illustrations must be submitted in the actual size at which they should appear in the journal. Note that good quality hardcopy original illustrations are required for both online and mail submissions of manuscripts.

Text Footnotes: The use of text footnotes is to be avoided. When their use is absolutely necessary, they should be typed at the bottom of the page to which they refer, and should be cited in the text by a superscript asterisk or multiples thereof. Place a line above the footnote, so that it is set off from the text.

Supplementary Material: Authors are encouraged to provide all supplementary materials that may facilitate the review process, including any detailed mathematical derivations that may not appear in whole in the manuscript.

Revised Manuscript and Computer Disks

Following the acceptance of a manuscript for publication and the incorporation of all required revisions, authors should submit an original and one more copy of the final disk containing the complete manuscript typed double spaced in Microsoft Word for Windows 2000 or a later version thereof. All graphic files must be saved as PDF, JPG, or TIFF images.

Allen, P.B., “.....”, in: Horton, G.K., and Muradudin, A. A., (eds.), “Dynamical.....”, (North.....), pp....

Reprints

Twenty (20) reprints free of charge are provided to the corresponding author. For orders of more reprints, a reprint order form and prices will be sent with the article proofs, which should be returned directly to the Editor for processing.

Copyright



Submission is an admission by the authors that the manuscript has neither been previously published nor is being considered for publication elsewhere. A statement transferring copyright from the authors to Yarmouk University is required before the manuscript can be accepted for publication. The necessary form for such transfer is supplied by the Editor-in-Chief. Reproduction of any part of the contents of a published work is forbidden without a written permission by the Editor-in-Chief.

Disclaimer

Opinions expressed in this Journal are those of the authors and neither necessarily reflects the opinions of the Editorial Board or the University, nor the policy of the Higher Scientific Research Committee or the Ministry of Higher Education and Scientific Research. The publisher shoulders no responsibility or liability whatsoever for the use or misuse of the information published by JJP.

Indexing

JJP is currently indexing in:

	Emerging Sources Citation Index (ESCI)	 ULRICHSWEB™ GLOBAL SERIALS DIRECTORY
---	---	--

Jordan Journal of P H Y S I C S

An International Peer-Reviewed Research Journal

Volume 13, No. 1, April 2020, Ramadan 1441 H

Table of Contents:

Articles	Pages
Structural and Magnetic Properties of (Mg, Co)₂W Hexaferrites	
S. H. Mahmood, Q. Al Sheyab, I. Bsoul, Y. Maswadeh, Q.I. Mohaidat and A. Awadallah	1-16
Chemical Characterization of Harmattan Dust across Oyo and Minna, Nigeria	17-28
O. A. Falaiye and F. O. Aweda	
Physical Properties of RhCrZ (Z= Si, Ge, P, As) Half-Heusler Compounds: A First-Principles Study	29-46
B. Amrani, A. Chahed, M. Rahmoune, K. Benkaddour and A. Sayede	
Dark Matter: Could It Be Vacuum Viscosity?	47-57
M. B. Altaie, N. R. Suleiman and N. M. Ershaidat	
Solution of the Hamilton – Jacobi Equations in an Electromagnetic Field Using Separation of Variables Method – Staeckel Boundary Conditions	59-65
B. M. Al-Khamiseh, R. S. Hijjawi and J. M. Khalifeh	
Reformulation of Degasperis-Procesi Field by Functional Derivatives	67-72
Y. M. Alawaideh, R. S. Hijjawi and J. M. Khalifeh	
Assessment of Natural Radionuclides in Local and Imported Cements in Erbil Governorate, Kurdistan Region- Iraq	73-77
Ali H. Ahmed, Adeeb O. Jafir and Hallo M. Abdullah	
Thermoelectric Properties of ALiF₃ (A= Ca, Sr and Ba): First-Principles Calculation	79-86
Nada T. Mahmoud, Ahmad A. Mousa and J. M. Khalifeh	
Technical Note	Pages
High Efficiency of Solar Cell Model Based on Two Types of Nanoparticles	87-92
Kholoud Kh. Abushaar, Mohammed M. Shabat, Dena M. El-Amassi and Daniel M. Schaadt	

Structural and Magnetic Properties of (Mg, Co)₂W Hexaferrites

S. H. Mahmood^a, Q. Al Sheyab^a, I. Bsoul^b, Y. Maswadeh^c, Q.I. Mohaidat^d
and A. Awadallah^a

^a Physics Department, The University of Jordan, Amman 11942, Jordan.

^b Physics Department, Al al-Bayt University, Al-Mafraq 13040, Jordan.

^c Central Michigan University, Mount Pleasant 48859, Michigan, USA.

^d Physics Department, Yarmouk University, Irbid 21163, Jordan.

Received on: 11/07/2019;

Accepted on: 2/9/2019

Abstract: Precursor powders of BaMg_{2-x}Co_xFe₁₆O₂₇ with ($x = 0.0, 1.0$, and 2.0) were prepared using high-energy ball milling and the effects of chemical composition and sintering temperature on the structural and magnetic properties were investigated using x-ray diffractometer (XRD), scanning electron microscopy (SEM) and vibrating sample magnetometry (VSM). XRD patterns of the prepared samples indicated that crystallization of pure BaW hexaferrite phase was achieved at a sintering temperature of 1300°C , while BaM and cubic spinel intermediate phases were obtained at lower sintering temperatures of 1100°C and 1200°C . SEM images revealed an improvement of crystallization of the structural phases and a growth of the particle size with increasing the sintering temperature. The magnetic data of the samples sintered at 1300°C revealed an increase of the saturation magnetization from 59.4 emu/g to 72.6 emu/g with increasing Co concentration (x) from 0.0 to 2.0 . The coercive field H_c decreased from 0.07 kOe at $x = 0.0$ to 0.03 kOe at $x = 1.0$ and then increased to 0.09 kOe at $x = 2.0$. The thermomagnetic curves of the samples sintered at 1300°C confirmed the existence of the W-type phase and revealed spin reorientation transitions in Co-containing samples.

Keywords: W-type hexaferrites, Magnetic properties, Structural properties, Thermomagnetic measurements, Spin reorientation transition.

Introduction

Hexagonal ferrites, also known as hexaferrites, were discovered in the 1950s at Philips Research Laboratories. Since then, the degree of interest in these ferrites has been increasing exponentially due to their cost effectiveness and suitability for a wide range of industrial and technological applications [1-8]. Different types of these ferrites, the most important of which are the M-, Y-, W-, Z-, X- and U-type, were successfully synthesized and found to exhibit large variations of magnetic properties due to differences in their magnetic structures and magnetocrystalline anisotropy [2,

9-14]. Structurally, all these ferrites are hexagonal with almost the same lattice parameter $a = 5.88\text{ \AA}$ and significantly different lattice parameter c , depending on the sequence of stacking of the structural blocks (S, R, and T) in the unit cell [9, 15]. Specifically, the c -parameter for M-type barium hexaferrite with the chemical formula of BaFe₁₂O₁₉ and unit cell composed of RSR*S* stacking is typically 23.2 \AA . On the other hand, the c -parameter for W-type hexaferrite with the chemical formula BaMe₂Fe₁₆O₂₇, space group P6₃/mmc and RSSR*S*S* stacking is 32.8 \AA [9, 16].

The W-type structure suggests that its unit cell can be represented by a combination of M-type unit cell and two spinel (S) structural blocks ($S = \text{Me}_2\text{Fe}_4\text{O}_8$), where the saturation magnetization can be derived from the superposition of the saturation magnetization of $M + 2S$. Accordingly, the saturation magnetization of W-type is expected to be higher than that of M-type hexaferrite of $20 \mu_B$ per formula unit (corresponding to ~ 100 emu/g) at 0 K [17]. In BaW ferrite, the additional S block has the composition $[\text{Me}_2\text{Fe}_4\text{O}_8]^0$, which is electrically neutral and has a net magnetization depending on the Me cation. For example, the experimental value of Fe_2W is $27.4 \mu_B$ (corresponding to 98 emu/g at 0 K and 78 emu/g at 293 K), which is in good agreement with the theoretical value of $28 \mu_B$. Also, the magnetic moment of Mg_2W at 0 K is expected to be equal

to that of BaM, since the magnetic moment of $\text{Mg}_2\text{Fe}_4\text{O}_8$ is theoretically zero, while the moment of Cu_2W is expected to be higher ($22 \mu_B$). The observed deviations of the experimental values from the theoretical values could be due to Me ions occupying sites of the R block and performing measurements at fields lower than required for full magnetic saturation [9].

The small metal cations (Fe and Me) in W-type hexaferrite reside in seven different interstitial crystallographic sites known as $4f_{VI}$, $2d$, $12k$, $6g$, $4f$, $4f_{IV}$ and $4e$ [18, 19]. These crystallographic sites are normally grouped into five magnetic sublattices as shown in Table 1 [16, 20, 21].

TABLE 1. Crystallographic and magnetic sites and their coordinations, positions in the unit cell, net magnetic sublattice spin orientation and occupancy for BaW structure.

Magnetic site	Crystallographic site	Coordination	Block	Spin	Number of metal ions
f_{VI}	$4f_{VI}$	Octahedral	R	Down	2
a	$6g$	Octahedral	S-S	Up	3
	$4f'$	Octahedral	S	Up	2
	$4e$	Tetrahedral	S	Down	2
f_{IV}	$4f_{IV}$	Tetrahedral	S	Down	2
k	$12k$	Octahedral	R-S	Up	6
b	$2d$	Bi-pyramidal	R	Up	1

Extensive research work on W-type hexaferrites prepared by different synthesis routes with a variety of cationic substitutional scenarios was carried out due to their potential for applications in microwave absorption [22-37], magnetic recording [20, 38-40] and other electrical devices [41-43]. All BaW hexaferrites, with the exception of Co_2W , are characterized by a uniaxial anisotropy. W-type hexaferrites containing Co^{2+} ions exhibit a complex magnetic structure with the variation of temperature, where spin reorientation transitions from easy plane, to easy cone, to easy axis are expected, making these ferrites of potential importance for magnetic refrigeration [24, 44-47]. Co_2W ferrite ($\text{BaCo}_2\text{Fe}_{16}\text{O}_{27}$) has a cone of easy magnetization with a constant vertex angle of 70° to the c -axis in the temperature range from -273°C to 180°C . As the temperature increases, the easy magnetization direction rotates towards the c -axis until the ferrite becomes uniaxial at 280°C [48].

Much of the research work on W-type hexaferrites available in the literature was concerned with Co- and Zn-based ferrites with a variety of cationic substitutions. Modification of the properties of the W-type ferrite based on Mg^{2+} as the divalent metal ion, however, was not addressed sufficiently in the literature [49], especially adequate structural and magnetic characterization. In this study, the effects of Co^{2+} cationic substitution for Mg^{2+} on the structural and magnetic properties of BaMg_2W hexaferrites were investigated by XRD, SEM and VSM. The results of measurements made by various experimental techniques were compared to reach an understanding of the crystalline and magnetic structure of the compounds. The spin reorientation transitions in the Co^{2+} -substituted compounds were investigated by means of thermomagnetic measurements.

Experimental

Samples of BaMg_{2-x}Co_xFe₁₆O₂₇ ($x = 0.0, 1.0$ and 2.0) were prepared by ball milling stoichiometric ratios of high purity ($\sim 99\%$) barium carbonate (BaCO₃), Fe₂O₃, CoO and MgO precursor powders using a high-energy ball mill (Fritsch Pulverisette-7) equipped with zirconia bowls and balls. The milling was carried out in an acetone medium for a period of 16 h at an angular speed of 250 rpm. The product was then left to dry in air at room temperature. Cylindrical pellets of about 1.2 cm in diameter and ~ 2 mm in thickness were made by pressing ~ 0.8 g of the powder under a 5-ton force in a stainless steel die. The discs were then sintered in an oven at 1100° C, 1200° C and 1300° C for 2 h in air.

X-ray diffraction (XRD) patterns of the sintered samples were collected using XRD 7000-Shimadzu diffractometer with Cu-K α radiation ($\lambda_1 = 1.540560\text{\AA}$, $\lambda_2 = 1.54439\text{\AA}$), in the angular range $20^\circ \leq 2\theta \leq 70^\circ$ with scanning step of 0.01. The patterns were analyzed using Expert High Score 2.0.1 software to identify the structural phases and Rietveld analysis was performed for structural refinement using FullProf software.

SEM system (FEI-Inspect F50/FEG) equipped with energy dispersive spectrometer

(EDS) was used to investigate the particle morphology and size distribution, as well as the homogeneity and local chemical composition of the prepared samples. The magnetic properties of the samples were examined using vibrating sample magnetometer (VSM Micro Mag 3900, Princeton Measurements Corporation), which operated at applied fields up to 10 kOe.

Results and Discussion

XRD Results

The XRD patterns were collected in the angular range $0^\circ \leq 2\theta \leq 70^\circ$ for all samples BaMg_{2-x}Co_xFe₁₆O₂₇ ($x = 0.0, 1.0, 2.0$) sintered at 1100° C, 1200° C and 1300° C. XRD analysis using Expert High score software revealed that all samples sintered at 1300° C consisted of a single W-type phase, whereas the samples sintered at lower temperatures were all multicomponent, consisting of BaM and cubic spinel MeFe₂O₄ (Me = Mg, Co) structural phases as demonstrated by the representative patterns in Fig. 1 for the sample with $x = 1.0$. Similar results (not shown for brevity) were obtained for the samples with different x values. These results indicated that crystallization of the W-type phase at 1300° C was preceded by the crystallization of the intermediate BaM and cubic spinel phases at lower temperatures.

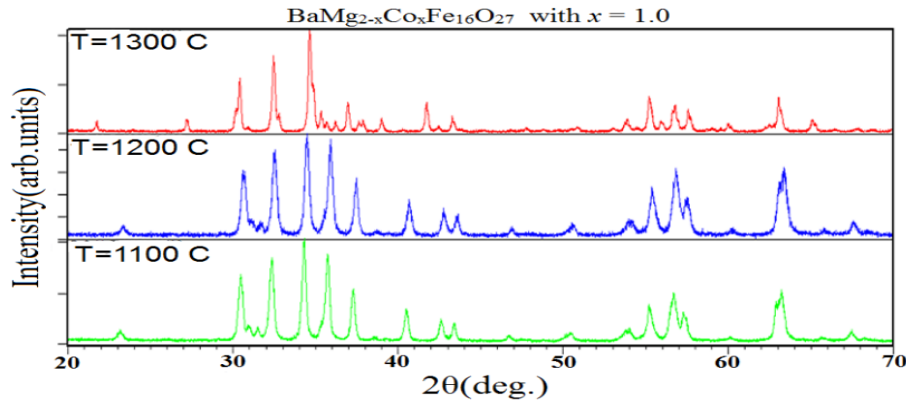


FIG. 1. X-ray diffraction patterns of BaMgCoFe₁₆O₂₇ ferrites sintered at different temperatures.

XRD pattern for the sample with $x = 2$ sintered at 1300° C revealed the existence of a single Co₂W (BaCo₂Fe₁₆O₂₇) hexaferrite phase consistent with the standard pattern (JCPDS 01-078-0135), while the patterns of the samples sintered at 1100° C and 1200° C indicated the coexistence of BaFe₁₂O₁₉ (BaM) hexaferrite phase consistent with the standard pattern (JCPDS 00-043-0002) together with CoFe₂O₄

spinel phase matching the standard pattern (JCPDS 01-079-1744). Also, the diffraction pattern for the sample with $x = 1.0$ sintered at 1300° C shows the existence of MgCo-W (BaMgCoFe₁₆O₂₇) hexaferrite phase consistent with the standard pattern (JCPDS 01-078-0135). The patterns for the samples sintered at 1100° C and 1200° C, however, indicated the existence of BaM hexaferrite phase consistent with the

standard pattern (JCPDS 00-043-0002), together with MgFe_2O_4 spinel phase consistent with the standard pattern (JCPDS 01-089-3084) and CoFe_2O_4 spinel consistent with the standard pattern (JCPDS 01-079-1744). Similarly, the XRD pattern for the sample with $x = 0.0$ sintered at 1300°C indicated the existence of a single Mg_2W ($\text{BaMg}_2\text{Fe}_{16}\text{O}_{27}$) hexaferrite phase consistent with the standard pattern (JCPDS 01-078-1551), while the patterns for the samples sintered at 1100°C and 1200°C revealed the existence of BaM hexaferrite phase consistent with the standard pattern (JCPDS 00-043-0002), together with Mg-spinel (MgFe_2O_4) phase consistent with the standard (JCPDS 01-089-3084). These results indicated that the M-phase and the spinel phase are intermediate phases that react to form the W-type phase at 1300°C .

Rietveld refinement of the XRD patterns of the samples sintered at 1300°C was performed using FullProf fitting routine (Fig. 2) and the refined lattice parameters and cell volume of the W phases are tabulated in Table 2. In Rietveld refinement, the reliability of the fit and the validity of the crystal structure model used in the fit are measured by the Bragg reliability factor

(R_B) and that of the structure factor (R_F), both of which are based on the discrepancy between the observed and calculated integrated intensities of the individual Bragg reflections. Additionally, the χ^2 parameter is a measure of the goodness of fit, which is based on the discrepancy between the observed and calculated intensities at the individual channels (angular positions). The relatively low values of these factors (Table 2) indicate reliable fit, where the structure model calculation is in good agreement with the observed diffraction data. The lattice parameters a and c for Co_2W are slightly lower than those for Mg_2W , in good agreement with previously reported results [18]. Also, the cell volume V of Co_2W is slightly ($< 0.1\%$) lower than that of Mg_2W . These results cannot be associated with the differences between the ionic radii of Mg^{2+} and Co^{2+} ions, since Co^{2+} ions have a slightly higher ionic radius at octahedral site (0.745 \AA) than Mg^{2+} (0.72 \AA) and the two ions have almost the same ionic radius at tetrahedral sites ($0.57\text{--}0.58\text{ \AA}$) [50]. Accordingly, the variations of the structural parameters can be associated with lattice distortions [5].

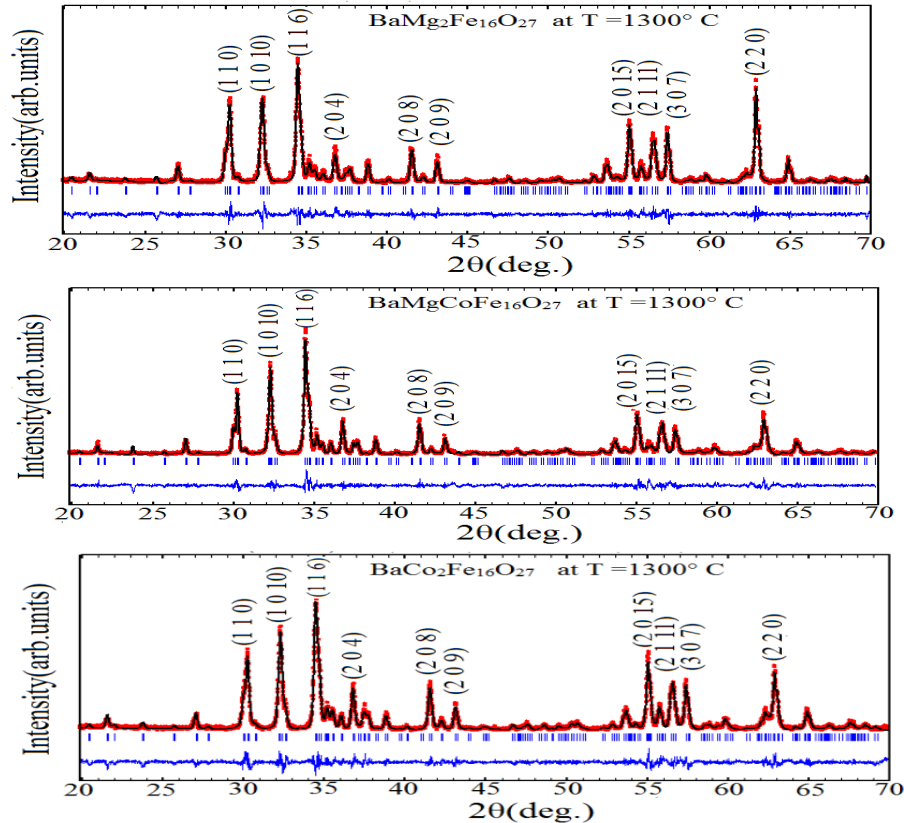


FIG. 2. Rietveld refinement of the X-ray diffraction patterns of the system $\text{BaMg}_{2-x}\text{Co}_x\text{Fe}_{16}\text{O}_{27}$ ($x = 0.0, 1.0, 2.0$) sintered at 1300°C .

TABLE 2. Results of the refinement of the patterns for the samples BaMg_{2-x}Co_xFe₁₆O₂₇ ($x = 0.0, 1.0, 2.0$) sintered at 1300° C.

Phase formula	Lattice parameters		V (Å ³)	ρ_x (g/cm ³)	R_F	R_B	χ^2
	$a = b$ (Å)	c (Å)					
BaMg ₂ Fe ₁₆ O ₂₇	5.9076	32.9681	996.4	5.04	1.36	1.36	1.87
BaMgCoFe ₁₆ O ₂₇	5.9061	32.9565	995.6	5.15	0.67	0.89	1.97
BaCo ₂ Fe ₁₆ O ₂₇	5.9069	32.9552	995.8	5.27	0.73	1.04	1.91

The X-ray density (ρ_x) increased linearly with increasing x , as shown in Table 2, recording an increase of 4.56% for the sample with $x = 2.0$. This increase is mainly due to the increase of the molecular weight of the W-type hexaferrite by 4.58% when Co replaced Mg completely, since the effect of the decrease of the cell volume on the X-ray density is much smaller.

The bulk density (ρ_b) of the samples sintered at 1300° C was measured by Archimedes method and the porosity (P) of each sample was evaluated using the relation:

$$P = 1 - \frac{\rho_b}{\rho_x} \quad (1)$$

The porosity of all samples (Table 3) is relatively low, indicating the possibility of producing highly densified (> 90% dense) magnets using the present synthesis route.

TABLE 3. X-ray density (ρ_x), bulk density (ρ_b) and porosity (P) of BaMg_{2-x}Co_xFe₁₆O₂₇ ($x = 0.0, 1.0, \text{ and } 2.0$) sintered at 1300° C.

x	ρ_b (g/cm ³)	ρ_x (g/cm ³)	P (%)
0.0	4.72	5.04	6.4
1.0	4.75	5.15	7.7
2.0	4.82	5.27	8.5

Crystallite size (D), lattice strain and instrumental effects are the main factors that cause the broadening of the diffraction peaks [51]. The instrumental broadening must be subtracted from the observed peak broadening in order to determine the effect of the lattice strains and crystallite sizes on the peak broadening. The instrumental broadening was estimated from the broadening of the diffraction peaks of a standard silicon sample. In our study, the effect of the lattice strain was found to be very small and it could be neglected. Therefore, the only effect of the broadening of the diffraction peaks was the crystallite size.

The crystallite size was determined using the Stokes and Wilson equation [5]:

$$D = \frac{\lambda}{\beta \cos \theta} \quad (2)$$

where θ is the peak position, β is the integral breadth (= area under the peak divided by the

maximum intensity) and λ is the wavelength of radiation (1.5406 Å). The integral breadth and peak position were determined by fitting a diffraction peak with a Lorentzian line shape and the crystallite size along the corresponding crystallographic direction was evaluated. Analysis of the (1 1 0) peak at $2\theta = 30.4^\circ$ was carried out to determine the crystallite size along the basal plane of the hexagonal lattice, while analysis of the (1 0 10) peak at $2\theta = 32.4^\circ$ was performed to explore the crystallite size along the c -direction. Furthermore, the peak at $2\theta = 34.6^\circ$ was considered to explore the crystallite size in the more general direction perpendicular to the corresponding (116) crystallographic planes. The values of D for all samples along the different investigated directions revealed nanocrystalline nature for all samples with crystallite size between 32 nm and 58 nm (Table 4).

TABLE 4. The crystallite size for BaMg_{2-x}Co_xFe₁₆O₂₇ ($x = 0.0, 1.0, 2.0$) sintered at 1300° C evaluated along different crystallographic directions.

x	D (nm)		
	(1 1 0)	(1 0 10)	(1 1 6)
0.00	36	34	35
1.00	58	57	40
2.00	30	44	32

SEM Results

SEM image of BaMg_{2-x}Co_xFe₁₆O₂₇ with $x = 0.0$ sintered at 1100° C (shown in Fig. 3-a) indicated that the sample consisted mostly of cuboidal particles and hexagonal platelets with an average size of around 230 nm. The particles in this sample seem to agglomerate with relatively high inter-particle porosity. Also, SEM image of BaMg_{2-x}Co_xFe₁₆O₂₇ with $x = 0.0$ sintered at 1200° C (Fig. 3-b) indicated that the sample consisted of cuboidal particles and hexagonal platelets with a relatively wide distribution of particle size mostly in the range between 0.2-1.0 μm . The particles in this sample stacked with low inter-particle porosity.

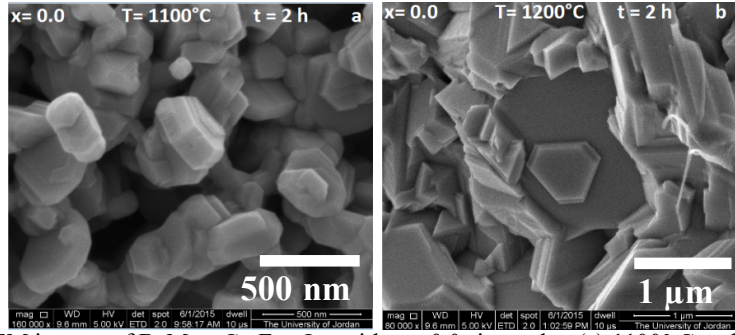


FIG. 3. SEM images of $\text{BaMg}_{2-x}\text{Co}_x\text{Fe}_{16}\text{O}_{27}$ with $x = 0.0$ sintered at (a) 1100°C and (b) 1200°C .

Representative SEM images of $\text{BaMg}_{2-x}\text{Co}_x\text{Fe}_{16}\text{O}_{27}$ with $x = 0.0$ sintered at 1300°C (Fig. 4) revealed granular structure mainly composed of regular hexagonal plates characterized by a wider distribution of particle size. The diameters of the hexagonal plates ranged between $0.7\text{--}5\text{ }\mu\text{m}$ with an average grain

size of $2.2\text{ }\mu\text{m}$. Since the critical single-domain size in hexaferrite was reported to be $0.46\text{ }\mu\text{m}$ [52], we may conclude that the sample consists of multi-domain particles. The particles in this sample stacked closely with relatively low porosity.

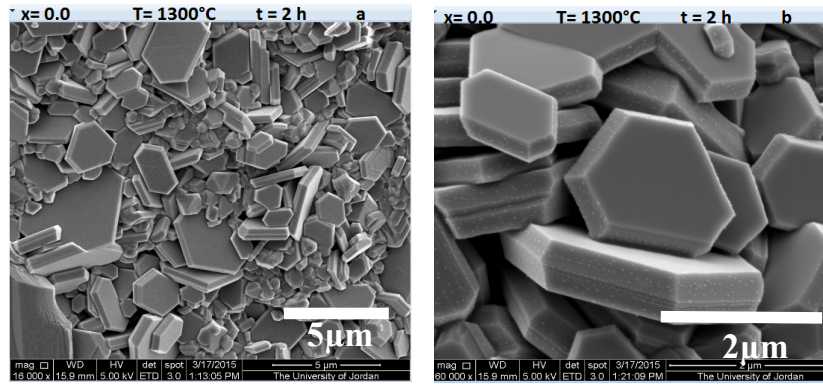


FIG. 4. SEM images of $\text{BaMg}_{2-x}\text{Co}_x\text{Fe}_{16}\text{O}_{27}$ with $x = 0.0$ sintered at 1300°C .

SEM image of $\text{BaMg}_{2-x}\text{Co}_x\text{Fe}_{16}\text{O}_{27}$ with $x = 1.0$ sintered at 1100°C (Fig. 5-a) also indicated that the sample consisted mainly of cuboidal particles and hexagonal platelets with diameters ranging between $100\text{--}500\text{ nm}$. Improvement of the crystallization of hexagonal platelets and

increase of the particle size to the range of $0.5\text{--}1.7\text{ }\mu\text{m}$ was observed at a sintering temperature of 1200°C (Fig. 5-b). Most of the particles in this sample are below the critical single domain size of about $0.5\text{ }\mu\text{m}$ and a small fraction is $> 1.0\text{ }\mu\text{m}$ in size.

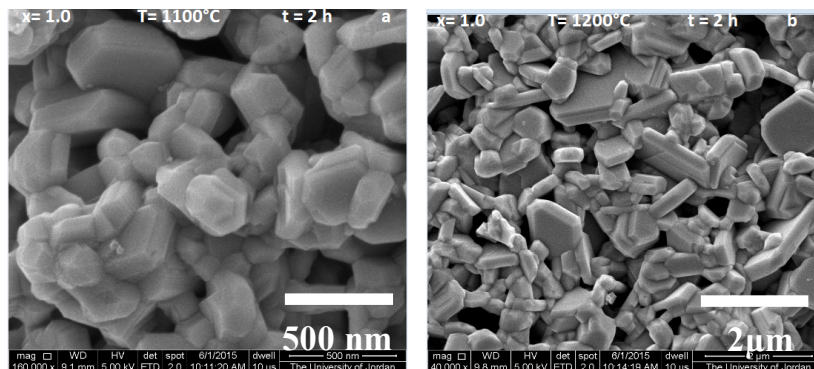


FIG. 5. SEM images of $\text{BaMg}_{2-x}\text{Co}_x\text{Fe}_{16}\text{O}_{27}$ with $x = 1.0$ sintered at (a) 1100°C and (b) 1200°C .

Fig. 6 shows representative SEM images of $\text{BaMg}_{2-x}\text{Co}_x\text{Fe}_{16}\text{O}_{27}$ with $x = 1.0$ sintered at 1300°C . The sample is generally composed of

non-granular mass, with only a small fraction of hexagonal plates. The diameters of the hexagonal plates were between 1-3 μm .

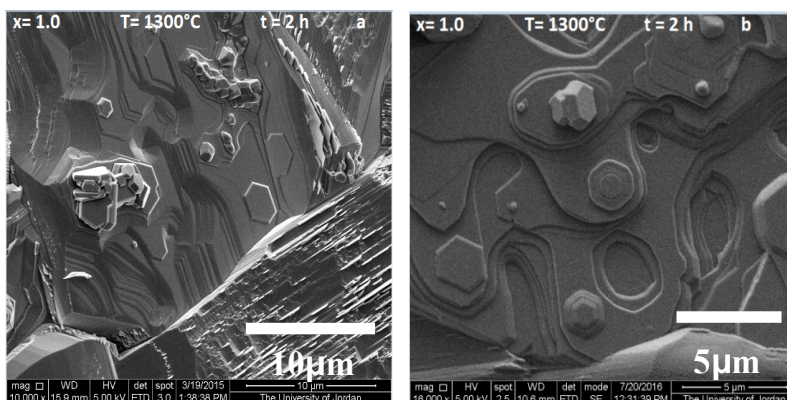


FIG. 6. SEM images of $\text{BaMg}_{2-x}\text{Co}_x\text{Fe}_{16}\text{O}_{27}$ with $x = 1.0$ sintered at 1300°C .

In addition, SEM images (Fig. 7) of $\text{BaMg}_{2-x}\text{Co}_x\text{Fe}_{16}\text{O}_{27}$ with $x = 2.0$ sintered at 1100°C indicated that the sample consisted mainly of cuboidal particles and hexagonal platelets with a relatively narrow distribution of particle size and

an average size of around 240 nm. The sample sintered at 1200°C (Fig. 7-b) indicated improved crystallization of hexagonal particles and the existence of large non-particulate masses.

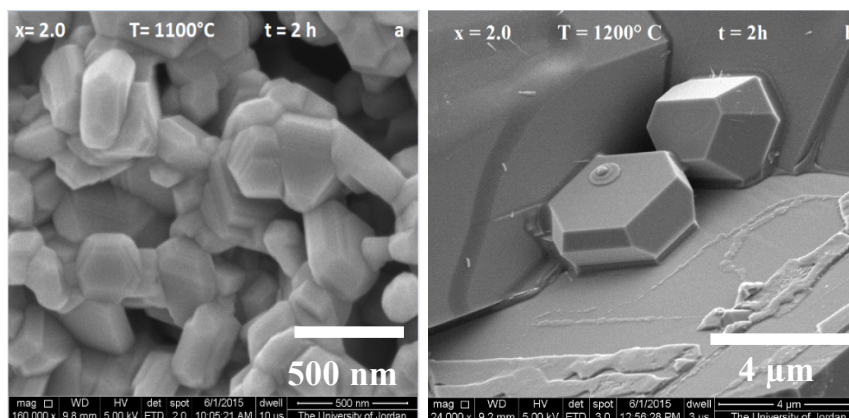


FIG. 7. SEM images of $\text{BaMg}_{2-x}\text{Co}_x\text{Fe}_{16}\text{O}_{27}$ with $x = 2.0$ sintered at (a) 1100°C and (b) 1200°C .

Fig. 8 shows SEM images of the $\text{BaMg}_{2-x}\text{Co}_x\text{Fe}_{16}\text{O}_{27}$ with $x = 2.0$ sintered at 1300°C . The sample is generally composed of large non-granular masses, with only a small fraction of

perfect hexagonal plates, the diameters of which were in the range of 0.5-2 μm . The non-granular masses developed in layered, nonporous structures.

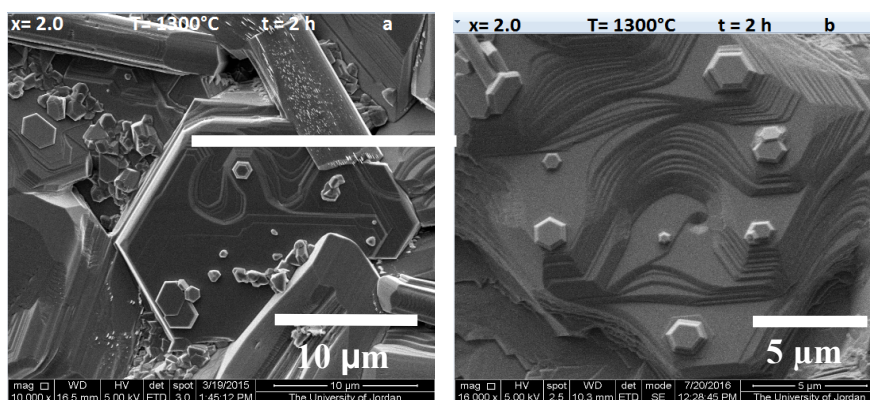


FIG. 8. SEM images of $\text{BaMg}_{2-x}\text{Co}_x\text{Fe}_{16}\text{O}_{27}$ with $x = 2.0$ sintered at 1300°C .

Energy dispersive x-ray spectroscopy (EDS) was used to examine the chemical composition of the samples sintered at 1300° C. The spectra collected from two different spots of the sample with $x = 0.0$ revealed that the Fe:Ba ratio was 14.9 and 16.3, while the Mg:Ba ratio was 1.26 and 1.52. The Fe:Ba ratio is consistent with the theoretical stoichiometric ratio of 16.0 for Mg_2W hexaferrite, while the difference between the observed Mg:Ba ratio and the theoretical ratio of 2 cannot be accounted for by the calculated experimental uncertainty (of $\sim 20\%$). This discrepancy could be associated with the low signal for Mg and the position of its emission line in a sloped and noisy region of the background, which makes the line intensity evaluated by the software unreliable.

EDS spectra from two different spots of the sample with $x = 1.0$ indicated that the Fe:Ba ratio was 15.7 and 14.0, which is consistent with the theoretical value within the experimental uncertainty of $\sim 17\%$. The Mg:Ba ratio at the two spots was 1.95 and 0.98. Although the ratio from the second spot was in good agreement with the theoretical value of 1.00, the significantly higher value from the first spot may indicate unreliability of the evaluated Mg:Ba ratio due to the weak signal of Mg occurring in a rather noisy and sloped background. On the other hand, the Co:Ba ratio at the two spots was 2.58 and 2.06, which is more than double the theoretical value of 1.00. This difference cannot

be accounted for by the experimental uncertainty of $\sim 19\%$ and the observed high Co:Ba ratio can be attributed to the overlapping between the Co-K_α line (which was used for evaluation of the Co concentration) and the Fe-K_β spectral line (the difference of the energies of these two lines is $< 2\%$).

EDS spectrum collected from a representative point in the sample with $x = 2.0$ revealed that Fe:Ba = 15.6, which is in good agreement with the theoretical value of 16.0. On the other hand, Co:Ba ratio was found to be 3.86, which is significantly higher than the theoretical value of 2.00. Again, this high value is associated with the apparent increase of the spectral intensity of the Co-K_α line due to overlapping with Fe-K_β spectral line.

VSM Results

Room Temperature Hysteresis Loop

In this section, the magnetic properties of the system $\text{BaMg}_{2-x}\text{Co}_x\text{Fe}_{16}\text{O}_{27}$ ($x = 0.0, 1.0, \text{ and } 2.0$) samples sintered at 1100° C, 1200° C and 1300° C were investigated using room temperature hysteresis loop (HL) measurements in an applied field up to 10 kOe. The hysteresis loops (HLs) for all the samples are shown in Figs. 9, 10 and 11. The values of the saturation magnetization, M_s , remanence magnetization, M_r and coercive field, H_c were determined from the hysteresis loops.

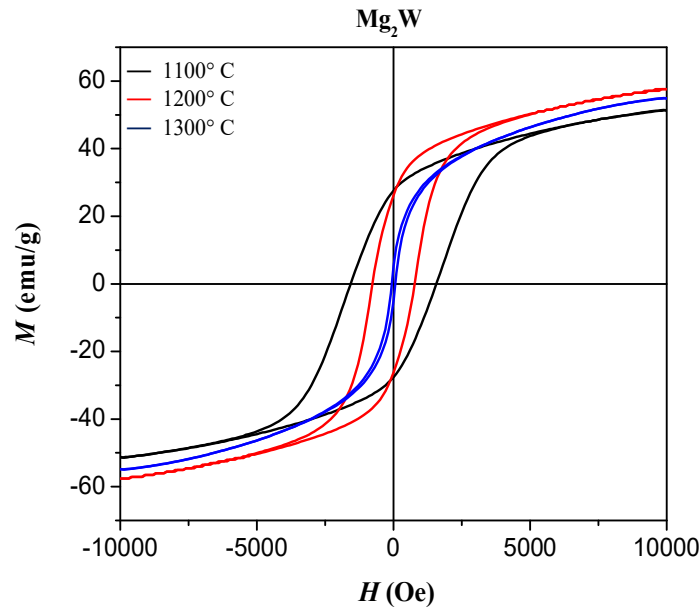


FIG. 9. Hysteresis loops of $\text{BaMg}_{2-x}\text{Co}_x\text{Fe}_{16}\text{O}_{27}$ with $x = 0.0$ sintered at 1100° C, 1200° C and 1300° C.

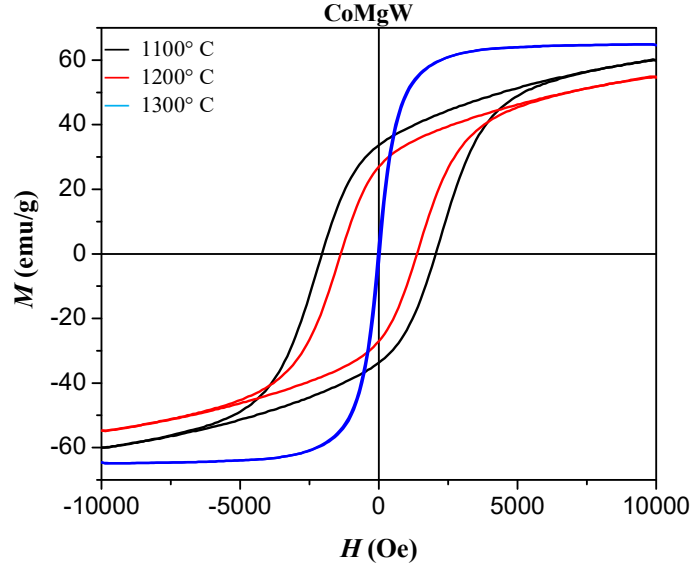


FIG. 10. Hysteresis loops of BaMg_{2-x}Co_xFe₁₆O₂₇ with $x = 1.0$ sintered at 1100° C, 1200° C and 1300° C.

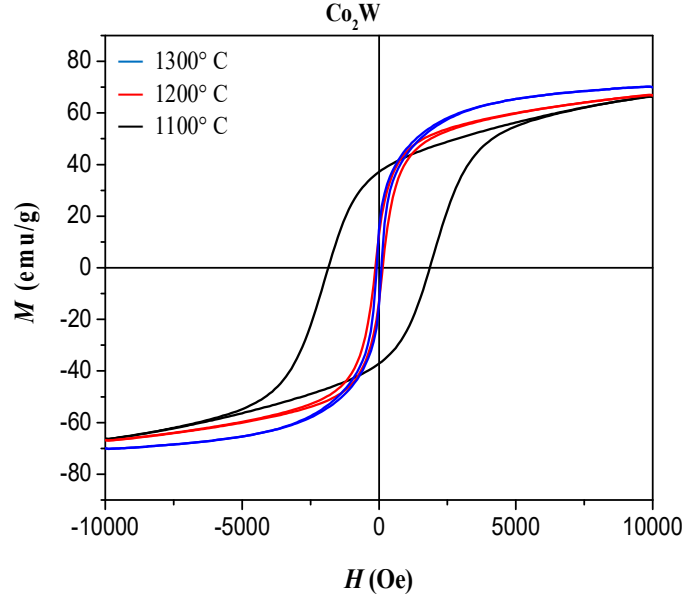


FIG. 11. Hysteresis loops of BaMg_{2-x}Co_xFe₁₆O₂₇ with $x = 2.0$ sintered at 1100° C, 1200° C and 1300° C.

The HLs for all samples indicated magnetic softening with the increase of the sintering temperature. The coercivity and remanence magnetization were determined directly from the hysteresis loops, while the saturation magnetization, M_s , was determined from the law of approach to saturation (LAS) [12, 53]:

$$M = M_s \left(1 - \frac{A}{H} - \frac{B}{H^2} \right) + \chi H \quad (3)$$

Here, M is the magnetization (in emu/cm³), M_s is the spontaneous saturation magnetization of the domains per unit volume, A is a constant associated with microstress and/or inclusions, B

is a constant representing the magnetocrystalline anisotropy contribution and χH is the forced magnetization term. Plotting M versus $1/H^2$ in the high field range 8.5 – 10 kOe gave straight lines, indicating that the magnetization in this field range is determined completely by the magnetocrystalline term.

The saturation magnetization was determined from the intercept of the straight line with the M -axis. The magnetic parameters derived from the hysteresis loops are tabulated in Table 5.

TABLE 5. Saturation magnetization, remanence magnetization, squareness ratio and coercive field for BaMg_{2-x}Co_xFe₁₆O₂₇ sintered at different temperatures.

x	$T(^{\circ}\text{C})$	$M_s(\text{emu/g})$	$M_r(\text{emu/g})$	M_{rs}	$H_c(\text{kOe})$
0.0	1100	55.4	27.5	0.50	1.57
0.0	1200	62.1	26.1	0.42	0.77
0.0	1300	59.4	4.33	0.07	0.07
1.0	1100	64.5	33.6	0.52	2.05
1.0	1200	59.8	26.9	0.45	1.37
1.0	1300	65.2	2.66	0.04	0.03
2.0	1100	72.6	37.1	0.51	1.85
2.0	1200	71.2	12.1	0.17	0.14
2.0	1300	72.6	11.7	0.16	0.09

Because the W-type hexaferrite structure is built up of M-type hexaferrite and S block, where S block contains two spinel molecules, the magnetic moment of the W-type hexaferrite can be described by the relations [9, 34, 54],

$$\mu_W = \mu_M + 2\mu_S, \quad (4)$$

$$\mu = \frac{MM_s}{N_A\mu_B}, \quad (5)$$

where μ_M is the magnetic moment of BaFe₁₂O₁₉ and μ_S is the magnetic moment of spinel, M is molecular weight, M_s is the saturation magnetization, N_A is Avogadro's number (6.023×10^{23} molecules/mole), μ_B is the Bohr magneton (9.27×10^{-21} erg/G) and μ is the magnetic moment of a given compound. Therefore, by combining Eq. (4) and Eq. (5), we obtain:

$$(M_s)_W = \left[\frac{M_M}{M_W} \right] (M_s)_M + 2 \left[\frac{M_S}{M_W} \right] (M_s)_S. \quad (6)$$

This last equation predicts that the saturation magnetization of Mg₂W is 58.6 emu/g, which is in good agreement with the observed value of 59.4 emu/g for Mg₂W sample sintered at 1300° C. On the other hand, the expected theoretical saturation magnetization of MgCoW is 66 emu/g, which is also in good agreement with the observed value of 65.2 emu/g. Further, the expected saturation magnetization of Co₂W is 72.96 emu/g, which is also in good agreement with the observed value of 72.6 emu/g. These results indicate that the magnetization of the W-type phase can be determined from the superposition of the magnetizations of the underlying magnetic phases.

The saturation magnetization for the sample with $x = 0$ increased with sintering temperature from 55.4 emu/g for the sample sintered at 1100° C to 62.1 emu/g for the sample sintered at 1200° C. The sample sintered at 1100° C is a mixture

of BaM phase and MgFe₂O₄ phase, as indicated by XRD analysis. Assuming that the magnetization of the sample results from a simple superposition of the BaM and Mg-spinel phases and using the values of the saturation magnetizations of polycrystalline BaM phase of 70 emu/g [1] and of 27 emu/g for MgFe₂O₄ phase [9], the saturation magnetization for the sample sintered at 1100° C (55.4 emu/g) suggests that this sample is composed of about 66 wt. % BaM phase and 34 wt. % MgFe₂O₄ phase. If all Mg were incorporated in the formation of MgFe₂O₄ spinel phase, the sample would consist of BaM and Mg-spinel phase with a molar ratio of 1:2, corresponding to 73.5 wt.% BaM and 26.5 wt.% Mg-spinel (molar mass of Mg-spinel = 200 g and of BaM = 1111.5 g). These fractions should give a theoretical value of 58.6 emu/g, which is higher than the observed value. The lower observed value could then be attributed to BaM and Mg-spinel phases with saturation magnetizations lower than the theoretical values. The saturation magnetization results are therefore consistent with the picture of phase segregation into BaM and Mg-spinel at a sintering temperature of 1100° C. The saturation magnetization of the sample sintered at 1200° C (62.1 emu/g), on the other hand, suggests that the sample consists of about 81.6 wt. % of BaM phase and 18.4 wt. % of MgFe₂O₄ phase. This may indicate that a fraction of the Mg ions substitutes Fe ions in the hexaferrite phase, which results in a reduction of the mass fraction of the Mg-spinel in the sample and a consequent increase of the saturation magnetization.

The coercivity of the samples with $x = 0$ decreased from 1.57 kOe for the sample sintered at 1100° C, down to 0.77 kOe at a sintering temperature of 1200° C and to 0.07 kOe at a

sintering temperature of 1300° C. The decrease of the coercivity of the sample sintered at 1200° C can be attributed to the significant increase of the particle size as the temperature increases (SEM results). The significant drop in the coercivity of the sample sintered at 1300° C is associated with the crystallization of large hexagonal plates of Mg₂W phase by solid state reaction of the intermediate BaM and MgFe₂O₄ phases at high sintering temperatures. The decrease of the squareness ratio (M_{rs}) to values below 0.5 (which is characteristic of single-domain, randomly oriented assembly of particles) is consistent with particle growth to the multidomain particle size regime. The multidomain nature of the particles is responsible for the significant decrease in coercivity, since in this case, the domain-wall motion is dominant in the magnetization processes.

The saturation magnetization for the sample with $x = 1$ decreased from 64.5 emu/g for the sample sintered at 1100° C, down to 59.8 emu/g at a sintering temperature of 1200° C, then increased up to 65.2 emu/g at a sintering temperature of 1300° C. The sample sintered at 1100° C is a mixture of BaM phase and MgFe₂O₄ and CoFe₂O₄ spinel phases. Again, assuming that the saturation magnetization of the sample sintered at 1100° C results from a simple superposition of the saturation magnetizations of the magnetic phases in the sample and using the saturation magnetization of 80 emu/g for CoFe₂O₄ phase [9], the saturation magnetization for this sample (64.5 emu/g) is consistent with 62 wt. % of BaM phase, 17.5 wt. % of MgFe₂O₄ phase and 20.5 wt. % of CoFe₂O₄ phase. In calculating the weight fractions, the ratio of the molar mass of Co-spinel to that of Mg-spinel (1.173) and equal molar ratios of the two spinel phases were assumed to determine the fractions of the two spinel phases. The relative weight fractions of the BaM and spinel phases (62 wt. % and 38 wt. %, respectively) are similar to those of the sample with $x = 0$ sintered at the same temperature. The saturation magnetization of the sample sintered at 1200° C decreased to 59.8 emu/g, which is consistent with 30 wt.% BaM, 32.2 wt.% Mg-spinel and 37.8 wt.% Co-spinel. The increase of the weight fraction of the spinel phases (the weighted average of saturation magnetization of which is 55.6 emu/g) cannot be justified on the basis of the starting materials in the sample and therefore, the reduction of the

saturation magnetization could be attributed to the presence of BaM and spinel phases with saturation magnetizations lower than their theoretical values.

The sample sintered at 1300° C is composed of MgCo-W hexaferrite. The increase in saturation magnetization with respect to the sample with $x = 0.0$ can be associated with the increase of the magnetic moment per molecular formula. Since Mg²⁺ is a non-magnetic ion and the magnetic moment of Co²⁺ ion is 3.7 μ_B , the increase in the saturation magnetization of this sample suggests that Co²⁺ ions replace Mg²⁺ ions at spin-up sites.

The coercivity decreased from 2.05 kOe for the sample sintered at 1100° C, down to 1.37 kOe at a sintering temperature of 1200° C and to 0.03 kOe at a sintering temperature of 1300° C. The decrease of the coercivity of the sample sintered at 1200° C could be associated with the increase of particle size of the BaM phase. The sharp drop in the coercivity of the sample sintered at 1300° C, however, is associated with phase transformation from hard BaM phase to soft BaW phase with large particle size. The small decrease of the squareness ratio, M_{rs} , from 0.52 for the sample sintered at 1100° C to 0.45 for the sample sintered at 1200° C is consistent with the small increase of the particle size beyond the critical single domain size as indicated by SEM images. The sharp drop in the squareness ratio down to 0.04 for the sample sintered at 1300° C, however, is due to transformation from hard BaM magnetic phase with almost single-domain particle size to soft, large non-granular masses of BaW phase.

The saturation magnetization for the samples with $x = 2$ revealed similar values at the different sintering temperatures (72.6 emu/g for the sample sintered at 1100° C, 71.2 emu/g at a sintering temperature of 1200° C and 72.6 emu/g at a sintering temperature of 1300° C). The sample sintered at 1100° C is a mixture of BaM and CoFe₂O₄ as indicated by XRD analysis. The saturation magnetization of 72.6 emu/g is consistent with 74 wt. % BaM and 26 wt. % CoFe₂O₄. If we assume that Co²⁺ ions were fully consumed in the spinel phase, the fractions of the BaM and spinel phase would be 70.3 wt.% and 29.7 wt.%, respectively, corresponding to an expected saturation magnetization of 72.96 emu/g. This value is similar to the observed saturation magnetization, which is an indication

of that this sample consists of BaM and Co-spinel phases with saturation magnetizations close to the theoretical values. On the other hand, the saturation magnetization of 71.2 emu/g for the sample sintered at 1200° C could indicate that Co partially substituted Fe in the hexaferrite lattice. The saturation magnetization of the sample sintered at 1300° C is 72.6 emu/g, which is in good agreement with the previously reported values of 71.18 emu/g for BaCo₂Fe₁₆O₂₇ [41] and 74.31 emu/g for SrCo₂Fe₁₆O₂₇ [55].

The coercivity decreased from 1.85 kOe for the sample sintered at 1100° C, down to 0.14 kOe at a sintering temperature of 1200° C and down to 0.09 kOe at a sintering temperature of 1300° C. These dramatic changes were associated with magnetic softening as a result of particle growth at 1200° C sintering temperature and the transformation of BaM and Co-spinel phases to large, non-granular masses of W-type hexaferrite phase at 1300° C sintering

temperature. The significant decreases of the squareness ratio M_{rs} from 0.51 to 0.17 and 0.16 is an indication of that the samples sintered at 1200° C and 1300° C consist of large multidomain volumes in these samples.

The soft magnetic character and the low coercivity values of 70 Oe for Mg₂W, 30 Oe for MgCo-W and 90 Oe for Co₂W for the samples sintered at the highest temperature of 1300° C are in good agreement with the values reported for Co-substituted Zn₂W ferrites [56]. The increase of the saturation magnetization from 59.4 emu/g for Mg₂W to 65.2 emu/g for CoMg-W and then to 72.6 emu/g for Co₂W is a result of the substitution of Mg²⁺ ions by Co²⁺ ions at spin-up sites. The saturation trends of the samples (Fig. 12) revealed that the magnetization of sample with $x = 1.0$ is almost saturated at an applied field of 10 kOe, indicating low magnetocrystalline anisotropy relative to the two end compounds ($x = 0.0$ and 2.0).

T = 1300° C

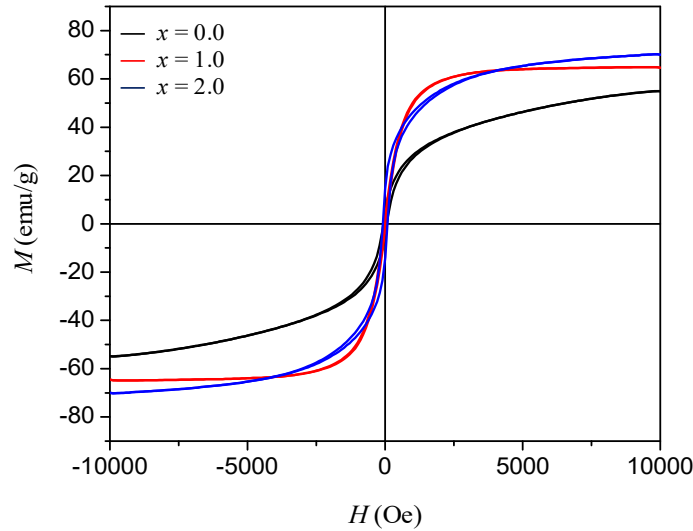


FIG. 12. Hysteresis loops of BaMg_{2-x}Co_xFe₁₆O₂₇ ($x = 0.0, 1.0$ and 2.0) sintered at 1300° C.

Thermomagnetic Measurements

The thermomagnetic curves of the system BaMg_{2-x}Co_xFe₁₆O₂₇ ($x = 0.0, 1.0$ and 2.0) sintered at 1300° C (measured at an applied field of $H = 100$ Oe) are shown in Fig. 13, together with their derivatives with respect to temperature. The derivative curves of all samples exhibited strong negative peaks (dips) at temperatures > 450 ° C, which were associated with the Curie temperature of the corresponding W-type phase as shown in Table 6. The observed Curie temperature of 452° C for Mg₂W is equal to the previously reported value of (452±3)° C

[18] and that of 483° C for Co₂W is in good agreement with the reported values of (490±3)° C [18] and (477±5)° C [46] for this compound, while the Curie temperature of 473° C for MgCo-W lies between the Curie temperatures of the end compounds. The results indicated that the Curie temperature increased with the increase of the Co content, as a consequence of the enhancement of the superexchange interactions resulting from the substitution of Mg²⁺ nonmagnetic ions by Co²⁺ magnetic ions. The occurrence of a single strong dip in the derivative curve suggests that each sample is composed of a single W-type phase.

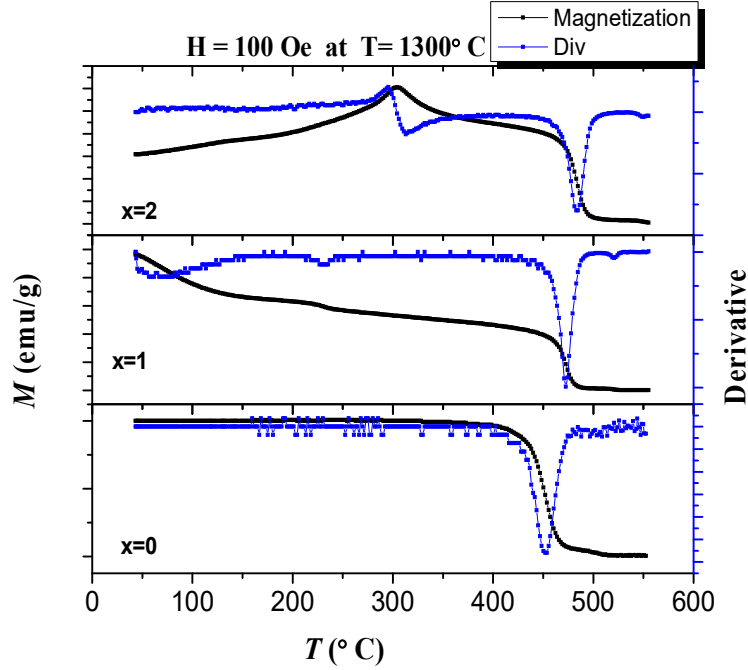


Fig. 13: Thermomagnetic curves of BaMg_{2-x}Co_xFe₁₆O₂₇ ($x = 0.0, 1.0$ and 2.0) samples sintered at 1300°C .

TABLE 6. Curie temperature of the different samples BaMg_{2-x}Co_xFe₁₆O₂₇ ($x = 0.0, 1.0$ and 2.0).

x	0.0	1.0	2.0
$T_c(^{\circ}\text{C})$	452	473	483

The derivative curve of the sample with $x = 1.0$ shows two additional weak dips at 232°C and 522°C resulting from inflection points on the magnetization curve. The weak peak at 232°C could be associated with spin reorientation transition, where the magnetic anisotropy changes from easy-cone to easy-axis. This temperature is lower than the reported spin reorientation transition temperature for Co₂W [46, 48], which is consistent with the reported increase of the spin reorientation transition temperature with the increase of Co content in Co-substituted Zn₂W ferrite [46, 47]. Further, this result is an indication of that both Mg²⁺ and Co²⁺ ions are incorporated into a single W-type phase. The high-temperature dip at 522°C is close to the reported Curie temperature of 527°C for BaCoZn_{0.5}Mg_{0.5}Fe₁₆O₂₇ [57] and could be associated with traces of Co-rich magnetic impurities in our sample.

The rise in the thermomagnetic curve of the sample with $x = 2.0$ into a peak at $\sim 304^\circ\text{C}$ is associated with the spin reorientation transition from conical to c -axis spin orientation. The shape of the derivative curve around this

temperature suggests a singular-type behavior of the magnetization, indicating that the origin of the peak is not a smooth function. This behavior is associated with the competition between the rise in the magnetization due to spin reorientation transitions and the decline due to thermal agitation. The spin reorientation transition in this sample is clearly observed at a higher temperature compared with MgCo-W. Also, a weak negative peak is observed in the derivative curve at $\sim 550^\circ\text{C}$, which can be associated with the enhancement of the superexchange interactions in Co-rich regions of the sample.

Conclusions

W-type hexaferrites were synthesized by high energy ball milling and sintering at 1300°C . The hexaferrite phase evolved from the reaction of BaM hexaferrite and cubic spinel intermediates which crystallize at lower temperatures. The saturation magnetization as well as the Curie temperature of the W-type hexaferrite increased with the increase of the Co concentration. This is a consequence of the increase of the net magnetic moment per molecule upon replacement of nonmagnetic Mg²⁺ ions by magnetic Co²⁺ ions and the consequent enhancement of the superexchange interactions between magnetic ions in spin-up and spin-down sublattices. The observed saturation

magnetization of the W-type phase in all samples was in good agreement with the calculated value using a model involving the superposition of cubic spinel and M-type ferrite phases, indicating that Mg^{2+} and Co^{2+} ions occupy octahedral sites corresponding to the (a) spin-up magnetic sublattice in the spinel (S) blocks of

the W-type unit cell. The thermomagnetic curves of the W-hexaferrites revealed spin reorientation transition around room temperature in the sample with $x = 2.0$, which could be of potential importance for magnetic refrigeration applications.

References

- [1] Pullar, R.C., Progress in Materials Science, 57 (2012) 1191.
- [2] Mahmood, S.H., "Properties and Synthesis of Hexaferrites", in: S.H. Mahmood and I. Abu-Aljarayesh (Eds.), Hexaferrite Permanent Magnetic Materials, (Materials Research Forum LLC, Millersville, PA, 2016), pp. 74-110.
- [3] Mahmood, S.H., "Permanent Magnet Applications", in: S.H. Mahmood and I. Abu-Aljarayesh (Eds.), Hexaferrite Permanent Magnetic Materials, (Materials Research Forum LLC, Millersville, PA, 2016), pp. 153-165.
- [4] Bsoul, I. and Mahmood, S., Jordan Journal of Physics, 2 (3) (2009) 171.
- [5] Awadallah, A., Mahmood, S.H., Maswadeh, Y., Bsoul, I., Awawdeh, M., Mohaidat, Q.I. and Juwhari, H., Materials Research Bulletin, 74 (2016) 192.
- [6] Mahmood, S.H., Awadallah, A., Maswadeh, Y. and Bsoul, I., IOP Conference Series: Materials Science and Engineering, IOP Publishing, (2015), p. 012008.
- [7] Awadallah, A., Mahmood, S.H., Maswadeh, Y., Bsoul, I. and Aloqaily, A., IOP Conference Series: Materials Science and Engineering, IOP Publishing, (2015), p. 012006.
- [8] Mahmood, S.H. and Bsoul, I., EPJ Web of Conferences, 29 (2012) 00039.
- [9] Smit, J. and Wijn, H.P.J., "Ferrites", (Wiley, New York, 1959).
- [10] Chikazumi, S., "Physics of Ferromagnetism", 2nd ed., (Oxford University Press, Oxford, 2009).
- [11] Alhwaitat, E.S., Mahmood, S.H., Al-Hussein, M., Mohsen, O.E., Maswadeh, Y., Bsoul, I. and Hammoudeh, A., Ceramics International, 44 (2018) 779.
- [12] Mahmood, S.H., Dushaq, G.H., Bsoul, I., Awawdeh, M., Juwhari, H.K., Lahlouh, B.I. and AlDamen, M.A., Journal of Applied Mathematics and Physics, 2 (2014) 77.
- [13] Awawdeh, M., Bsoul, I. and Mahmood, S.H., Journal of Alloys and Compounds, 585 (2014) 465.
- [14] Mahmood, S., Aloqaily, A., Maswadeh, Y., Awadallah, A., Bsoul, I. and Juwhari, H., Material Science Research India, 11 (2014) 09.
- [15] Maswadeh, Y., Mahmood, S.H., Awadallah, A. and Aloqaily, A.N., IOP Conference Series: Materials Science and Engineering, IOP Publishing, (2015), p. 012019.
- [16] Mahmood, S.H., Aloqaily, A.N., Maswadeh, Y., Awadallah, A., Bsoul, I., Awawdeh, M. and Juwhari, H.K., Solid State Phenomena, 232 (2015) 65.
- [17] Alsmadi, A., Bsoul, I., Mahmood, S., Alnawashi, G., Prokeš, K., Siemensmeyer, K., Klemke, B. and Nakotte, H., Journal of Applied Physics, 114 (2013) 243910.
- [18] Collomb, A., Wolfers, P. and Obradors, X., Journal of Magnetism and Magnetic Materials, 62 (1986) 57.
- [19] Ahmad, M., Grössinger, R., Kriegisch, M., Kubel, F. and Rana, M., Current Applied Physics, 12 (2012) 1413.
- [20] Iqbal, M.J., Khan, R.A., Mizukami, S. and Miyazaki, T., Materials Research Bulletin, 46 (2011) 1980.
- [21] Leccabue, F., Muzio, O.A., Kany, M.S.E., Calestani, G. and Albanese, G., Journal of Magnetism and Magnetic Materials, 68 (1987) 201.
- [22] Iqbal, M.J. and Khan, R.A., Journal of Alloys and Compounds, 478 (2009) 847.

- [23] Yang, Y., Zhang, B., Xu, W., Shi, Y., Zhou, N. and Lu, H., *Journal of Magnetism and Magnetic Materials*, 265 (2003) 119.
- [24] Ahmad, M., Aen, F., Islam, M., Niazi, S.B. and Rana, M., *Ceramics International*, 37 (2011) 3691.
- [25] Qin, X., Cheng, Y., Zhou, K., Huang, S. and Hui, X., *Journal of Materials Science and Chemical Engineering*, 1 (2013) 8.
- [26] Zi, Z., Dai, J., Liu, Q., Liu, H., Zhu, X. and Sun, Y., *Journal of Applied Physics*, 109 (2011) 07E536.
- [27] Iqbal, M.J., Khan, R.A., Mizukami, S. and Miyazaki, T., *Journal of Magnetism and Magnetic Materials*, 323 (2011) 2137.
- [28] Shen, G., Xu, Z. and Li, Y., *Journal of Magnetism and Magnetic Materials*, 301 (2006) 325.
- [29] Xu, J., Zou, H., Li, H., Li, G., Gan, S. and Hong, G., *Journal of Alloys and Compounds*, 490 (2010) 552.
- [30] Deng, L., Ding, L., Zhou, K., Huang, S., Hu, Z. and Yang, B., *Journal of Magnetism and Magnetic Materials*, 323 (2011) 1895.
- [31] Qiao, M., Zhang, C. and Jia, H., *Materials Chemistry and Physics*, 135 (2012) 604.
- [32] Wu, Y., Huang, Y., Niu, L., Zhang, Y., Li, Y. and Wang, X., *Journal of Magnetism and Magnetic Materials*, 324 (2012) 616.
- [33] Ahmad, M., Grössinger, R., Ali, I., Ahmad, I. and Rana, M., *Journal of Alloys and Compounds*, 577 (2013) 382.
- [34] Ahmad, M., Ali, I., Grössinger, R., Kriegisch, M., Kubel, F. and Rana, M., *Journal of Alloys and Compounds*, 579 (2013) 57.
- [35] Aen, F., Ahmad, M. and Rana, M., *Current Applied Physics*, 13 (2013) 41.
- [36] Wu, Y., Ong, C., Lin, G. and Li, Z., *Journal of Physics D: Applied Physics*, 39 (2006) 2915.
- [37] Wang, L., Song, J., Zhang, Q., Huang, X. and Xu, N., *Journal of Alloys and Compounds*, 481 (2009) 863.
- [38] Iqbal, M.J., Khan, R.A., Mizukami, S. and Miyazaki, T., *Ceramics International*, 38 (2012) 4097.
- [39] Khan, I., Sadiq, I. and Ashiq, M.N., *Journal of Alloys and Compounds*, 509 (2011) 8042.
- [40] Ram, S., *Journal of Materials Science*, 25 (1990) 2465.
- [41] Guo, F., Wu, X., Ji, G., Xu, J., Zou, L. and Gan, S., *Journal of Superconductivity and Novel Magnetism*, 27 (2014) 411.
- [42] Su, Z., Chen, Y., Hu, B., Sokolov, A.S., Bennett, S., Burns, L., Xing, X. and Harris, V.G., *Journal of Applied Physics*, 113 (2013) 17B305.
- [43] Feng, Y., Qiu, T. and Shen, C., *Journal of Magnetism and Magnetic Materials*, 318 (2007) 8.
- [44] Pasko, A., Mazaleyrat, F., Lobue, M., Loyau, V., Basso, V., Küpferling, M., Sasso, C. and Bessais, L., *Journal of Physics: Conference Series*, IOP Publishing, 303 (2011) 012045.
- [45] Rinaldi, S., Licci, F., Paoluzi, A. and Turilli, G., *Journal of Applied Physics*, 60 (1986) 3680.
- [46] Albanese, G., Calabrese, E., Deriu, A. and Licci, F., *Hyperfine Interactions*, 28 (1986) 487.
- [47] Paoluzi, A., Licci, F., Moze, O., Turilli, G., Deriu, A., Albanese, G. and Calabrese, E., *Journal of Applied Physics*, 63 (1988) 5074.
- [48] Samaras, D., Collomb, A., Hadjivasiliou, S., Achilleos, C., Tsoukalas, J., Pannetier, J. and Rodriguez, J., *Journal of Magnetism and Magnetic Materials*, 79 (1989) 193.
- [49] Khan, R.A., Mir, S., Khan, A.M., Ismail, B. and Khan, A.R., *Ceramics International*, 40 (2014) 11205.
- [50] Shannon, R.T., *Acta Crystallographica-Section A: Crystal Physics, Diffraction, Theoretical and General Crystallography*, 32 (1976) 751.
- [51] Suryanarayana, C. and Norton, M.G., "X-Ray Diffraction: A Practical Approach", (Springer Science & Business Media, 1998).
- [52] Rezlescu, L., Rezlescu, E., Popa, P. and Rezlescu, N., *Journal of Magnetism and Magnetic Materials*, 193 (1999) 288.
- [53] Cullity, B.D. and Graham, C.D., "Introduction to Magnetic Materials", 2nd ed., (John Wiley & Sons, Hoboken, NJ, 2011).

-
- [54] Ahmad, M., Grössinger, R., Kriegisch, M., Kubel, F. and Rana, M., Journal of Magnetism and Magnetic Materials, 332 (2013) 137.
- [55] Stergiou, C. and Litsardakis, G., Journal of Magnetism and Magnetic Materials, 323 (2011) 2362.
- [56] Hemeda, D., Al-Sharif, A. and Hemeda, O., Journal of Magnetism and Magnetic Materials, 315 (2007) L1.
- [57] Ahmed, M., Okasha, N., Oaf, M. and Kershi, R., Journal of Magnetism and Magnetic Materials, 314 (2007) 128.

Chemical Characterization of Harmattan Dust across Oyo and Minna, Nigeria

O. A. Falaiye^a and F. O. Aweda^b

^a Department of Physics, University of Ilorin, Ilorin, Nigeria.

^b Department of Physics and Solar Energy, Bowen University, Iwo, Osun State, Nigeria.

Received on: 12/01/2019;

Accepted on: 15/10/2019

Abstract: Harmattan dust haze in Nigeria is due to annual deposition of very fine dust particles as a result of both natural and human activities. There are scanty reports on the mineralogical, elemental and heavy metal composition in the Harmattan dust blowing across the country to support the presence of minerals and elements in the Harmattan dust. The aim of this study is to assess minerals and elemental compositions of Harmattan dust variations across Oyo (7°32'N, 3°25'E) and Minna (9°35'N, 6°32'E), Nigeria. Harmattan dust samples were collected using clean plastic bowls of 10 cm diameter and analysis was conducted on the samples collected at the two stations using Fourier Transform Infrared Spectroscopy (FTIR), X-ray Fluorescence (XRF), Particle Induced X-ray Emission (PIXE) and Atomic Absorption Spectroscopy (AAS). It was observed that elements, such as K, Ca, Ti, Mn, Fe, Ni, Cu, Zn, Mo, As, Zr, Pb, V, Sr, Cr and Ce, were present in different concentrations in the samples collected. Minerals, such as Quartz [SiO₂], Rutile [TiO₂], Periclase [MgO], Corundum [Al₂O₃], Hematite [Fe₂O₃], Cuprite [Cu₂O], Baddeleyite [ZrO₂], Litharge [PbO], Monazite [P₂O₅], Zincite [ZnO], Montroydite [HgO] and Lime [CaO], were present in the samples collected at each station in different proportions. The soil mass concentration of the elements was calculated and observed to be 3.5179 μg m⁻³ at Oyo and 3.4745 μg m⁻³ at Minna. It was observed that the Harmattan dusts moving across Nigeria have almost all the elements present in Harmattan dust varying from station to station as the dust is moving towards the south of the country. The study concluded that the elemental composition of the dust samples analyzed revealed that the percentage compositions of some elements are higher than the acceptable WHO standard values, which may affect human health. It is therefore recommended that adequate precautionary measures and policies should be made to help mitigate the effects of high elemental concentrations observed.

Keywords: FTIR, PIXE, XRF, AAS, Mineralogy and element composition.

Introduction

The word Harmattan is a local term of dust storm gotten from the Twi language “haramata”, which perhaps is from Arabic “haram” forbidden thing. This is a dry dusty wind that emanated from the Sahara blowing towards the West Africa coast of the world continent, which precisely started from November to March of every year. More so, the Harmattan in America is also known as a dry dusty wind that blows

from the Sahara in North Africa towards the Atlantic affecting both domestic and commercial activities during its period.

Harmattan dust lifting, transportation and deposition occur naturally (Kalu [1], Falaiye et al. [2], Adimula [3], Falaiye et al. [4]). This could be a result of wind transportation that moves the dust from the source and deposits it along the trajectory path. The Harmattan period

is usually associated with low and poor visibility of the atmosphere, which is sometimes less than 1000 m (Falaiye et al. [2], Adimula et al. [3], [4]). Falaiye et al. [5] reported that the more the Harmattan dust mass in the air, the less the visibility of both human and animal.

The wind that blows Harmattan dust across Nigeria is the north east trade wind. This wind causes different types of ailments, such as dry skin, cough, catarrh and respiratory-related diseases, which are mostly reported in hospitals during the Harmattan period (Carlson and Prospero [6], Shutz [7]). Studies have shown that the Harmattan season occurs from the month of November to the month of March of the following year in Nigeria (Falaiye [4]).

During this period, the atmosphere is laden with dust, thus reducing visibility and causing domestic as well as outdoor activities' inconvenience (Aweda et al. [8]). During the period of this study (November – March), the West African region experiences the prevailing north-easterly wind regime known as Harmattan (Adimula et al. [3]). Junge [9] reported that on the average, it takes about twenty-four hours for the Harmattan to reach the Northern part of Nigeria from its source. Bertrand et al. [10] reported that dust particles are deposited over the region where dust plumes predominantly originate from the *Bôdélé* depression in the Chad Basin. This fact has been pointed out by various meteorological observers according to Samway [11].

Different authors have worked on the mechanisms of the path way of dust on the Cape Verde Islands as reported by (Glaccum and Prospero [12], Talbot et al. [13]). Since the majority of land-derived sediments in this part of the Atlantic Ocean are of Aeolian origin, often the erogenous sediment fraction was taken to be windblown (deMenocal et al. [14], Moreno et al. [15], Sarnthein [16]).

In another vein, admixtures of fluvial-transported or laterally advected sediments were also found to play a role in Harmattan dust as well (Holz et al. [17], Koopmann [18], Ratmeyer et al. [19], Zabel et al. [20]). In Harmattan dust production, Chad Basin was estimated to be up to 6.3×10^8 and 7.1×10^8 t/yr in 1981 and 1982, respectively (McTanish and Walker [21]).

Studies have been conducted on the pollutant concentrations in the ambient air (Obiajunwa et

al. [22]). This is powerful and widely used for the purpose of identifying the dominant sources of dust (Owoade et al. [23], Cohen et al. [24], Mooibroek et al. [25]). The emission rate that increases the range of air pollutants associated with iron smelter process (Brook et al. [26], Pope and Dockey [27], Zhang et al. [28], Tai et al. [29]) in the part of south west contributes to the increase of iron concentration. The light-absorbing species in the atmosphere play a major role in the block carbon of the aerosol climatic forcing and visibility degradation (Malm et al. [30], Jacobson [31] and Bond et al. [32]).

Heavy metals, such as As, Cd and Cr, are part of the constituents of particulate matter with iron and steel production (Cohen et al. [33]) in some parts of Nigeria. Hence, this study focuses on the assessment of trace elementals and minerals in Harmattan dust in the selected locations and their effects on the human health.

Material and Methods

(A) Sample Collection

A dry standard plastic bowl of a diameter of 10 cm and a height of 40 cm was used to collect each of the Harmattan samples across the two selected stations. This plastic bowl was kept in a wire gauge of (100x100x100 cm) firmed on the top of residential buildings, so as to prevent the dust from reptiles and wind disturbance. The choice of plastic bowl was taken, because the bowl has a heavy weight that can prevent wind from blowing it away and dust can settle in it successfully. In Nigeria, plastic bowl is one of the important materials used for domestic and commercial purposes. Different precautionary measures were put in place to avoid contamination by keeping the plastic in a polythylene box (60x60x60 cm) with a hole on its sides for aeration. See Fig. 1. Distilled water was also exposed on an elevated platform and in residential buildings at the two locations: Oyo (7°32'N, 3°25'E) and Minna (9°35'N, 6°32'E). The maps of sampling locations are shown in Figs. 2 and 3. Some of the bowls were exposed to collect dust particles from November for a period of one week or one month, while some were exposed to collect the dust samples for a period of five months (November to March), respectively. A total of ten (10) samples were collected and stored in desiccators prior to the analysis in order to avoid contamination which could influence the results. This experiment

follows the method adopted by Falaiye et al. [4] and Falaiye and Aweda [5], where Petri dishes were exposed on an elevated platform to collect Harmattan dust samples in order to conduct mineralogical and chemical analysis. During the collection process, as reported by Falaiye et al.

[4], measures such as keeping the sample containers away from public roads and highways were taken into consideration in order to minimize contamination by the local dust. However, the experimental setup for this research is shown in Fig. 1 below.

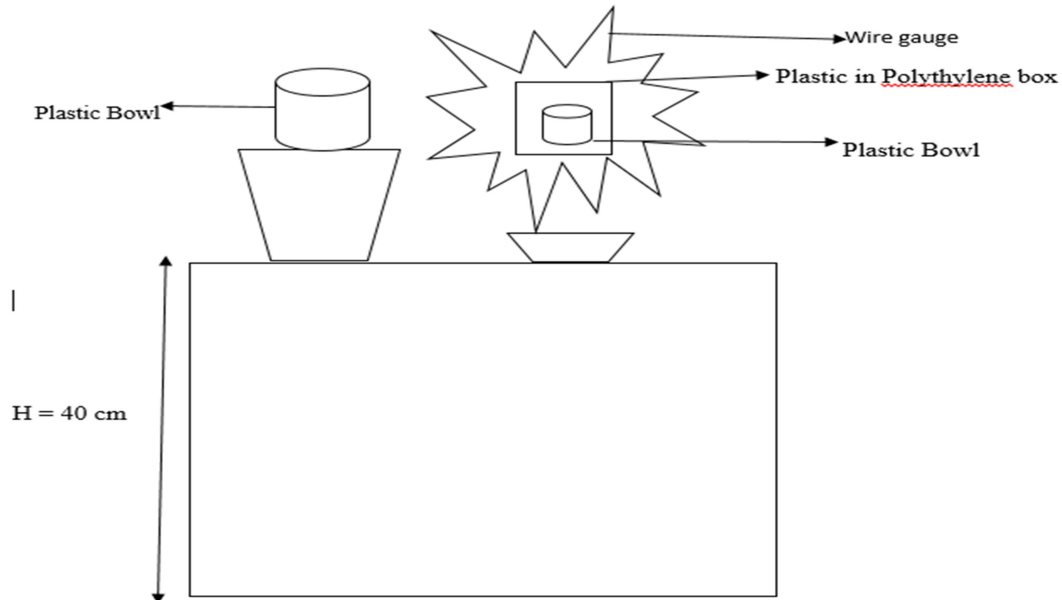


FIG. 1. Schematic diagram of the experimental setup for sample collection.

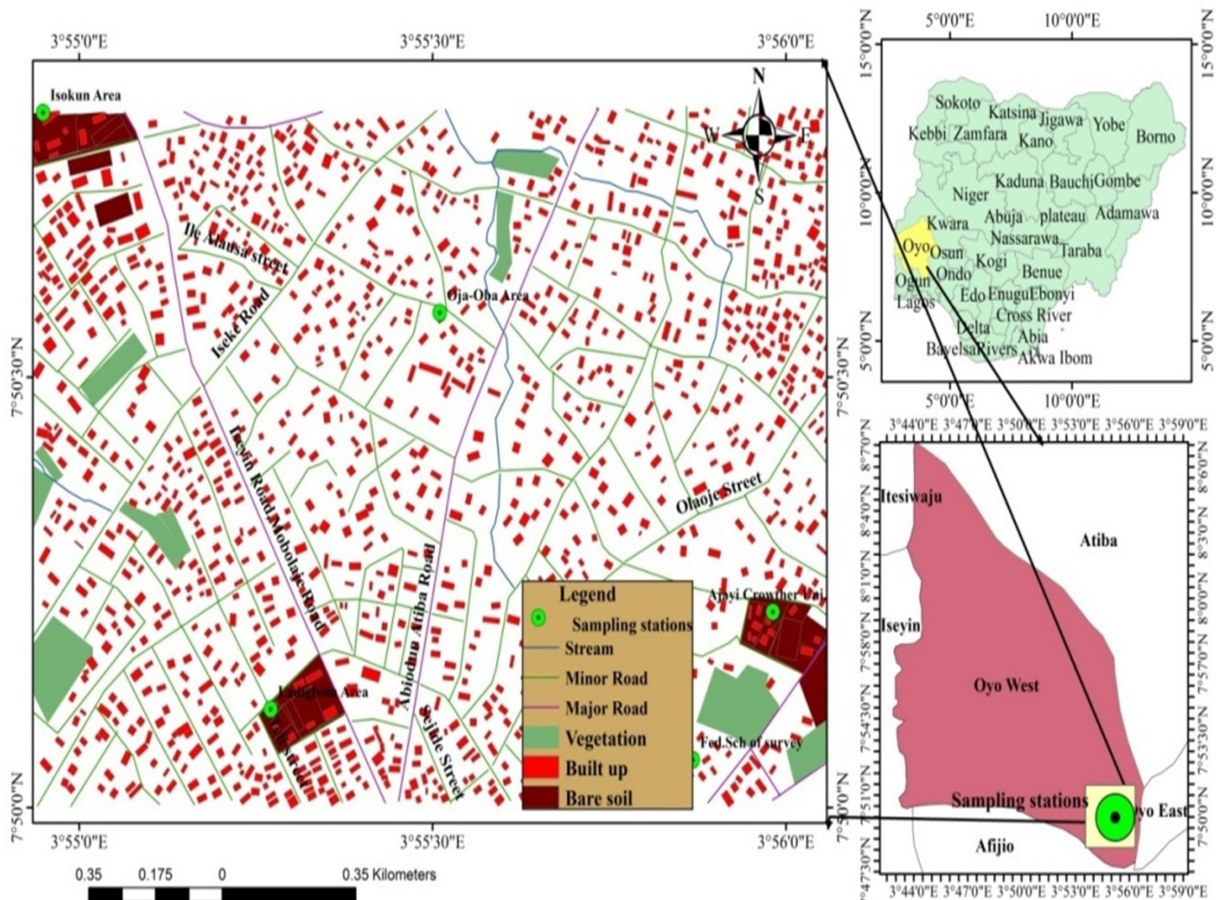


FIG. 2. Map of Oyo showing the sampling location.

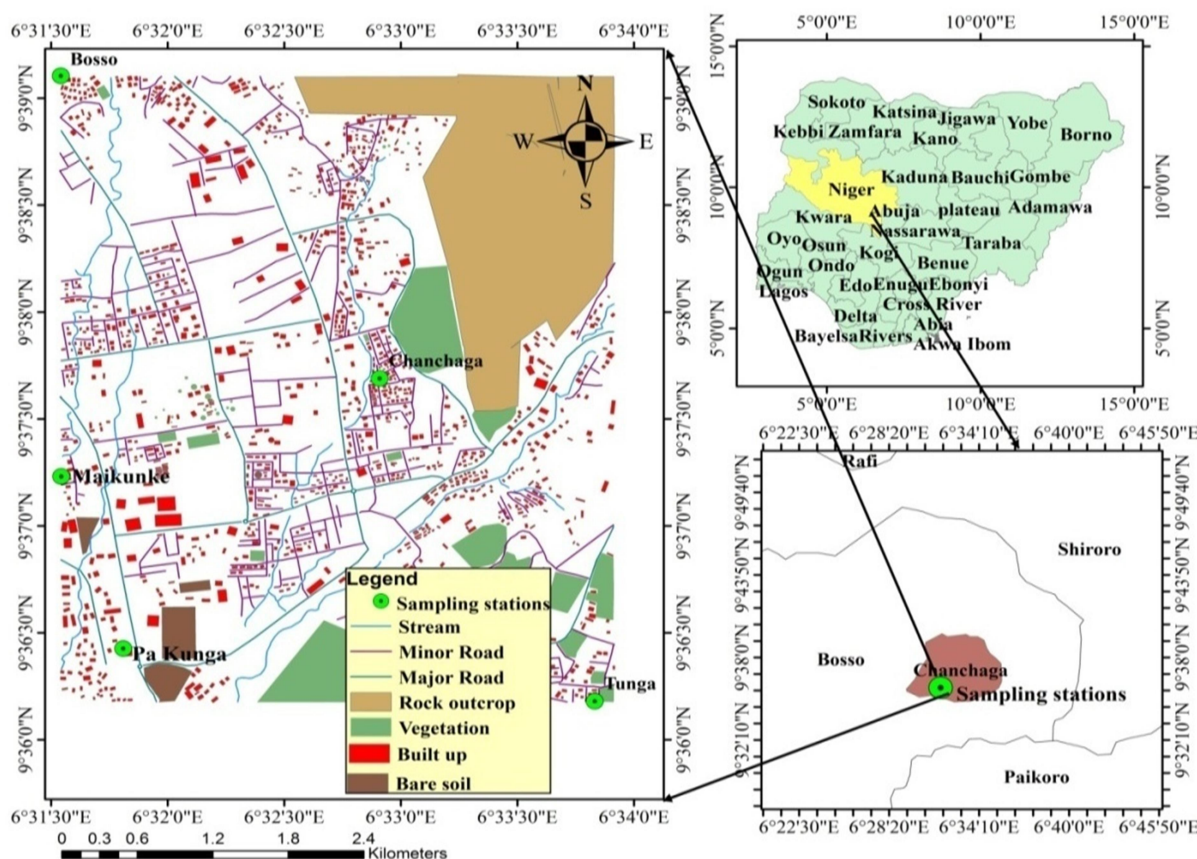


FIG. 3. Map of Minna showing the sampling location.

TABLE 1. Coordinates of different sampling locations across each station.

Location	Longitude (N)	Latitude (E)	Elevation (m)
Minna Area			
Bosso	9°39'17.13"	6°31'39.73"	909
Maikunkele	9°41'11.48"	6°28'24.39"	1026
Tunga	9°35'40.78"	6°33'54.80"	868
Pa Kungu	9°35.849'	006°31.487	597
Chanchaga	09°33'11.16"	06°34'58.19"	744
Oyo Area			
Federal School of Survey	7°50'31.86"	3°56'57.98"	1030
Ajayi Crowther University	7°50'13.49"	3°56'06.19"	1030
Isokun Area	7°50'49.22"	3°54'57.58"	937
Ladigbolu Area	7°49'11.45"	3°55'07.68"	973
Oja-Oba Area	7°50'58.33"	3°55'47.79"	951

(B) Sample Preparation and Characterization

The dry Harmattan dust samples were pelletized before being analyzed. Pelletization of the samples was done with steel mold pellets and a hydraulic press. Aluminum foil was used as the binder to hold the sample particles together after their removal from the molds. Thereafter, the samples were transferred into the accelerator for the XRF and PIXE employed in the research analysis.

Mineralogical and elemental analyses were carried out on the Harmattan dust gathered across the two stations under consideration. The analyses were carried out using the following characterization techniques: PIXE, XRF, FTIR and AAS, to determine the minerals and elements present in the samples collected across the two stations.

(C) Machines Used and Their Description

The elemental analysis of the Harmattan dust samples was carried out using the Energy Dispersive X-ray Fluorescence (EDXRF) spectrometry, Particle-Induced X-ray Emission, Fourier Transform Infrared Machine (FTIR) and Atomic Absorption Spectroscopy (AAS). The spectrometer brand name of EDXRF is ECLIPSE III, supplied by AMTEK INC. MA; USA. It is a self-contained miniature X-ray tube system. The detection system for all the measurements is of Model XR-100CR which is a high-performance X-ray detector with a preamplifier and a cooler system which uses a thermoelectrically cooled Si-PIN photodiode as an X-ray detector. The power to the XR-100CR is provided by a PX2CR power supply. The detector is coupled to the pocket MCA 8000A Multichannel Analyzer. The resolution of the detector for the 5.9 keV peak of ^{55}Fe is 220 eV FWHM with 12 μs shaping time constant for the standard setting and 186 eV FWHM with 20 μs time constant for the optional setting. The optional setting was used for measurements with a resolution of 186 eV for the 5.9 peak of ^{55}Fe . The Particle-Induced X-ray Emission machine with the name National Electrostatics Corporation Model 5SDH pelletron which is a 1.7MV tandem electrostatic ion acceleration was used for the analysis. This system is designed to accelerate light ions for material science research using such techniques as Rutherford backscattering, PIXE, hydrogen profiling and implantation and nuclear physics experiments. However, it is also capable of producing low current of heavy ions. This technique can be applied to different sample materials which include geological, archaeological, biological, material science and environmental pollution in which Aerosol samples are classified. The detailed setup of the proton-induced X-ray emission technique (PIXE) setup used for this work was reported by Ezech and Obiajunwa [34] and it was briefly described by Ezech et al. [35]. The accelerator tank is linked with the charge exchange ion (beam) source which is equipped with hydrogen and helium. The Fourier Transform Infrared Machine (FTIR) manufactured by Agilent Technologies with the model number CARY 630FTIR was used for the analysis of the liquid samples. The Atomic Absorption Spectroscopy (AAS) with model number PG990 was used for the analysis of the liquid samples.

(D) Sample Preparation Using EDXRF and PIXE

The Harmattan dust samples analyzed were dried and pelletized. The pelletization of the samples is done with steel molds, pellets and a hydraulic press, by aluminum foil as the binder, to hold the sample particles together after their removal from the molds.

(E) Sample Preparation Using AAS and FTIR

The samples collected at each location were taken to the laboratory for analysis using Atomic Absorption Spectroscopy (AAS). The samples were digested before taking them for the elemental analysis using AAS. The digestion process was done in a fume cupboard for safety purposes, by measuring 50 ml of each waste water sample (4 samples) and adding 5 ml of hydrochloric acid, followed by boiling till 20 ml. They were all filtered and the filtrates were taken for chemical analysis using PG990 model buck scientific AAS. For FTIR, the samples collected at each location were taken to the laboratory for analysis using Fourier Transform Infrared Machine (FTIR) manufactured by Agilent Technologies with the model number CARY 630FTIR. The sample liquid was shaken vigorously and then a little quantity of the sample was dropped on the sensor part of the machine where a software installed on a computer was used to determine the spectrum

Results and Discussion**A. Elemental Composition and Concentrations**

Elemental concentrations of Harmattan dust collected in Oyo and Minna include: Cu, Zn, Fe, Pb, Ca, Mn, Ni, As, K, Ti, Mo, V, Sr and Zr. Table 2 reveals the elements present in Oyo. Fig. 4 shows the spectrum of the elements present in the samples as obtained from PIXE results for samples from Oyo. The order of magnitude of the concentration values is: $\text{Ca} > \text{Fe} > \text{K} > \text{Ti} > \text{Mn} > \text{Pb} > \text{Zn} > \text{V} > \text{Ni} > \text{Cu} \geq \text{Sr} > \text{Mo} > \text{As}$.

Calcium (Ca) was discovered to be of highest concentration in the samples at Oyo and Minna. This was due to some activities taking place at Oyo during the sampling collection.

TABLE 2. Average concentrations of metals in different elemental forms as revealed by PIXE for solid sample collected across Oyo.

	A (mg/L)	B (mg/L)	C (mg/L)	D (mg/L)	E (mg/L)	Average (mg/L)
K	32506	32453	32453	32453	32400	32453
Ca	82898	82799	82799	82799	82700	82799
Mn	4080	3000	3580	3540	3500	3540
Fe	82364	82344	82358	82354	82350	82354
Ni	504	450	474	484	474	474
Cu	300	253	250	256	203	253
Mo	100	96	97	98	99	98
As	100	92	96	98	94	96
Zr	300	256	200	250	253	253
Pb	777	778	779	780	776	778
V	550	450	400	560	490	490
Sr	200	143	173	176	170	173
Cr	143	200	170	173	176	173

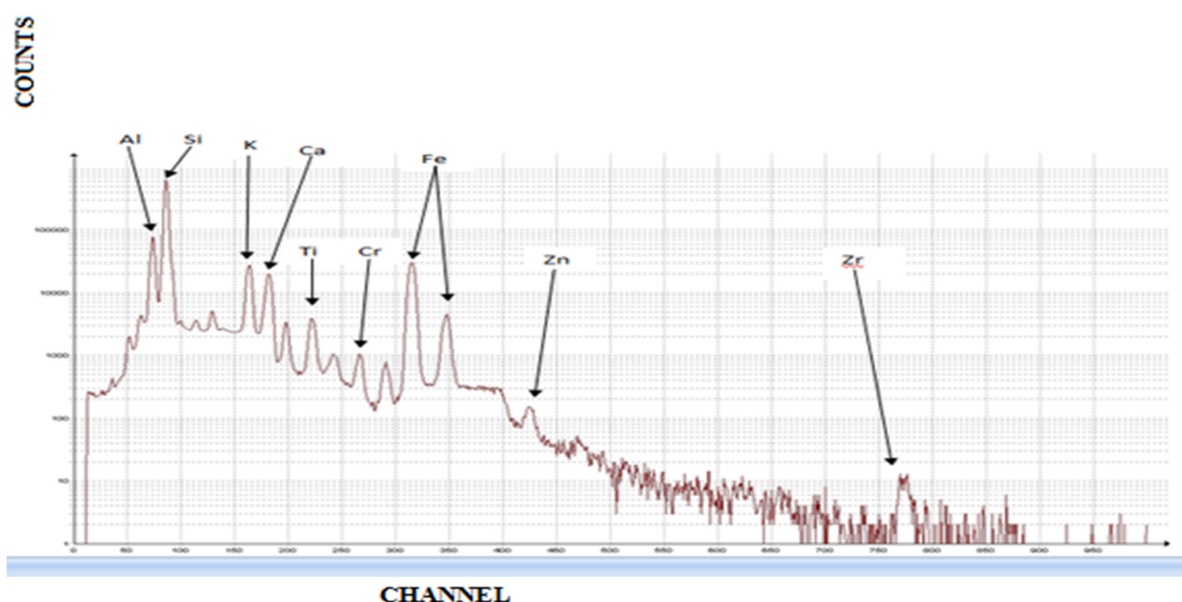


FIG. 4. PIXE spectrum of Harmattan dust sample from Oyo deposit.

The sampling locations were labelled with different letters which are: A (Federal School of Survey), B (Ajayi Crowther University), C (Isokun), D (Ladigbolu) and E (Oja-Oba). These locations are in the ancient part of Oyo town in Oyo State, Nigeria, as shown in Fig. 2. They are also represented with different coordinates, as shown in Table 1.

Table 3 reveals the elemental concentrations as observed in the Harmattan dust collected at Minna. The sampling locations were labelled

with different letters which are: F (Bosso), G (Maikunkele), H (Tunga), I (Pakungu), J (Chanchaga). These locations are in Minna Township in Niger State, Nigeria as shown in Fig. 3. They are also represented with different coordinates, as shown in Table 3. These coordinates represent the point at which the samples were collected across each station during the process of the research. Fig. 5 shows the spectral result of the samples collected at Minna during the period of the study.

TABLE 3. Average concentrations of metals in different elemental forms as revealed by PIXE for solid sample collected across Minna.

	F (mg/L)	G (mg/L)	H (mg/L)	I (mg/L)	J (mg/L)	Average (mg/L)
K	28384	28192	28192	28192	28000	28192
Ca	112054	111054	111554	111554	111554	111554
Mn	2416	1016	1716	1716	1716	1716
Fe	65000	61662	63331	63331	63331	63331
Ni	190	177	164	177	177	177
Cu	93	73	83	80	86	83
Mo	50	42	36	42	42	42
As	58	20	38	18	20	28
Zr	202	196	196	196	190	196
Cr	900	832	866	866	866	866
Ti	6387	6380	6394	6387	6387	6387
Ce	866	860	860	878	878	866
Pb	248	248	240	256	248	248
Zn	291	291	291	291	291	291

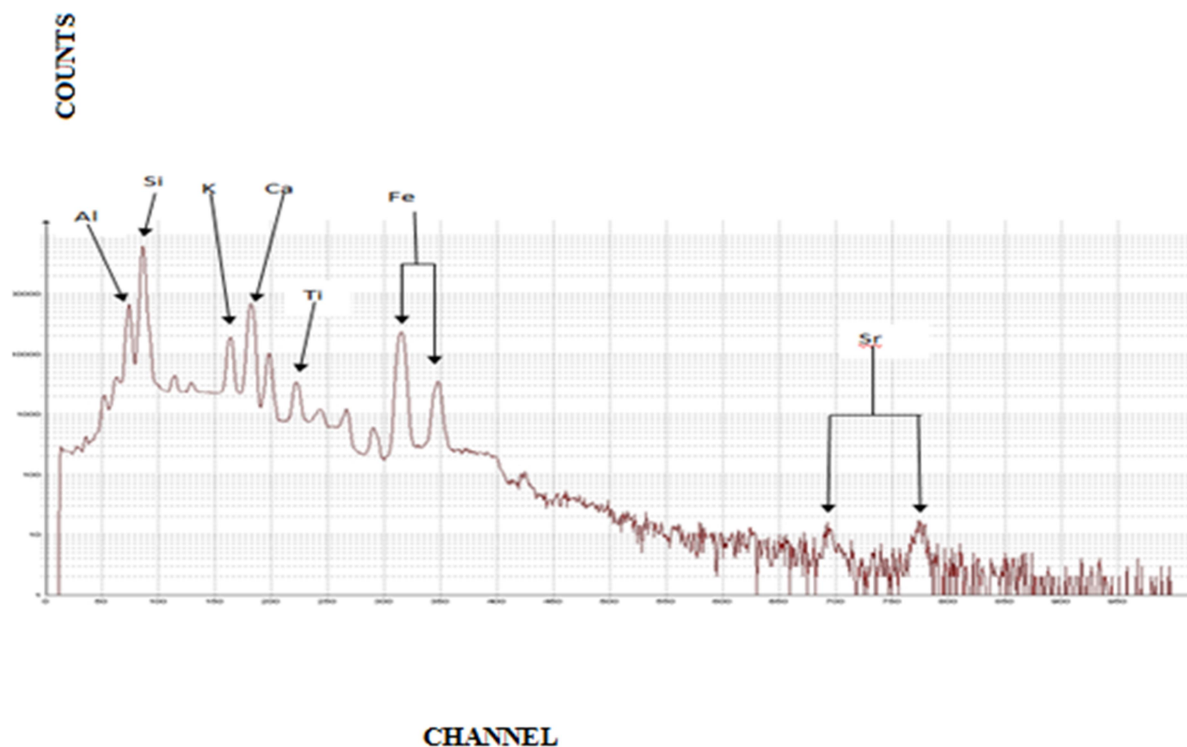


FIG. 5. PIXE spectrum of Harmattan dust sample from Minna deposit.

The soil mass concentration of the elements present in the samples collected across the two stations under consideration was also calculated. It was observed that the soil mass concentration collected in Minna was determined to be $3.4745\mu\text{g}/\text{m}^3$ while the soil mass concentration for Oyo was observed to be $3.5179\mu\text{g}/\text{m}^3$. The value for Oyo was found to be higher than the value for Minna as a result of activities taking place during the collection of the samples, such as highway vehicular activities, road side kitchens and many more.

B. Health Implications of Elemental Dust Composition

From the liquid samples, it was observed that there is a presence of lead (Pb) particulate matter in the air. This may be a result of the activities taking place in the environment of the sample collection. These activities include fossil fuel combustion (including vehicles), metal processing industries and waste incineration around the sample collection area, as reported by Isozaki et al [36]. However, research has shown that the little amount of Pb can be harmful to

human beings, more especially little babies and young children, as their bodies are prone to the absorption of high elements (Chineke and Chiemeka [37]). As reported by Chineke and Chiemeka [37], if much of Pb is inhaled by a pregnant woman, it may affect the health of the unborn child. Since lead is one of the toxic elements, it will be considered that the presence of lead in Oyo may be as a result of the activities taking place in the Isokun area of Oyo town, where we have heavy vehicular movements, particularly of articulated vehicles. As reported by Chineke and Chiemeka [37], the Air Quality Archive [38] and WHO [39], the acceptable value of potassium in the air as recommended by WHO was observed to be 8.7 mg/m^3 . Meanwhile, the two stations Oyo and Minna have average values of potassium to be higher than the recommended value, which could be a result of accumulation of the dust for a long period of time during the sample collection. But, the presence of the high value of the element may be a result of the accumulation of the dust in the dust collector before taking it to laboratory for analysis.

Table 4 shows the elemental concentrations as revealed by AAS machine using the liquid

sample collected across each location. However, other elements, such as Zn, Fe, Mn, Ni, As, K, Mo, V, Sr and Zn, present in the dust samples collected at the two stations, revealed that dusts that blow across the country (Nigeria) have some of the toxic elements which may be harmful to human health. As reported by Chineke and Chiemeka [37], the presence of Zinc (Zn) in the air is essential in the elemental composition of Harmattan dust, because Zn is indispensable for human health and for all living organisms. However, research has shown that Zn, though useful and needed for good health, can be toxic to human health if the concentration is far higher than the WHO recommendations over an extended period of time (Chineke and Chiemeka [37], the Air Quality Archive [24], WHO [25]). However, for this study, it can be observed that the acceptable levels of Zn and iron in the air are the same. This is also reported by Chineke and Chiemeka [37]. This indicates that the level of Zn in Oyo and Minna shows a high value as compared with the WHO standard. This may be due to some activities taking place at the two stations, such as road construction, metal work (which makes use of zinc-based materials) and vehicular movement around the station.

TABLE 4. Mean concentrations of metals in different elemental forms as revealed by AAS.

Elements	Na	K	Ca	Mg	Fe	Cd	Zn	Mn	Cu	Cr	Pb
Oyo (ppm)	6.27	4.37	1.883	2.67	8.366	0.157	0.18	-0.054	-0.043	1.931	0.22
Minna (ppm)	19.7	44.94	23.149	9.967	2.376	0.157	7.587	0.631	-0.043	-0.205	0.25
WHO (ppm)	0.005	8.7	0.4	0.4	0.4	5.0	0.4	0.01	0.03	0.5	0.15

This shows that the Harmattan dusts that blow across the two stations under consideration are far above the WHO recommended dosage of iron in the human body. This could be a result of the activities going on in all the environments such as vehicular movement and industrial activities that may be taking place in the area. The human health risk was assessed on the basis of observed mean concentration of the particulate matter of the trace elements and its location, based on the exposure. Human health is assumed to be exposed to significant amounts of the trace elements in the samples collected across the two stations considered. Naturally, inhalation is one of the primary sources of direct exposure to dust particles in every part of the country. More so, the non-carcinogenic risks of some of the trace metals (Cu, Zn, Fe, Pb, Mn, Ni, As, K, Mo, V, Sr and Zn) for children and adults were estimated for road site and urban background elevated from the site.

C. Mineralogical Composition

Mineralogical study of Harmattan dust samples collected at Oyo and Minna, carried out using PIXE analyzer, shows minerals such as Quartz [SiO_2] (82.4%) with a specific gravity of 2.65, which predominantly dominates the samples. Other minerals present in the samples are in lower quantity, (Check Table 5 for details). Studies have shown that the Harmattan dust mineralogies have major components, such as; quartz, haematite, illite, micas, feldspars, kaolinite, chlorite and other accessory minerals, as reported by Adedokun et al. [40], Jimoh [42] and Falaiye et al. [4]. Adedokun et al. [40] at Ile-Ife and Falaiye et al. [4] at Ilorin reported higher mineral contents in Harmattan dust than for the present study. This discrepancy could be a result of different instruments used for analysis: Adedokun et al. [40] and Falaiye et al. [4] used X-ray Diffraction (XRD) machine while in the present study PIXE machine was used.

TABLE 5. Percentage proportions of minerals present in Harmattan dust at Oyo and Minna compared to those of Ile-Ife (Adedokun et al. [40]) and Ilorin (Falaiye, et al. [4]) using XRD machine.

Mineral	Specific Gravity	Ilorin (%)	Ile-Ife (%)	Oyo (%)	Minna (%)
Quartz [SiO_2]	2.65	76.47	74.78	82.4	75.6
Gibbsite [$\text{Al}(\text{OH})_3$]	2.35	7.09	-	-	-
Rutile [TiO_2]	4.2	5.78	-	0.45	0.44
Goethite [$\text{Fe}_2\text{O}_3 \cdot \text{H}_2\text{O}$]	4-4.2	4.59	-	-	-
Halloysite [$\text{Al}_4\text{Si}_4\text{O}_{10}(\text{OH})_8 \cdot 8\text{H}_2\text{O}$]	2.6	3.93	1.45	-	-
Kaolinite [$\text{Al}_4\text{Si}_4\text{O}_{10}(\text{OH})_8$]	2.6	2.09	10.29	-	-
Microcline [KAlSi_3O_8]	2.56	-	17.63	-	-
Mica [Si_4O_{10} Sheet Structure]	2.7-3.1	-	2.54	-	-
Periclase [MgO]	3.56	-	-	0.61	0.39
Corundum [Al_2O_3]	4.0-4.2	-	-	5.00	7.23
Zincite [ZnO]	5.66	-	-	5.66	0.06
Hematite [Fe_2O_3]	5.26	-	-	5.71	6.51
Cuprite [Cu_2O]	6.13-6.15	-	-	0.03	0.02
Baddeleyite [ZrO_2]	5.4-6.02	-	-	0.09	0.08
Litharge [PbO]	9.14	-	-	-	-
Monazite [P_2O_5]	4.6-5.4	-	-	0.24	0.12
Montroydite [HgO]	11.23	-	-	0.001	-
Lime [CaO]	1.97	-	-	-	6.81

(Source of Specific Gravity: Read [41]).

(I) Mineralogical Composition of Harmattan Dust Using FTIR Spectrum

Fig. 6 (A and B) shows the quantitative analysis carried out on the liquid samples collected at the stations considered for this research. Prominent FTIR absorption peaks were

studied to determine functional groups present which correspond to the minerals present in the dust samples. These minerals were identified with the available instruments to determine the quantities present in the samples collected.

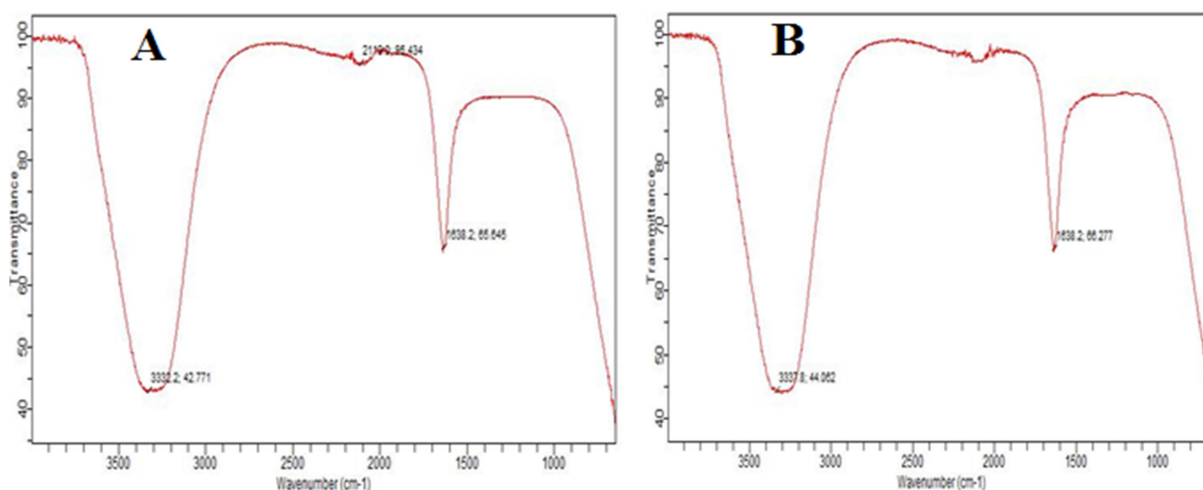


FIG. 6. A typical FTIR spectrum for Oyo (A) and Minna (B).

(II) Composition of Quartz Mineral

From the FTIR spectrum in Fig. 6, the absorption band appearing at 1638.2 cm^{-1} and 1015.7 cm^{-1} suggests the presence of quartz in the samples. The bending vibration at 1971.9 cm^{-1}

and symmetrical stretching vibration at 1922.3 cm^{-1} are assigned. The pattern of absorption in quartz can be explained by ascribing the 1971.9 cm^{-1} band region (Si-O asymmetrical bending vibration), the band region 1994.1 cm^{-1} (Si-O symmetrical bending vibrations) and the bands

in the region 1966.2 cm^{-1} (Si-O symmetrical stretching vibrations). It was observed that there are about four to six peaks in the samples collected across each location.

(III) Composition of Clay Minerals

The presence of kaolinite, illite and montmorillinite indicated clay minerals in the samples collected across all these locations. Kaolinite is said to be a clay mineral in crystallization which occurs in the monoclinic system and forms the major constituent of Nigeria clay. It is also shown that Harmattan dust in the air reduces the visibility of air craft that may lead to air crash in some periods because of the dusts that are lifted high as far as the stratospheric region of the atmosphere before dropping into the lower atmosphere after travelling to a very long distance (Falaiye and Aweda [5], Aweda et al. [8], Falaiye and Aweda [43]). It can be observed from Fig. 6 (A and B) that the FTIR absorption peaks appearing at 1015.7 cm^{-1} in the sample indicate kaolinite.

Conclusion

This research concluded that quartz percentage of Oyo is higher than those observed at Minna, Ilorin and Ile-Ife as a result of some activities taking place in the city during sampling collection. In another vein, the presence of elements in the samples gathered across Oyo and Minna shows that the dusts in Nigeria may have almost all the elements present in Harmattan. Some of the elements are in lower quantity and some are in high quantity. However, these elements can affect light as they pass through the atmosphere by scattering and absorption. More so, the study revealed that the elemental composition of the dust samples analyzed has higher percentages compared with the acceptable standard values (as recommended by WHO) for human health. It is therefore recommended that adequate precautionary measures and policies should be made to help mitigate the effects of high elemental concentrations observed. For proper verification of Harmattan dust effect on human health, daily collection of the dust is recommended.

References

- [1] Kalu, A. E. "The African dust plume: Its characteristics and propagation across West-Africa in winter". In: Morales, C. (Ed.) Saharan dust Mobilization Transport Deposit, SCOPE 14, (John Wiley, 1979), pp. 95-118.
- [2] Falaiye, O.A., Aro, T.O. and Babatunde, E.B., Zuma J. of Pure and App. Science, 5 (2) (2003) 197.
- [3] Adimula, I. A., Falaiye, O. A. and Adindu C.L., Centrepont (Science Edition), 16 (2008) 15.
- [4] Falaiye, O.A., Yakubu, A.T., Aweda, F.O. and Abimbola, O.J., Ife Journal of Science. 15 (1) (2013) 175.
- [5] Falaiye, O.A., Aweda, F.O. and Yakubu, A.T., FUTA Journal of Research in Sciences, 13 (1) (2017) 158.
- [6] Carlson, T.N. and Prospero, J.M., J. of App. Met., 2 (1972) 283.
- [7] Shutz, L., Annals of the New York Academy of Science, 338 (1980) 512.
- [8] Aweda, F.O., Falaiye, O.A. and Babatunde, J.G., Journal of Applied Science and Environmental Management, 21 (7) (2017) 1313.
- [9] Junge, C., "The importance of mineral dust as atmospheric constituents". Scientific Committee on Problems of the Environment. SCOPE Report: 14, (John Wiley and Sons, Chichester and New York, 1979).
- [10] Bertrand, J., Cerf, A. and Domergue, J.K., WMO, 538 (1979) 409.
- [11] Samway, J., Savanna, 4 (1975) 187.
- [12] Glaccum, R.A. and Prospero, J.M., Mar. Geol., 37 (34) (1980) 295.
- [13] Talbot, R.W., Harriss, R.C., Browell, E.V., Gregory, G.L., Sebach, D.I. and Beck, S.M., J. Geophys. Res., 91 (D4) (1986) 5173.
- [14] deMenocal, P.B., Ortiz, J., Guilderson, T.P., Adkins, J., Sarnthein, M., Baker, L. and Yarusinsky, M., Quat. Sci. Rev., 19 (2000) 347.

- [15] Moreno, A., Targarona, J., Henderiks, J., Canals, M., Freudenthal, T. and Meggers, H., *Quat. Sci. Rev.*, 20 (2001) 1327.
- [16] Sarnthein, M., Thiede, J., Pflaumann, U., Erlenkeuser, H., Fütterer, D., Koopmann, B., Lange, H. and Seibold, E., "Atmospheric and oceanic circulation patterns off northwest Africa during the past 25 million years". In: *Geology of the Northwest African Continental Margin*, edited by U. Von Rad, K. Hinz, M. Sarnthein and E. Seibold. (Springer, New York, 1982), pp. 545-604.
- [17] Holz, C., Stuut, J.-B.W. and Henrich, R., *Sedimentology*, 51 (5) (2004) 1145.
- [18] Koopmann, B., *Reihe C*, 35 (1981) 23.
- [19] Ratmeyer, V., Fischer, G. and Wefer, G., *Deep Sea Res., Part I*, 46 (8) (1999) 1289.
- [20] Zabel, M., Bickert, T., Dittert, L. and Haase, R.R., *Paleoceanography*, 14 (6) (1999) 789.
- [21] McTarnish, G.H. and Walker, P.H., *Geomorphology*, 26 (1982) 417.
- [22] Owoade, K.O., Hopke, P.K., Olise, F.S., Ogundele, L.T., Fawole, O.G., Olaniyi, B.H., Jegede, O.O., Ayoola, M.A. and Bashiru, M.I., *Atmospheric Pollution Research*, 6 (2015) 107.
- [23] Obiajunwa, E.I., Johnson-Fatokun, F.O., Olaniyi, H.B. and Olowole, A.F., *Nuclear Instruments & Methods in Physics Research, Section B-Beam Interactions with Materials and Atoms*, 194 (2002) 65.
- [24] Cohen, D.D., Crawford, J., Stelcer, E. and Bac, V.T., *Atmospheric Environment*, 44 (2010) 320.
- [25] Mooibroek, D., Schaap, M., Weijers, E.P., Hoogerbrugge, R., *Atmospheric Environment*, 45 (2011) 4180.
- [26] Brook, R.D., Franklin, B., Cascio, W., Hong, Y.L., Howard, G., Lipsett, M., Luepker, R., Mittleman, M., Samet, J., Smith, S.C. and Tager, I., *Circulation*, 109 (2004) 2655.
- [27] Pope, C.A. and Dockery, D.W., *Journal of the Air & Waste Management Association*, 56 (2006) 709.
- [28] Zhang, Y., Wen, X.-Y., Wang, K., Vijayaraghavan, K. and Jacobson, M.Z., *Journal of Geophysical Research: Atmospheres*, 114 (2009) D22305.
- [29] Tai, A.P.K., Mickley, L.J. and Jacob, D.J., *Atmospheric Environment*, 44 (2010) 3976.
- [30] Malm, W.C., Day, D.E. and Kreidenweis, S.M., *Journal of the Air & Waste Management Association*, 50 (2000) 701.
- [31] Jacobson, M.Z., *Nature*, 409 (2001) 695.
- [32] Bond, T.C., Doherty, S.J., Fahey, D.W., Forster, P.M., Berntsen, T., DeAngelo, B.J., Flanner, M.G., Ghan, S., Karcher, B., Koch, D., Kinne, S., Kondo, Y., Quinn, P.K., Sarofim, M.C., Schultz, M.G., Schulz, M., Venkataraman, C., Zhang, H., Zhang, S., Bellouin, N., Guttikunda, S.K., Hopke, P.K., Jacobson, M.Z., Kaiser, J.W., Klimont, Z., Lohmann, U., Schwarz, J.P., Shindell, D., Storelvmo, T., Warren, S.G. and Zender, C.S., *Journal of Geophysical Research-Atmospheres*, 118 (2013) 5380.
- [33] Cohen, A.J., Anderson, H.R., Ostro, B., Pandey, K.D., Krzyzanowski, M., Kuenzli, N., Gutschmidt, K., Pope, C.A., Romieu, I., Samet, J.M. and Smith, K.R., "Mortality Impacts of Urban Air Pollution. In: *Comparative Quantification of Health Risks: Global and Regional Burden of Disease Due to Selected Major Risk Factors*", edited by Ezzati, M., Lopez, A.D., Rodgers, A. and Murray, C.U.J.L., Vol. 2, (World Health Organization, Geneva, 2004).
- [34] Ezeh, G.C. and Obiajunwa, E.I., *J. Fundam. Appl. Sci.*, 9(1) (2017) 499.
- [35] Ezeh, G.C., Ugwo, J.P., Adebisi, F.M., Abiye, O.E., Onwudiegwu, C.A. and Obiajunwa, E.I., *Human and Ecological Risk Assessment: An International Journal*, (2018) 1549.
- [36] Isozaki, A., Morita, Y., Okutani, T. and Matsumura, T., *Analytical Science*, 12 (5) (1996) 755.
- [37] Chineke, T.C. and Chiemeka, I.U., *Africa Physical Review*, 3, 0018 (2009) 125.
- [38] The Air Quality Archive, "Air Pollution: Causes of air pollution", (The UK National Information, 2003).

- [39] WHO, "Air Quality Guideline for Europe II", 2nd edition, (WHO Regional Publications, European Series No. 91, 2000).
- [40] Adedokun, J.A., Emofurieta, W.O. and Adedeji, O.A., J. of Theor. and App. Clim., 40 (3) (1989) 161.
- [41] Read, H.H., "Rutley's Elements of Mineralogy", 26th Edition, (Jolly and Barber, Ltd., Rugby, Great Britain, 1973).
- [42] Jimoh, W.L.O., Research Journal of Environmental and Earth Sciences, 4 (4) (2012) 428.
- [43] Falaiye, O.A. and Aweda, F.O., Journal of Applied Science and Environmental Management, 22 (2) (2018) 281.

Physical Properties of RhCrZ (Z= Si, Ge, P, As) Half-Heusler Compounds: A First-Principles Study

B. Amrani^a, A. Chahed^a, M. Rahmoune^a, K. Benkaddour^a and A. Sayede^b

^a *Condensed Matter and Sustainable Development Laboratory (LMCDD), University of Sidi Bel-Abbes, Sidi Bel-Abbes 22000, Algeria.*

^b *UCCS, CNRS-UMR 8181, Université d'Artois, Faculté des Sciences Jean Perrin, Rue Jean Souvraz, SP 18, 62307 Lens Cedex, France.*

Received on: 5/6/2019;

Accepted on: 7/11/2019

Abstract: We use the first-principles-based density functional theory with full potential linearized augmented plane wave method in order to investigate the structural, elastic, electronic, magnetic and thermoelectric properties of RhCrZ (Z= Si, Ge, P, As) Half-Heusler compounds. The preferred configurations of the RhCrZ alloys are all type α . The structural parameters are in good agreement with the available theoretical results. The Young's and shear modulus, Poisson's ratio, sound velocities, Debye temperature and melting temperature have been calculated. Furthermore, the elastic constants C_{ij} and the related elastic moduli confirm their stability in the cubic phase and demonstrate their ductile nature. The compounds RhCrSi, RhCrGe, RhCrP and RhCrAs are found to be half-metallic ferrimagnets (HMFs) with a half-metallic gap E_{HM} of 0.37, 0.35, 0.25 and 0.02 eV, respectively. The half-metallicity of RhCrZ (Z= Si, Ge, P, As) compounds can be kept in a quite large hydrostatic strain and tetragonal distortion. The Curie temperatures of RhCrSi, RhCrGe, RhCrP and RhCrAs compounds are estimated to be 952, 1261, 82 and 297 K, respectively, in the mean field approximation (MFA). Thermoelectric properties of the RhCrZ (Z= Si, Ge, P, As) materials are additionally computed over an extensive variety of temperatures and it is discovered that RhCrAs demonstrates higher figure of merit than RhCrSi, RhCrGe and RhCrP. The properties of half-metallicity and higher Seebeck coefficient make this material a promising candidate for thermoelectric and spintronic device applications.

Keywords: Heusler alloys, Electronic structures, Magnetic properties, Mechanical properties.

Introduction

The scientific community is engaged in finding a material candidate that has a conversion efficiency as high as possible [1]. The Heusler alloys have been immensely studied with respect to thermoelectric technology due to their unique properties, like half-metallic ferromagnetism, topological insulation and Weyl semimetallicity [2]. They also possess a special spin band behavior, where one of the spin densities shows typically a metallic behavior

while the other is semiconducting. Heusler alloys with chemical formulae of XYZ, X_2YZ and $XX'YZ$ (where X, X', Y = transition metals, Z = s, p element) have been found to be potential candidates for spintronic applications [3].

The concept of half-metallic ferromagnets was first introduced by de Groot et al. [4], on the basis of band structure calculations in NiMnSb and PtMnSb semi-Heusler phases. Half-metallic materials have been found theoretically in many

materials; for example, ferromagnetic metallic oxides [5], dilute magnetic semiconductors [6], zincblende compounds [7], full-Heusler compounds [8], half-Heusler compounds [9] and quaternary Heusler alloys [10].

Although numerous half-Heusler compounds have been predicted to be half-metallic by first-principles calculations [11-13], a comprehensive study of the structural, electronic and magnetic properties of the half-Heusler family is useful, because it is not clear which of the many half-metallic half-Heuslers that can be imagined are stable. Thus, a systematic study of the structural stability of the half-Heusler family should provide guidance for future experiments. Among these, the RhCrZ (Z= Si, Ge, P, As) compounds have not received much attention theoretically and experimental information on these compounds is also scarce.

Until now, no half-metallic gap E_{HM} , which is the minimum energy for the electron to change the spin, has been found in either theory or experiment investigations of these compounds. The characteristics of energy bands and origin of half-metallic gap were also not studied. In addition, the effect of volumetric and tetragonal strain on the half-metallicity character was not investigated. It is also interesting to estimate the Curie temperatures of the RhCrZ (Z= Si, Ge, P, As) half-Heusler compounds to see their potential application in spintronics. On the other hand, half-Heusler (HH) alloys are potential candidates for use in high-temperature thermoelectric materials [14-16]. HH compounds are also used for power generation, because they are cheaper, abundant in nature and environmentally friendly; i.e., free from toxic elements [17]. HH compounds have attracted attention, because they have high-power factors due to the combination of large Seebeck coefficients and moderately low electrical resistivity.

For all these reasons, we perform these calculations by using the full-potential augmented plane wave (FP-LAPW) in order to provide reference data for experimentalists and to complete existing theoretical works on these compounds. Our paper is organized as follows: theoretical background, results and discussion and a summary of the results.

Computational Method

The calculations were performed within the density functional theory (DFT) [18]. We use the full potential linear-augmented-plane waves plus local orbital (FP-LAPW) method [19], as implemented in the Wien2k package [20]. The exchange-correlation potential was treated under the generalized gradient approximation (GGA) [21]. The core and valence states were treated with the relativistic and scalar relativistic approach, respectively. The partial waves used inside the atomic spheres are expanded up to $l_{max} = 10$ with a matrix size $R_{mt} K_{max}$ equal to 8, where R_{mt} represents the smallest atomic sphere radii and K_{max} is the plane waves' cut-off. A 20x20x20 k -point mesh was used as base for which the first Brillouin zone was found to be sufficient in most cases. Within the (FP-LAPW) method, we impose a convergence criterion of 10^{-5} in the total energy and charge density to improve accuracy in the spin-polarized calculations.

Results and Discussion

Structural Properties

In general, half-Heusler alloys, XYZ, have CI_b structure [22], which is similar to the structure of a full-Heusler alloy (X_2YZ), the $L2_1$ structure, except missing one X. The elements of X and Y are alkali metals, transition metals or rare-earth metals and Z is a main group element. The Z atoms constitute the most electronegative part of the half-Heusler XYZ compounds, followed by the X atoms, leaving the Y atom as the electron donating constituent. The X_2YZ full-Heusler $L2_1$ type structure consists of four fcc sublattices. The unit cell contains four atomic positions, X at (0,0,0) and (1/2,1/2,1/2), Y at (1/4,1/4,1/4) and Z at (3/4,3/4,3/4). Due to missing one X atom, there are three atomic configurations for XYZ half-Heusler alloys, which are called α , β and γ types; type α : X (0.25, 0.25, 0.25), Y (0, 0, 0) and Z (0.5, 0.5, 0.5); type β : X (0.25, 0.25, 0.25), Y (0.5, 0.5, 0.5) and Z (0, 0, 0); type γ : X (0.5, 0.5, 0.5), Y (0.25, 0.25, 0.25) and Z (0, 0, 0). In all three atomic configurations, the (0.75, 0.75, 0.75) site is empty.

In the first step, in order to obtain the correct atomic arrangement and the magnetic ground state corresponding to the true ground state of the half-Heusler RhCrZ (Z= Si, Ge, P, As) compounds, we performed the energy

minimization as a function of lattice constant with respect to the three different possible site occupations for every non-magnetic (NM), ferromagnetic (FM) and antiferromagnetic (AFM) configurations and the obtained curves

are shown in Fig. 1 and Fig. 2. The calculated total energies within GGA as a function of volume are fitted to Murnaghan's equation of state to obtain the ground-state properties [23].

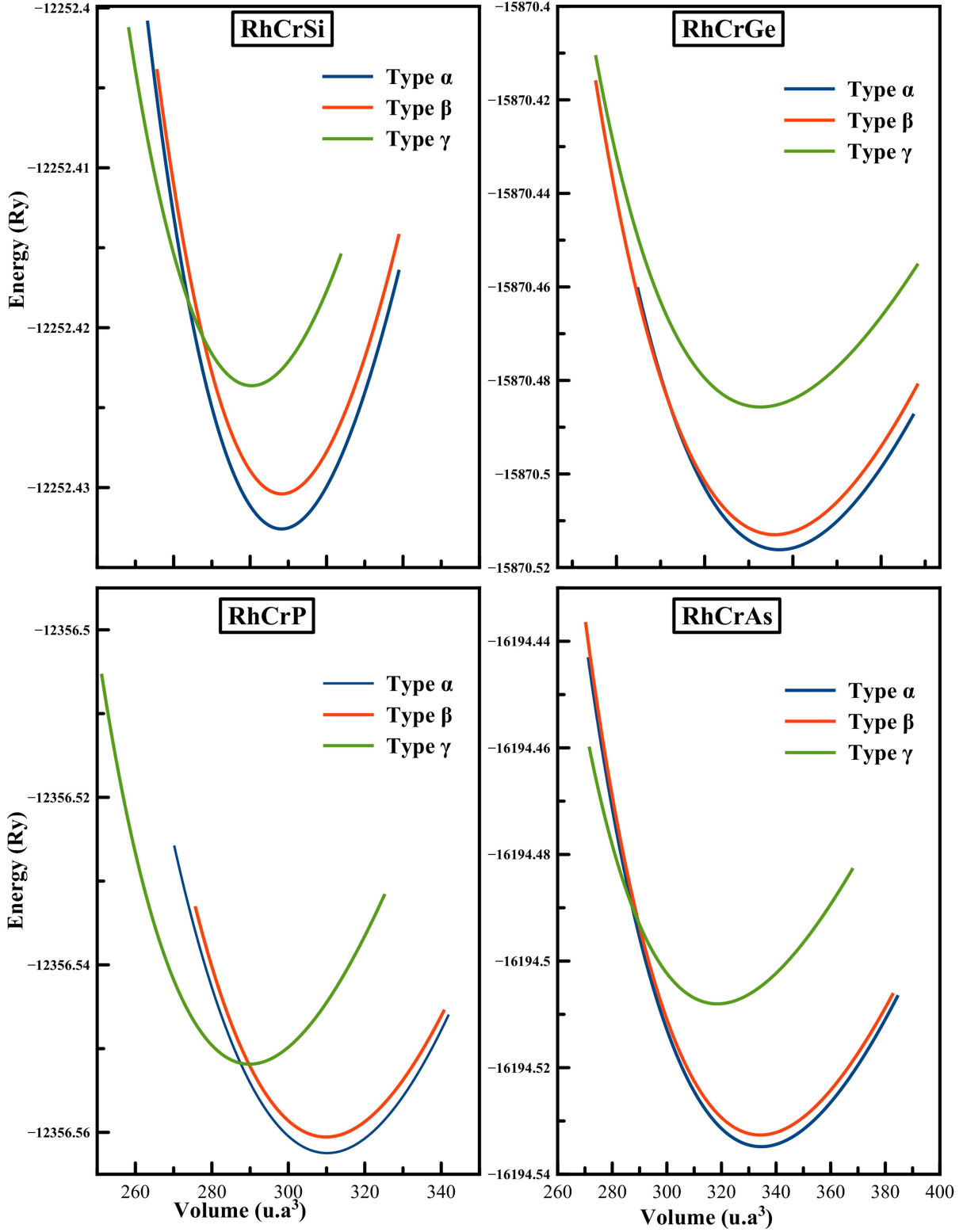


FIG. 1. Total energy as a function of volume per formula unit (f.u.) in the three atomic arrangements: type α , type β and type γ for the RhCrZ (Z= Si, Ge, P, As) compounds. The curves correspond to the FM state.

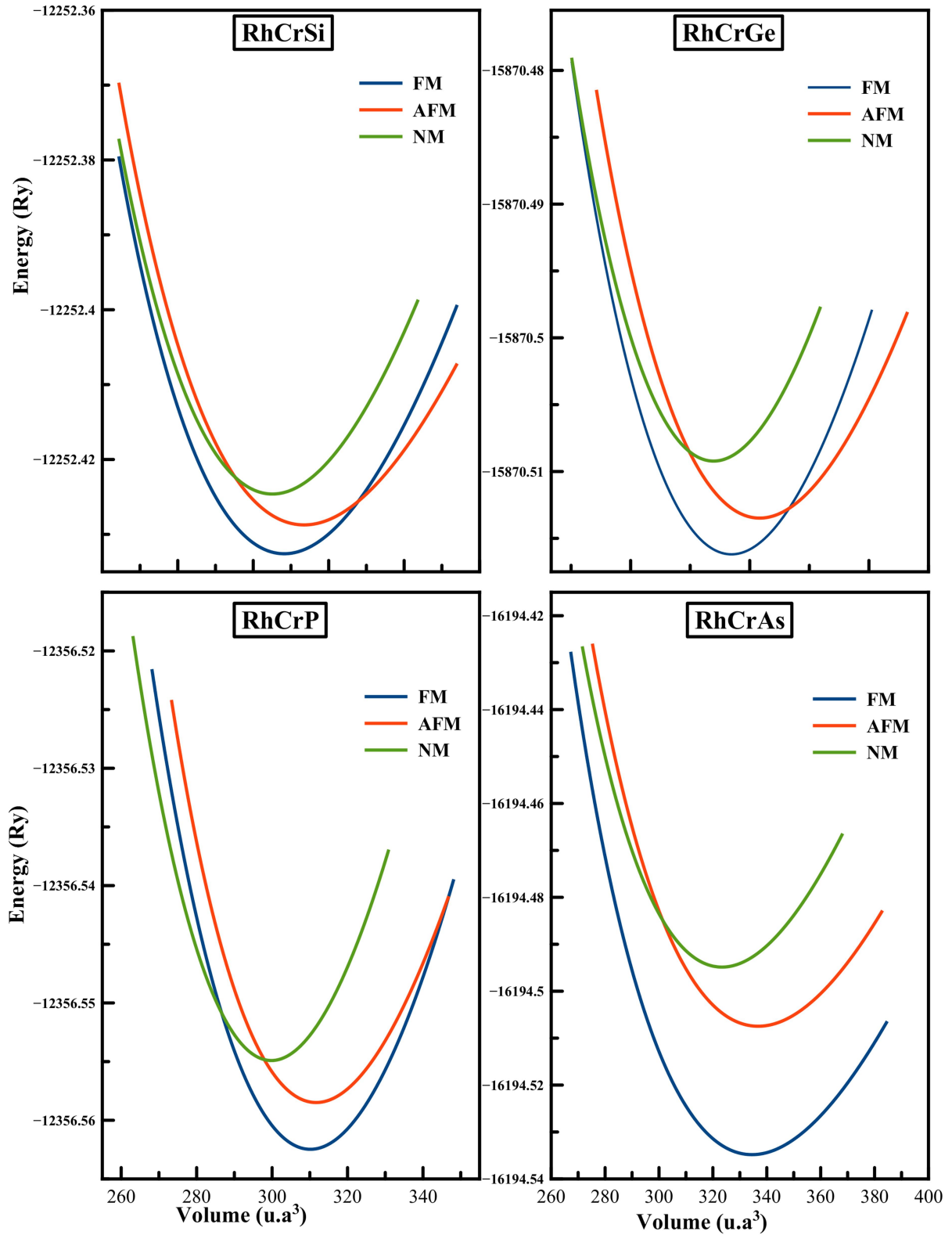


FIG. 2. Total energy as a function of volume per formula unit (f.u.) in the three magnetic states: FM, AFM and NM for the RhCrZ (Z= Si, Ge, P, As) compounds. The curves correspond to the type α structure.

As seen in Figs. (1,2), the optimization of the cubic lattice parameters for all three possible configurations in their respective three different magnetic configurations revealed the lowest energy for type α structure with a ferromagnetic

ground state for all compounds (type $\alpha + FM$). The obtained equilibrium lattice constants, bulk modulus and the corresponding total energies are presented in Table 1.

TABLE 1. Calculated total energies E_{tot} (in Ry) per formula unit, equilibrium lattice constant a_0 (in Å), the bulk modulus B (in GPa) and formation energy E_f (in Ry) for RhCrZ (Z= Si, Ge, P, As) half-Heusler compounds in their different structure types and magnetic configurations.

Compound	Structure	E_{tot} (Ry)			a_0 (Å)	B (GPa)	E_f (Ry)
		NM	FM	AFM	FM	FM	FM
RhCrSi	Type α	-12252.424612	-12252.432589	-12252.428423	5.6742	185.0286	-1.71
	Type β	-12252.424521	-12252.432396	-12252.430944	5.6745	184.4734	-1.697
					5.65 ^a	408.1 ^b	-2.486 ^a
					5.65 ^b		
	Type γ	-12252.384913	-12252.423623	-12252.407615	5.6279	154.8741	-1.669
RhCrGe	Type α	-15870.509219	-15870.516193	-15870.513548	5.7776	168.7817	-1.585
	Type β	-15870.504840	-15870.513131	-15870.492267	5.7795	144.9142	-1.573
					5.75 ^a	173.04 ^b	-0.761 ^a
					5.76 ^b		
	Type γ	-15870.479146	-15870.485676	-15870.481536	5.8613	140.2142	-1.511
RhCrP	Type α	-12356.554924	-12356.562472	-12356.558487	5.686	171.0891	-1.707
	Type β	-12356.530538	-12356.560651	-12356.553949	5.6842	171.5793	-1.696
					5.65 ^a	224.6 ^c	-3.981 ^a
					5.67 ^c		
	Type γ	-12356.473652	-12356.551856	-12356.548623	5.7363	135.4124	-1.672
RhCrAs	Type α	-16194.494862	-16194.534822	-16194.507464	5.8312	145.2174	-1.608
	Type β	-16194.494837	-16194.532635	-16194.507476	5.8294	144.7208	-1.550
					5.81 ^a	206.00 ^c	-1.644 ^a
					5.80 ^c		
	Type γ	-16194.502575	-16194.508025	-16194.506468	5.7363	135.4124	-1.558

^a [24], ^b [25], ^c [26]

Until now, there are no other experimental or theoretical results in the structure type α and only very few theoretical results have been reported for these compounds in the structure type β [24-26], which is not the most stable state, as shown in Figs. (1,2). However, this structure type β is closer to the structure type α than the structure type γ , as shown in Fig. 1 and Table 1. Our optimized lattice constants for our compounds show very good agreement with the recent available theoretical results [24-26] listed in Table 1. We believe that our calculated results are reliable and we propose a future experimental work to verify our calculated results. The highest calculated bulk moduli for RhCrZ (Z= Si, Ge, P, As) in type $\alpha + FM$ configuration confirm the stability of this structure.

The formation energy E_f determines whether a compound can be experimentally synthesized or not. E_f is the change in energy when a material is formed from its constituent elements in their bulk states and can be calculated for RhCrZ (Z= Si, Ge, P, As) compounds as:

$$E_f^{\text{RhCrZ}} = E_{\text{tot}}^{\text{RhCrZ}} - (E_{\text{Rh}}^{\text{Bulk}} + E_{\text{Cr}}^{\text{Bulk}} + E_{\text{Z}}^{\text{Bulk}});$$

$$Z = \text{Si, Ge, P, As} \quad (1)$$

where $E_{\text{tot}}^{\text{RhCrZ}}$ represents the first-principles calculated equilibrium total energy of the studied compounds per formula unit, $E_{\text{Rh}}^{\text{Bulk}}$, $E_{\text{Cr}}^{\text{Bulk}}$ and $E_{\text{Z}}^{\text{Bulk}}$ are the equilibrium total energies per atom of the pure constituent elements Rh, Cr, Si, Ge, P and As in their individual stable bulk structures. In Table 1, we give the values of formation energy for all types of structures and all magnetic configurations. The negative sign of formation energy values for the four alloys reported in this study implies that they can be experimentally fabricated. Also, according to Table 1, the calculated E_f values confirm the structural stability of type $\alpha + FM$ structure for all RhCrZ (Z= Si, Ge, P, As) compounds (high negative formation energy). Among them, RhCrSi is most easily synthesized because of its lowest formation energy. Based on this, all the further calculations on elastic, thermal, electronic, magnetic and thermoelectric properties of RhCrZ (Z= Si, Ge, P, As) were performed on this structure only; i.e in the type $\alpha + FM$ structure.

Elastic Properties

To confirm the stability of the studied compounds, the elastic properties have been studied. Since RhCrZ (Z= Si, Ge, P, As) compounds have cubic symmetry, we have calculated only three independent elastic parameters; C_{11} , C_{12} and C_{44} . The obtained elastic constant values for RhCrZ (Z= Si, Ge, P, As) compounds are given in Table 2. The bulk modulus values calculated from the theoretical values of the elastic constants $B = (1/3) (C_{11} + 2C_{12})$ is also listed in Table 2. The traditional mechanical stability conditions of the elastic constants in cubic crystal [27] are:

$$(C_{11} + 2C_{12}) > 0; \quad \frac{1}{2}(C_{11} - C_{12}) > 0;$$

$$C_{11} > 0; C_{44} > 0; C_{12} < B < C_{11} > 0 \quad (2)$$

Thus, these compounds are elastically stable as satisfying these restrictions indicating that the α -type +FM structure is a mechanically stable phase. It may be noted that the value of B (bulk modulus) calculated from the elastic constants has nearly the same value as the one obtained from energy minimization. This gives a good estimate of the precision and accuracy of the elastic constants' calculations performed in this article of our compounds.

TABLE 2. Calculated elastic constants C_{ij} (in GPa), Calculated Voigt shear modulus G_V (in GPa), Reuss shear modulus G_R (in GPa), shear modulus G (in GPa), bulk modulus B (in GPa), Young's modulus Y (in GPa), Poisson's ratio ν , anisotropy factor A and B/G ratio for RhCrZ (Z= Si, Ge, P, As) compounds.

Compound	C_{11}	C_{12}	C_{44}	G_V	G_R	G	B	Y	ν	A	B/G
RhCrSi	223.7255	168.951	123.7067	85.178	51.399	68.288	187.208	182.654	0.337	4,517	2.7414
	247.32 ^b	165.46 ^b	137.66 ^b			87.48		227.84 ^b	0.30 ^b	3.35 ^b	2.20 ^b
RhCrGe	222.348	142.4235	123.2154	89.913	67.208	78.56	169.064	204.071	0.298	3.084	2.152
	277.50 ^b	125.14 ^b	117.48 ^b			98.7 ^b		249.4 ^b	0.26 ^b	1.53 ^b	1.78 ^b
RhCrP	192.8669	166.2601	96.0693	62.962	27.538	45.25	175.128	124.985	0.381	7.221	3.87
	261.08 ^c	206.53 ^c	108.85 ^c					35.50 ^c	0.38 ^c	3.99 ^c	2.38 ^c
RhCrAs	161.0483	121.2655	104.2189	70.487	38.66	54.573	134.526	144.217	0.321	5.24	2.465
	249.82 ^c	184.60 ^c	115.80 ^c					187.00 ^c	0.34 ^c	3.50 ^c	2.90 ^c

^a [24], ^b [25], ^c [26].

From Table 2, it was observed that the C_{11} constant for the four half-Heusler compounds is larger than the C_{44} constant, which implies that the investigated compounds present a weaker resistance to pure shear deformation compared to the resistance to unidirectional compression. The elastic anisotropy parameter A plays an important role in engineering sciences to detect the micro-cracks in materials. The deviation from 1 shows the degree of elastic anisotropy possessed by a crystal. The obtained elastic constants are used to compute the anisotropy constant A [27], which is given by $A = 2C_{44}/(C_{11} - C_{12})$. According to the values of A listed in Table 2, all our RhCrZ (Z= Si, Ge, P, As) compounds show anisotropic behaviour and possess a low probability to develop micro-cracks or structural defects during their growing process. Also, we can clearly observe that the anisotropy decreases on insertion of the anion with large atomic size for each IV and V column, respectively. RhCrP is characterized by a strong anisotropy compared to the other three compounds. The main isotropic mechanical parameters; namely, bulk modulus B , shear

modulus G , Young's modulus Y and Poisson's ratio ν , which are the important elastic moduli for applications, are calculated from the elastic constants C_{ij} of the single crystal using the Voigt–Reuss–Hill approximation [28] by the following relations:

$$G_V = \frac{1}{5} (C_{11} - C_{12} + 3C_{44}) \quad (3)$$

$$G_R = \frac{5C_{44}(C_{11} - C_{12})}{4C_{44} + (C_{11} - C_{12})} \quad (4)$$

$$B_V = B_R = \frac{1}{3} (C_{11} + 2C_{12}) \quad (5)$$

$$G = \frac{1}{2} (G_V + G_R) \quad (6)$$

The Young's modulus Y and Poisson's ratio ν were calculated, which are related to the bulk modulus B and the shear modulus G by the following equations:

$$Y = \frac{9BG}{(3B + G)} \quad (7)$$

$$\nu = \frac{(3B - 2G)}{2(3B + G)} \quad (8)$$

Our results on Young's modulus (Y), shear modulus (G) and Poisson's ratio (ν) of the four

compounds using GGA are listed in Table 2. Shear modulus (G) and Young modulus (Y) can be considered as stiffness indicators. Our calculations of G and Y show clearly that RhCrGe is stiffer than RhCrSi \rightarrow RhCrAs \rightarrow RhCrP.

Having acquired the necessary data, three parameters are used to estimate the ductile or brittle nature of these compounds. The Cauchy pressure ($C_{12} - C_{44}$), Pugh's index of ductility (B/G) and Poisson's ratio (ν). Present values of Cauchy pressure ($C_{12} - C_{44}$) for all our compounds RhCrZ (Z= Si, Ge, P, As) are positive; therefore, these compounds are ductile in nature. According to Pugh criterion [29], the critical value (B/G) which separates the ductile and brittle was found to be 1.75. As mentioned in Table 2, this ratio is greater than 1.75 for all our compounds RhCrZ (Z= Si, Ge, P, As), which are classified as ductile materials. For brittle materials, the Poisson's ratio is less than 0.26; otherwise the material behaves in a ductile manner. The results displayed in Table 2 show that all our compounds RhCrZ (Z= Si, Ge, P, As) are also classified as ductile alloys. These different results are in overall agreement with the other theoretical results found for type β [25, 26] and reported in Table 2.

Thermal Properties

Study of thermal properties provides information about phase stability, melting point, strength and bonding nature, among other properties. We estimated that the Debye temperature θ_D performs a central role in determining thermal characteristics of materials as well as in the development and manufacturing of electronic devices. Also, Debye temperature is used to distinguish between high- and low-temperature regions in solids. As a rule of thumb, a higher θ_D implies a higher melting temperature and thermal conductivity. The

Debye temperature (θ_D) can be estimated from the average sound velocity, v_m , by the following classical relation [30]:

$$\theta_D = \frac{h}{k} \left[\frac{3n}{4\pi} \left(\frac{\rho N_A}{M} \right) \right]^{1/3} v_m \quad (9)$$

where h and k are the Plank's and Boltzmann's constants, respectively, n is the number of atoms per formula unit, N_A is the Avogadro's number, ρ is the density of the compound, M is the molecular mass per formula unit and v_m is the average wave velocity [30] which is given by:

$$v_m = \left[\frac{1}{3} \left(\frac{2}{v_t^3} + \frac{1}{v_l^3} \right) \right]^{-1/3} \quad (10)$$

where v_l and v_t are the longitudinal and transverse elastic wave velocities, respectively, which are obtained from Navier's equations [30]:

$$v_l = \left(\frac{3B+4G}{3\rho} \right)^{1/2} \quad (11)$$

$$v_t = \left(\frac{G}{\rho} \right)^{1/2} \quad (12)$$

The melting temperature (T_{melt}) is calculated from C_{11} using the following expression [30]:

$$T_{melt} = \left[553K + \left(\frac{5.91K}{GPa} \right) C_{11} \right] \quad (13)$$

The calculated Debye temperature, longitudinal, transverse and average elastic wave velocities and melting temperature at zero pressure for the present compounds are given in Table 3. In light of these results, the Debye temperature and the melting temperature are directly related to elastic constants and decrease from RhCrSi to RhCrGe and from RhCrP to RhCrAs, respectively. To the best of our knowledge, there is no other theoretical and experimental data existent for comparison. Anyway, further experimental works are desirable.

TABLE 3. The calculated sound velocity longitudinal v_l (in m.s⁻¹), sound velocity transverse v_t (in m.s⁻¹), average sound velocity v_m (in m.s⁻¹), Debye temperature θ_D (in K) and melting temperature T_{melt} (in K) for RhCrZ (Z= Si, Ge, P, As) compounds.

Compound	v_l	v_t	v_m	θ_D	T_{melt}
<i>RhCrSi</i>	6467.07	3203.73	3595.92	431.965	1875.2177
<i>RhCrGe</i>	5910.97	3166.17	3536.01	417.163	1867.0766
<i>RhCrP</i>	5921.09	2595.68	2930.73	351.324	1692.8433
<i>RhCrAs</i>	5189.29	2662.61	2982.24	348.578	1504.7954

Electronic Properties

The electronic band structure calculations are done to predict the electronic nature of RhCrZ ($Z = \text{Si, Ge, P, As}$) compounds. The majority and minority spins (spin-up and spin-down) band structure along the high symmetry direction of the first Brillouin zone are depicted in Fig. 3 (a-d) for RhCrSi, RhCrGe, RhCrP and RhCrAs, respectively. As can be seen in Fig. 3, all RhCrZ ($Z = \text{Si, Ge, P, As}$) compounds have shown half-metallicity, because the spin-up (majority) band structure has metallic intersections at the Fermi level, indicating clearly strong metallic nature, whereas the spin-down (minority) band structure exhibits a semiconductor behavior. Fig. 3 shows that in minority spin channel, all four compounds have an indirect band gap E_g (Γ -X). The half-metallic gap E_{HM} is defined as the minimum energy required to flip a minority-spin electron from the valance band maximum to the majority-spin Fermi level, as listed in Table 4. The calculated band gap values for the investigated compounds are listed in Table 4, along with the other previous theoretical calculations. The half-metallic gap E_{HM} is strongly influenced by group IV elements (Si,Ge) and group V ones (P,As) and decrease from RhCrSi to RhCrGe and from RhCrP to RhCrAs, respectively. It is clearly seen that the calculated indirect band gaps (Γ -X) are slightly larger than those obtained by M. Jianhua et al. [24] and are usually closes than those obtained by N. Mehmood et al. [25] and R. Ahmad et al. [26]. Unfortunately, so far, no experimental measurements for band gap E_g and no experimental or theoretical data for the half-metallic gap E_{HM} for the investigated compounds have been carried out to compare with. Our total magnetic moment per formula unit values calculated are found to be integer values (see Table 4); $1.00\mu_B$ and $2.00\mu_B$ for RhCrZ ($Z = \text{Si, Ge}$) and RhCrZ ($Z = \text{P, As}$), respectively, and obey the Slater-Pauling behavior of HM ferromagnets [31], $M_{tot} = (Z_{tot} - 18)$; here, M_{tot} and Z_{tot} are the total magnetic moment and the number of total valence electrons. Z_{tot} is 19 and 20 for RhCrZ ($Z = \text{Si, Ge}$) and RhCrZ ($Z = \text{P, As}$), respectively. In order to analyze the magnetic configurations of the half-metallic half-Heusler compounds, we also list in Table 4 the local magnetic moments at Rh, Cr and Z ($Z = \text{Si, Ge, P, As}$) sites.

As seen in Table 4, for all four half-metal compounds, the main contribution to the total magnetic moment is due to the relatively large moment on the Cr sub-lattice with much smaller antiferromagnetically aligned moments on the Rh sub-lattice. The increase in atomic number of Z elements causes weak hybridization, yielding the enhancement of the local magnetic moment at the Cr site. The small moments on Rh are due to the difficulty in magnetically polarizing Rh atoms and the magnetic moment on the Z ($Z = \text{Si, Ge, P, As}$) atoms are quite small. A small amount of magnetic moment is found in the interstitial region too. To explain the magnetic properties in these compounds, we calculate the spin-polarized total densities of states (spin-TDOS) and partial density of states (spin-PDOS) of the RhCrZ ($Z = \text{Si, Ge, P, As}$) compounds at their optimized lattice constant presented in Fig. 4 and Fig. 5. As it can be seen, the general structure total TDOS is similar in shape for our compounds. At the first glance, it can easily be visualized that total DOS is mainly contributed by the 3d states of Cr and 4d states of Rh, while p state of Z ($Z = \text{Si, Ge, P, As}$) near the E_F makes no significant contribution to the total DOS. For example, in RhCrGe compound, the large exchange splitting of the Cr-3d states leads to a large magnetic moment of $1.251\mu_B$ at the Cr site. The exchange splitting of the Rh-4d states is relatively small and induces a magnetic moment of $-0.163\mu_B$. The DOS of Ge atom is almost symmetrical, yielding a very small magnetic moment of $-0.075\mu_B$.

The total DOS (spin-TDOS) of the RhCrZ ($Z = \text{Si, Ge, P, As}$) compound has a gap in the minority spin states at the Fermi level. The origin of the band gap may be attributed to the strong hybridization between the Cr-3d and Rh-4d electrons. In addition, since the total DOS of our compounds is generally similar in shape, we can conclude that the Z element is not responsible for the band gap. However, the substitutions of Z element result in a shift in the Fermi levels. On the other hand, the reason of the absence of a semiconducting gap in the majority spin is due to the dominance of the Cr-3d and Rh-4d electrons with little contribution of Z-p around the E_F for all the RhCrZ materials.

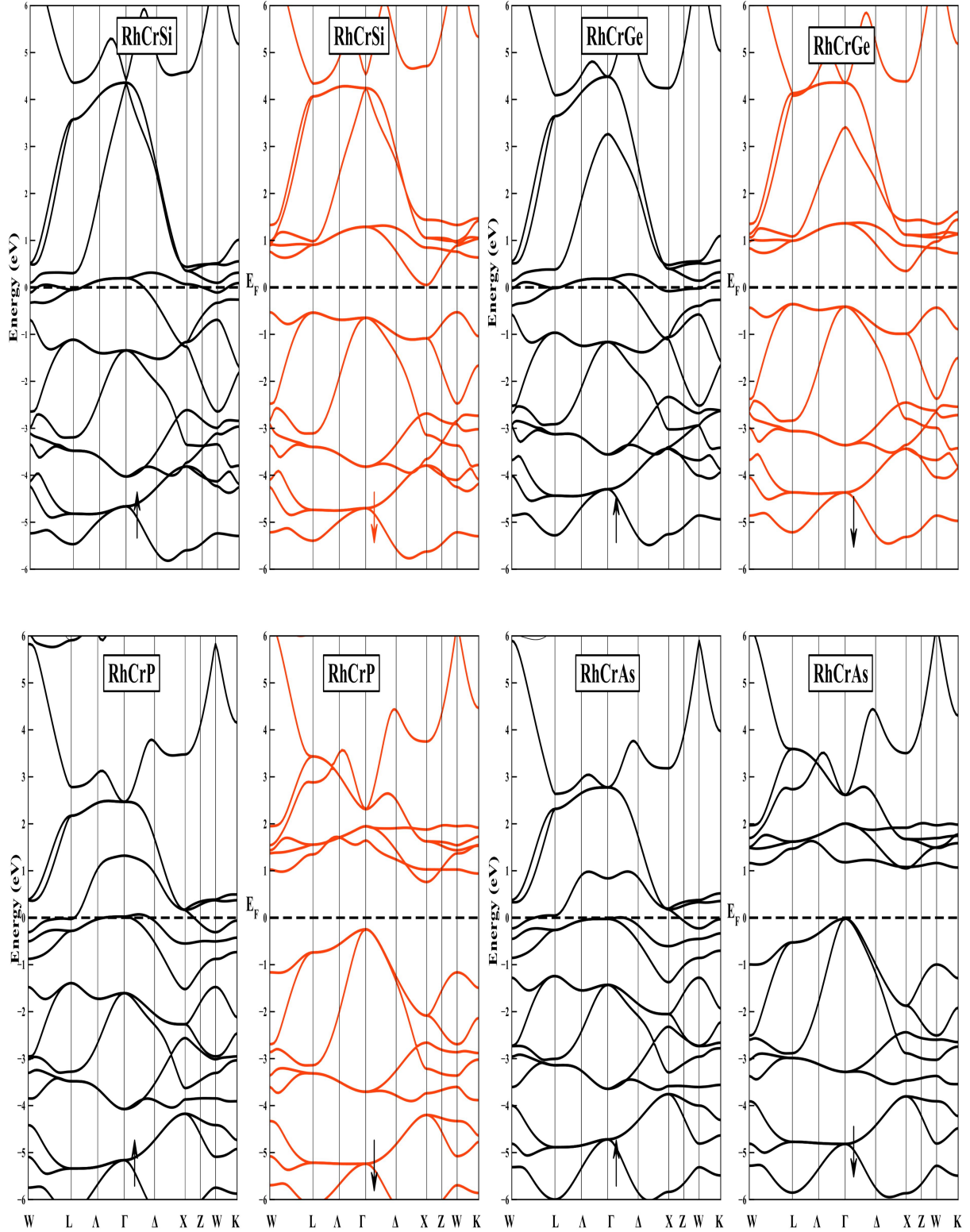


FIG. 3. Spin polarized band structure for the RhCrZ (Z= Si, Ge, P, As) compounds at their equilibrium lattice constants.

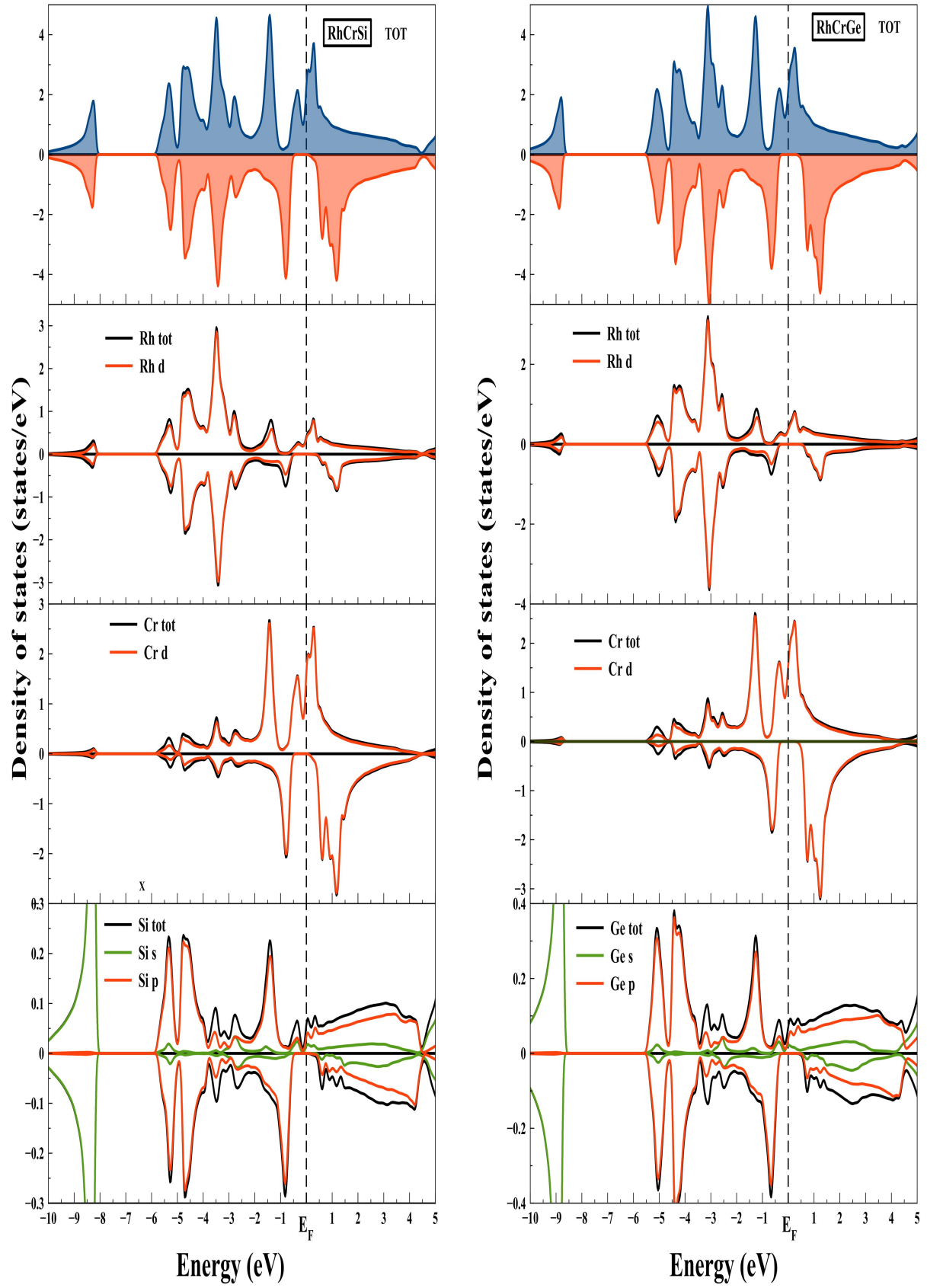


FIG. 4. Spin-polarized total and partial densities of states (DOS and P-DOS) of RhCrZ (Z= Si, Ge).

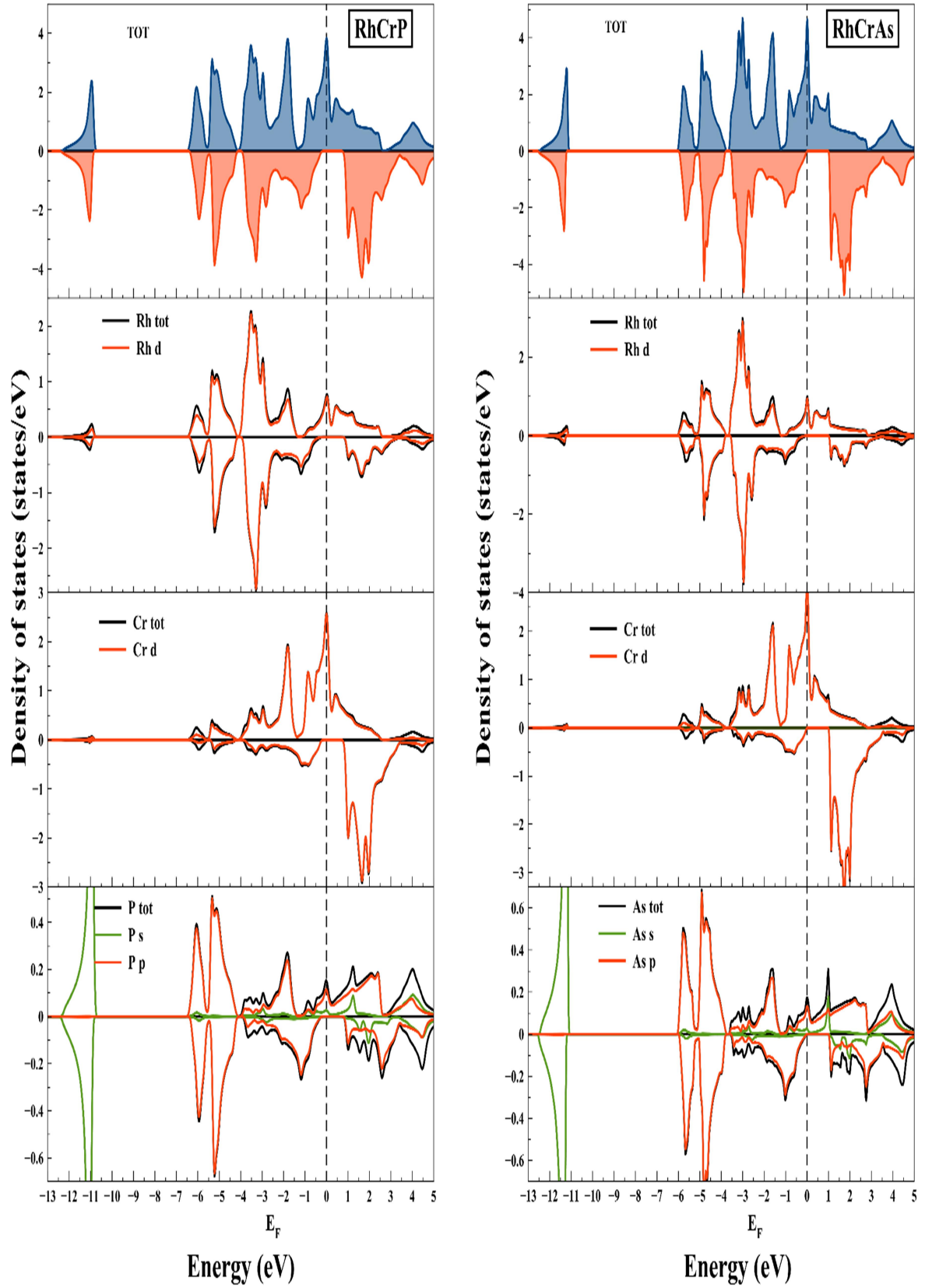


FIG. 5. Spin-polarized total and partial densities of states (DOS and P-DOS) of RhCrZ (Z= P, As).

TABLE 4. The semiconducting gap E_g^{I-X} (in eV), the half-metallic gap E_{HM} (in eV), total magnetic moment μ_{tot} (in μ_B), magnetic moment per atom (Rh, Cr, Si, Ge, P, As), magnetic moment in the interstitial region μ_{int} and Curie temperature T_c (in K) in compounds RhCrZ (Z= Si, Ge, P, As).

Compound	E_g	E_{HM}	μ_{tot}	μ_{Rh}	μ_{Cr}	μ_Z	μ_{int}	$T_c(^{\circ}K)$
<i>RhCrSi</i>	0.95		1	-0.113	1.182	-0.051	-0.018	
	0.57 ^a	0.37	1 ^a	-0.148 ^a	1.23 ^a	-0.093 ^a		951.163
	0.26 ^b		0.94 ^b	-0.22 ^b	1.28 ^b	-0.05 ^b	-0.06	
<i>RhCrGe</i>	0.71		1	-0.163	1.251	-0.075	-0.013	
	0.67 ^a	0.35	1 ^a	-0.191 ^a	1.293 ^a	-0.098 ^a		1261
	0.82 ^b		0.97 ^b	-0.11 ^b	1.17 ^b	-0.05 ^b	-0.03	
<i>RhCrP</i>	1.01		2	-0.204	2.214	-0.085	0.075	
	0.91 ^a	0.25	2 ^a	-0.234 ^a	2.297 ^a	-0.121 ^a		81.436
	1.49 ^c		2 ^c	-0.13 ^c	2.13 ^c	-0.07 ^c	0.08 ^c	
<i>RhCrAs</i>	1.06		2	-0.249	2.299	-0.111	0.061	
	0.95 ^a	0.02	2 ^a	-0.291 ^a	2.384 ^a	-0.135 ^a		296.4
	1.07 ^c		2 ^c	-0.15 ^c	2.35 ^c	-0.04 ^c	0.06 ^c	

^a [24] , ^b [25] , ^c [26]

Because half-metallic materials are usually prepared as thin films for spintronic applications, where the lattice constant of the half-metallic material strongly depends on the substrate lattice parameter and correspondingly the half-metallicity may be destroyed. The effect of the change of lattice constant (uniform strain) on the electronic and magnetic properties was preformed to test the robustness of the half-metallic properties in RhCrZ (Z= Si, Ge, P, As) alloys. The half-metallicity represented by the variations of the valence band maximum (VBM) and the conduction band minimum (CBM) in the spin-down direction as a function of lattice constant is exhibited in Fig.6(a). From Fig. 6(a), we can see that the RhCrSi, RhCrGe, RhCrP and RhCrAs Heusler alloys will maintain their half-metallic nature with the lattice constants in the wide range of 5.483 – 6.06 Å, 5.56 – 6.07 Å, 5.37 – 5.85 Å and 5.32 – 5.85 Å corresponding to -3.37% – 6.8%, -3.77% – 5.06%, -5.56% – 5.69% and -8.77% – 0.37%, respectively. As it can be seen, the half-metallicity of RhCrGe and RhCrP is more robust against lattice constant change than that of RhCrSi and RhCrAs equilibrium lattice constant. On the other hand, in the RhCrAs (RhCrSi) compounds, although their half-metallic gap E_{HM} is small, the half-metallicity is found to be more robust with respect to the lattice compression (expansion) and is maintained up to the lattice constant contraction of 8.77% (expansion of +6.8%), compared with both other compounds RhCrGe and RhCrP.

Compared to the uniform strain, the tetragonal distortion (in-plane strain) is more practical in potential spintronic applications. In fact, in the growth of thin films, the tetragonal distortion with fixed volume is most likely to occur and is one of the most undesired troubles for the growing process. To study the effect of a tetragonal distortion with the c/a ratio, the variations of valence band maximum (VBM) and conduction band minimum (CBM) as a function of the c/a ratio for the RhCrZ (Z= Si, Ge, P, As) compounds are shown in Fig. 6(b). We keep the unit-cell volume the same as the equilibrium bulk volume ($a \times a \times a = a^3$). It can be seen that the half-metallic character appears to exhibit a low sensitivity to a tetragonal distortion of lattice structure mainly for both RhCrGe and RhCrP compounds. In detail, the RhCrSi, RhCrGe, RhCrP and RhCrAs compounds can maintain their half-metallicity when the c/a ratio changes within the range 0.893 - 1.156, 0.85 - 1.19, 0.83 - 1.26 and 0.99 - 1.03, respectively. The CBM, VBM and band gap of minority spin channel are approximately maximum at the equilibrium lattice constant and the absolute values of them decrease monotonically with both positive and negative tetragonal strain.

Since the equilibrium lattice constants of RhCrSi (5.6742 Å), RhCrP (5.686 Å), RhCrGe (5.7776 Å) and RhCrAs (5.8312 Å) compounds are close to those of zinc blende semiconductors, such as GaAs (5.65 Å) and CdS (5.818 Å) [32], it is suggested to grow new HM Heusler alloys in the form of thin films on suitable substrates to get new candidates for spintronic applications.

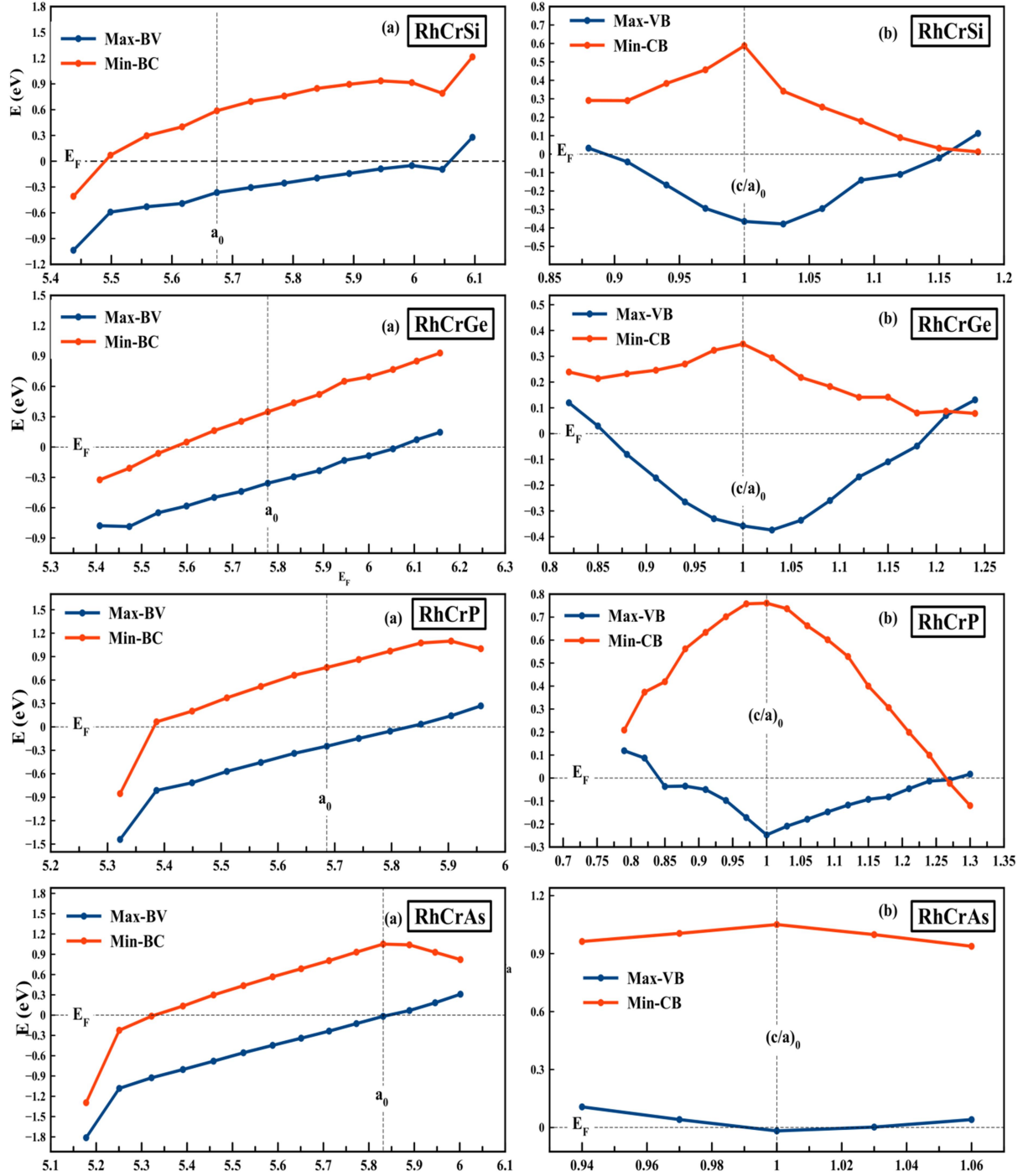


FIG. 6. Dependence of the HM state on the lattice constant (uniform strain) (a) at the c/a ratio (tetragonal distortion) (b) of RhCrZ (Z= Si, Ge, P, As) compounds. The blue lines correspond to the valence band maxima and the red lines correspond to the conduction band minima in the minority spin states (spin-down states).

The Curie temperature is another important aspect of application for spintronic materials. Using the mean field approximation (MFA) [33], the Curie temperature (T_C) can be calculated as:

$$T_C = \frac{2\Delta E}{3k_B} \quad (14)$$

where ΔE is the total energy difference between the antiferromagnetic and ferromagnetic states

($\Delta E = E_{AFM} - E_{FM}$) and k_B is the Boltzmann constant. The results are given in Table 4. The Curie temperature has been calculated to be 81.436 K, 296.4 K, 951.163 K and 1261 K for RhCrP, RhCrAs, RhCrSi and RhCrGe, respectively. The Curie temperature T_C is strongly influenced by group IV elements (Si, Ge) and group V ones (P, As) and increases

from RhCrSi to RhCrGe and from RhCrP to RhCrAs compounds, respectively. Among the four studied compounds, RhCrSi and RhCrGe seem to be the most suitable for applications, since they show the largest T_C . The Curie temperature of the half-metallic Mn_2VAl compound, estimated by using the mean field approximation, is 638 K and its value is in good agreement with the experimental value of the Curie temperature of 760 K [33].

Thermoelectric Properties

Thermoelectric (*TE*) materials transform the waste heat energy into usable electric energy, thereby offering a possible solution to the present-day energy crisis. This category of materials is currently being investigated at faster rates than other technologically important materials because of their ecofriendly and efficient energy management [34]. The thermoelectric properties of RhCrX ($X = Si, Ge, P, As$) compounds are calculated by the BoltzTrap code [35], which is related to the semiclassical Boltzmann theory and rigid band approach. In this study, we calculated the electrical conductivity σ , thermal conductivity κ , Seebeck coefficient S , thermopower factor PF and figure of merit ZT and the results are plotted in Fig. 7 and Fig. 8. An efficient thermoelectric material is required to have high electrical conductivity, a low thermal conductivity and a large Seebeck coefficient. To our information, the thermoelectric efficiency for the considered compounds has not been surveyed till now. The combined results of both spin channels to estimate overall thermal conductivity κ , electrical conductivity σ , Seebeck coefficient S , power factor PF and figure of merit ZT , can be expressed [36] respectively by:

$$\sigma = \sigma(\uparrow) + \sigma(\downarrow) \quad (15)$$

$$\kappa = \kappa(\uparrow) + \kappa(\downarrow) \quad (16)$$

$$S = [S(\uparrow) \cdot \sigma(\uparrow) + S(\downarrow) \cdot \sigma(\downarrow)] / [\sigma(\uparrow) + \sigma(\downarrow)] \quad (17)$$

$$PF = S^2 \sigma = S(\uparrow)^2 \cdot \sigma(\uparrow) + S(\downarrow)^2 \cdot \sigma(\downarrow) \quad (18)$$

$$ZT = T \cdot S^2 \cdot \sigma / \kappa \quad (19)$$

The variation of the electrical conductivity σ as a function of temperature is plotted in Fig. 7(a). We see that the electrical conductivity increases mostly linearly with temperature for all compounds. This could be justified by the fact that increasing temperature enhances thermal energy of the electrons to freely form a high-conducting state.

Fig. 7(b) displays the temperature dependence of thermal conductivity κ . The κ plots follow a similar trend as those of electrical conductivity σ . The κ value increases gradually from nearly zero for all four materials in the range of temperature between 100K and 600K. Beyond these temperatures, there is almost a linear increase in the range studied. The rise of thermal conductivity with increasing temperature is mainly due to the higher charge carrier concentration. Note in passing that the nearly indistinguishable plots (Fig. 7(a,b)) suggest that RhCrP and RhCrAs should have approximately the same band gaps (1.01 and 1.06 eV, respectively). We also computed the total Seebeck coefficient S variation calculated by two-current model [36] to designate its nature as shown in Fig. 8 (a,b). As one can see, the Seebeck coefficient of both RhCrSi and RhCrGe Heusler compounds is negative for the entire temperature range and negative in both RhCrP and RhCrAs Heusler compounds. The negative sign of S explains that electrons are the dominant charge carriers and the positive sign of S explains that the holes are dominant charge carriers. Therefore, the RhCrSi and RhCrGe compounds are *n*-type materials and the RhCrP and RhCrAs compounds are *p*-type materials. The power factor (PF) was evaluated in order to determine the performance of RhCrX ($X = Si, Ge, P, As$) compounds as thermoelectric materials, where a large PF denotes that large voltages and currents are generated. The PF is shown as a function of temperature in Fig. 8(c), which clearly demonstrates that PF increases gradually with temperature, suggesting its potential stand for commercial thermoelectric applications. Finally, the calculated transport coefficients are now used to estimate the thermoelectric efficiency through the figure of merit ZT measurement. The materials are considered as good elements for thermoelectric devices if their ZT is about or greater than unity [37].

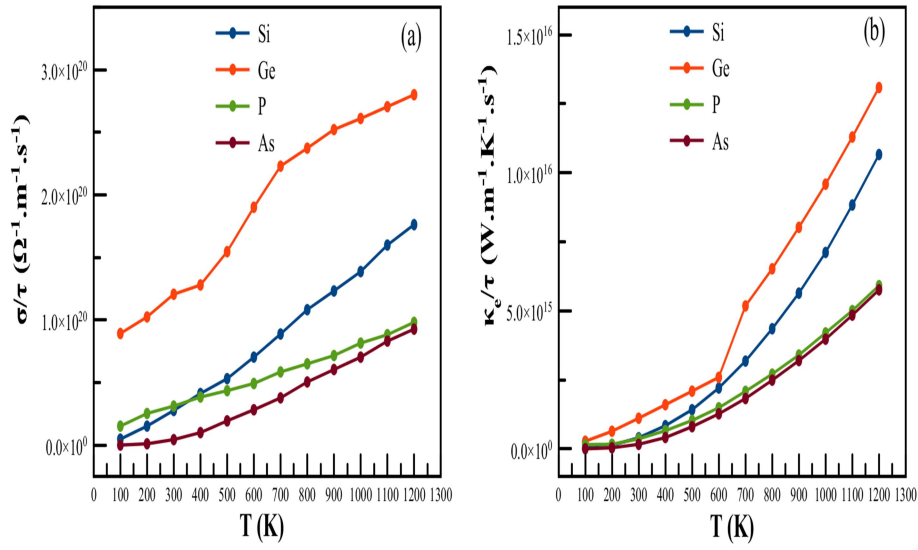


FIG. 7. Calculated transport coefficients of RhCrZ (Z= Si, Ge, P, As) (a) electrical conductivity σ/τ and (b) electronic thermal conductivity κ_e/τ (where τ is the relaxation time) as a function of temperature.

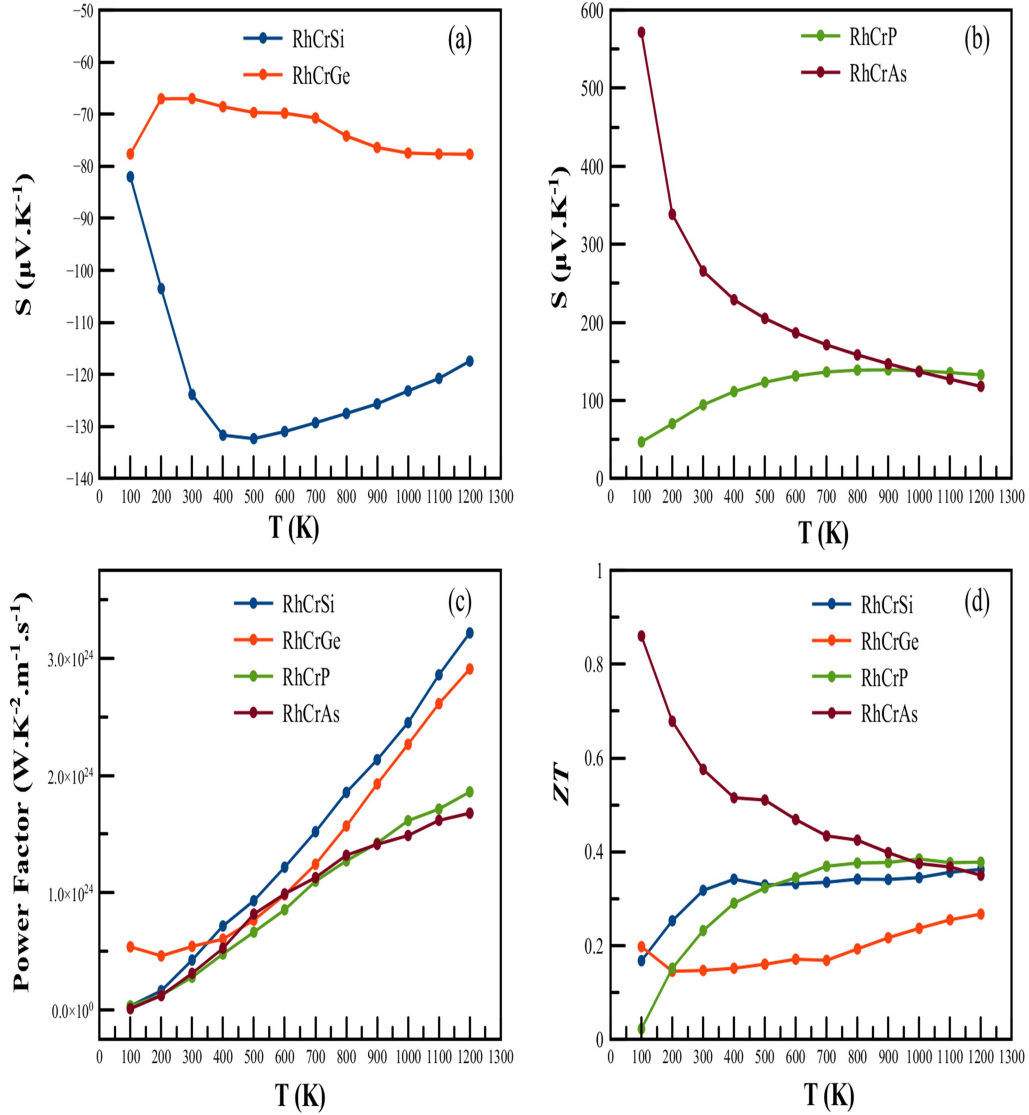


FIG. 8. Calculated transport coefficients of RhCrZ (Z= Si, Ge, P, As) (a,b) Seebeck coefficient (S), (c) power factor (PF) and (d) figure of merit (ZT), as a function of temperature.

The variation of ZT is shown in Fig. 8(d), which shows a linearly increasing trend with temperature in the three RhCrSi, RhCrGe and RhCrP compounds and a decrease in the RhCrAs compound. The highest value of 0.86 is reached for RhCrAs at 100K, where the Seebeck coefficient reaches its maximum (Fig. 8(a)). This value is the same compared to that of thermoelectric materials, such as Sb_2Te_3 ($ZT \sim 0.9$) found at $\sim 273\text{K}$ [38] and zintl compounds Ba_3AlAs_3 ($ZT = 0.74$) and Sr_3AlAs_3 ($ZT = 0.85$) found at 100K and 150K, respectively [39]. In return, the value for RhCrP at 100K is smaller due to the lower Seebeck coefficient at the same temperature. At room temperature, the computed thermoelectric efficiency of RhCrAs ($ZT = 0.568$) is nearly greater than the range of the few half-Heusler alloys studied experimentally as 0.45 [40, 41] and may trigger its stand as potential candidate for a thermoelectric material.

Although the observed ZT values are small for the three RhCrSi, RhCrGe and RhCrP compounds compared to available thermoelectric materials, the thermoelectric performance of the present materials could be improved by doping with suitable sp -elements or miniaturizing the size; i.e., shifting to nano-dimensions [42,43]. Therefore, the present materials are likely to find their application as high temperature thermoelectric materials. The values of electrical conductivity, thermal conductivity and Seebeck coefficient at room temperature are summarized in Table 5. Based on these types of results, RhCrAs can be considered to be probably the most noticeable material for thermoelectric applications. Unfortunately, a comparison of our results is not achieved due to lack of any experimental data regarding these materials. Exactness and contrast are not possible, but these calculations may act as reference data and expand the valuable information to forthcoming theoretical or experimental investigations.

Table 5. Values of electrical conductivity σ (in $10^{19} \Omega^{-1} \cdot \text{m}^{-1} \cdot \text{s}^{-1}$), thermal conductivity κ (in $10^{14} \text{W} \cdot \text{m}^{-1} \cdot \text{K}^{-1} \cdot \text{s}^{-1}$), Seebeck coefficient S (in $\mu\text{V} \cdot \text{K}^{-1}$), power factor (PF) (in $10^{23} \text{W} \cdot \text{m}^{-1} \cdot \text{K}^{-2} \cdot \text{s}^{-1}$) and figure of merit ZT at 300 K for RhCrZ ($Z = \text{Si, Ge, P, As}$) compounds.

Compound	σ	κ	S	PF	ZT
<i>RhCrSi</i>	2,770	4,016	-123,850	4,249	0,317
<i>RhCrGe</i>	12,060	11,082	-67,001	5,414	0,146
<i>RhCrP</i>	3,120	3,603	94,418	2,782	0,232
<i>RhCrAs</i>	0,441	1,623	265,738	3,115	0,575

Conclusion

In conclusion, the electronic structure, magnetic and thermoelectric properties of the half-Heusler alloys RhCrZ ($Z = \text{Si, Ge, P, As}$) have been calculated using the first-principles full-potential linearized augmented plane waves (FPLAPW+lo) method within the generalized gradient approximation (GGA). In all compounds, the stable type $\alpha + \text{FM}$ configuration structure was energetically more favorable than type β and type γ structures. Elastic properties show that all our compounds have good mechanical strength and good thermal stability with ductile nature, especially if they are used in a thermoelectric generator. At the equilibrium lattice constant, our GGA calculations have shown that RhCrZ ($Z = \text{Si, Ge, P, As}$) are half-metallic ferromagnets (HMFs) with a half-metallic gap E_{HM} of 0.37, 0.35, 0.25 and 0.02 eV for RhCrSi, RhCrGe, RhCrP and RhCrAs, respectively. The total spin magnetic

moment per formula unit in μ_B follows the rule $\mu_{\text{tot}} = Z_t - 18$. The half-metallicity is found to be robust with respect to the lattice compression and is maintained up to the lattice-constant contraction of -3.37%, -3.77%, -5.56% and -8.77% for RhCrSi, RhCrGe, RhCrP and RhCrAs, respectively. Further, the transport properties of the materials reveal some fruitful results. These materials exhibit high values of Seebeck coefficient and power factor with room temperature values. The computed figure of merit showed an extensive variety of temperatures demonstrating that HH RhCrAs exhibits a preferred thermoelectric conduct over other HH RhCrSi, RhCrGe and RhCrP materials. Since these materials offer high spin-polarization, robust half-metallicity and high Seebeck coefficient, this makes them credible applicants for spintronic and thermoelectric applications. To the best of our knowledge, most of the investigated properties are reported for the

first time and provide a reference for future experimental work.

Acknowledgments

This work has been supported by the PRFU project (N° B00L02UN220120190013) of the Ministry of Higher Education and Scientific

Research (MESRS) and the Directory General of Scientific Research and Technological Development (DGRST).

References

- [1] Casper, F., Graf, T., Chadov, S., Balke, B. and Felser, C., *Semicond. Sci. Technol.*, 27 (2012) 06300.
- [2] Akasaka, M., Iida, T., Matsumoto, A., Yamanaka, K., Takanashi, Y., Imai, T. and Hamada, N., *J. Appl. Phys.*, 104 (2008) 013703.
- [3] Downie, R.A., Barczak, S.A., Smith, R.I. and Bos, J.W.G., *J. Mater. Chem. A*, 2 (2014) 6107.
- [4] deGroot, R.A., Mueller, F.M., van Engen, P.G. and Buschow, K.H.J., *Phys. Rev. Lett.*, 20 (1983) 2024.
- [5] Lv, S., Li, H., Han, D., Wu, F., Liu, X. and Meng, J., *J. Magn. Magn. Mater.*, 323 (2011) 416.
- [6] Saeed, Y., Nazir, S., Shaukat, A. and Reshak, A.H., *J. Magn. Magn. Mater.*, 322 (2011) 3214.
- [7] Galanakis, I. and Mavropoulos, P., *Phys. Rev. B*, 67 (2003) 104417.
- [8] Kandpal, H.C., Fecher, G.H. and Felser, C.J., *J. Phys. D: Appl. Phys.*, 40 (2007) 1507.
- [9] Chen, J., Gao, G.Y., Yao, K.L. and Song, M.H., *J. of Alloys and Compounds*, 509 (2011) 10172.
- [10] Zhang, L., Cheng, Z. X., Wang, X. T., Khenata, R. and H. Rozale, *J. Supercond. Nov. Magn.*, 31 (2018) 189.
- [11] Galanakis, I., Dederichs, P. H. and Papanikolaou, N., *Phys. Rev. B*, 66 (2002) 134428.
- [12] Youn, S. J. and Min, B. I., *Phys. Rev. B*, 51 (1995) 10436.
- [13] Kervan, S. and Kervan, N., *Intermetallics*, 19 (2011) 1642.
- [14] Fang, T., Zheng, S., Zhou, T., Yana, L. and Zhang, P., *Phys. Chem. Chem. Phys.*, 19 (2017) 4411.
- [15] Bhat, T.M. and Gupta, D.C., *Journal of Physics and Chemistry of Solids*, 119 (2018) 281.
- [16] Wei, J. and Wang, G., *Journal of Alloys and Compounds*, 757 (2018) 118e123.
- [17] Qiu, P., Yang, J., Huang, X., Chen, X. and Chen, L., *Appl. Phys. Lett.*, 96 (2010) 152105.
- [18] Hohenberg, P. and Kohn, W., *Phys. Rev. B*, 136 (1964) 864.
- [19] Wimmer, E., Krakauer, H., Weinert, M. and Freeman, A.J., *Phys. Rev. B*, 24 (1981) 864.
- [20] Blaha, P., Schwarz, K., Madsen, G.K.H., Kvasnicka, D. and Luitz, J., *WIEN2k, An Augmented Plane Wave+Local Orbitals Program for Calculating Crystal Properties* (Technische Universität Wien, 2001).
- [21] Perdew, J.P., Burke, S. and Ernzerhof, M., *Phys. Rev. Lett.*, 77 (1996) 3865.
- [22] Graf, T., Felser, C. and Parkin, S.S.P., *Progress Solid State Chem.*, 39 (2011) 1.
- [23] Murnaghan, F.D., *Proc. Natl. Acad. Sci. USA*, 30 (1944) 244.
- [24] Ma, J., Hegde, V.I., Munira, K., Xie, Y., Keshavarz, S., Mildebrath, D.T., Wolverton, C., Ghosh, A.W. and Butler, W. H., *Phys. Rev. B*, 95 (2017) 024411.
- [25] Ahmad, R. and Mehmood, N., *J. Supercond. Nov. Magn.*, 31 (2017) 2637.
- [26] Mehmood, N., Ahmad, R. and Murtaza, G., *J. Supercond. Nov. Magn.*, 30 (2017) 2481.
- [27] Sinko, G.V. and Smirnov, N.A., *J. Phys. Condens. Matter*, 14 (2002) 6989.

- [28] Hill, R., Proc. Phys. Soc. Lond., 65 (1953) 909.
- [29] Pugh, S.F., Philos. Mag., 45 (1954) 823.
- [30] Fine, M.E., Brown, M.D. and Marcus, H.L., Scr. Metall, 18 (1984) 951.
- [31] Galanakis, I., Mavropoulos, P. and Dederichs, P.H., J. Phys. D. Appl. Phys., 39 (2006) 765.
- [32] Sato, K., Dederichs, P.H., Yoshida, H.K. and Kudrnovsky, J., J. Phys.: Condens. Matter, 16 (2004) S5491.
- [33] Şasioğlu, E., Sandratskii, L.M. and Bruno, P., J. Phys.: Condens. Matter, 17 (2005) 995.
- [34] Khandy, S.A. and Gupta, D.C., J. Magn. Magn. Mater., 441 (2017) 166.
- [35] Madsen, G.K.H. and Singh, D.J., Phys. Commun., 175 (2006) 67.
- [36] Xiang, H.J. and Singh, D.J., Phys. Rev. B, 76 (2007) 195111.
- [37] Takeuchi, T., Mater. Trans., 50 (2009) 2359.
- [38] G. J. Snyder and E.S. Toberer, Nature Materials, 7, 105, (2008).
- [39] Bekhti-Siad, A., Bettine, K., Rai, D. P., Al-Dourid, Y., Wang, X., Khenata, R., Bouhemadou, A. and Voon, C.H., Chinese J. Physics, 56 (2018) 870.
- [40] Hsu, C.C., Liu, Y.N. and Ma, H.K., J. of Alloys and Compounds, 597 (2014) 217.
- [41] Wang, D., Wang, G. and Li, W., J. of Alloys and Compounds, 692 (2017) 599.
- [42] Khandy, S.A. and Gupta, D.C., J. Magn. Magn. Mater., 441 (2017), 166.
- [43] Geng, H. and Zhang, H., J. Appl. Phys., 116 (2014) 033708.

Dark Matter: Could It Be Vacuum Viscosity?

M. B. Altaie^a, N. R. Suleiman^b and N. M. Ershaidat^c

^a Department of Physics, Yarmouk University, 21163 Irbid, Jordan.

^b Department of Astronomy, Eötvös University, 1117 Budapest, Hungary.

^c Physics Department, The University of Jordan, 11942 Amman, Jordan.

Received on: 21/1/2019;

Accepted on: 19/11/2019

Abstract: We test a hypothesis that stars located away from the center of the galaxy, moving under the effect of an emergent viscous drag force perpendicular to their velocities, might exhibit the behavior observed in the rotation curves of the spiral galaxies. We construct a simple model for such an assumption, then by using simple fitting technique, we are able to produce the rotation curves for a sample of 18 spiral galaxies. Results show good agreement with the observed rotation curves. The applicability of our hypothesis suggests that an emergent drag force perpendicular to the velocity of the stars might be the cause of the apparent dark matter effect.

Keywords: Rotation curves, Quantum vacuum, Dark matter.

PACS: 95.30.Sf, 95.35.+d

Introduction

The problem of the rotation curves of spiral galaxies is well-known since a long time. Classical reviews, which explain the origin of the problem since the work of Zwicky [1], are available [2]. While one would expect the stars and gases in the far parts of the galaxy to behave like being under the effect of the central field of force of the galaxy, thus following Kepler's third law, it is observed that the velocity of these parts of the galaxy is nearly constant and nearly does not change with the distance except for small variations in most cases [3], [4] and [5]. Recently, new studies have extended the range of observation to go up to 200 kpc for our galaxy [6]. Other very recent studies are giving more accurate results for the velocity profile [7] and [8] confirming the nearly constant velocity profile for the stars far from the galactic bulge. This means that the velocities of the stars and gases in this part of the galaxy are lower than what would be expected for a solid disk and are higher than what would be expected from

Kepler's third law. This might indicate that the mass of the galaxy is much more than the mass calculated from the observed matter.

The dominant explanation, which was given to this problem, was the assumption of the presence of invisible matter within the galaxies and clusters of galaxies. This excess mass was called *dark matter* and was thought to be within the galactic halo. Dark matter is thought to interact only through its gravitational effect. However, for this assumption to work, most of the dark matter has to be located in the galactic halo. If dark matter is to be clumped in the form of dense planet-sized objects, then one might assume that such objects are in stable orbits around the galaxy, but recent observations of gravitational lensing show that this is not the case [9]. According to observations from the gravitational lensing, dark matter is almost homogeneously distributed within the galactic halo. Several suggestions for other possible candidates of dark matter were presented during

the past decades, but the preferred one was the so-called weakly interacting massive particles (WIMPs) [10]. For this reason, several projects were launched in an endeavor to detect such WIMPs (for detailed presentations, see [11] and [12]). The last and the most sensitive detector of these was the project of Large Underground Xenon (LUX) detector [13]. Despite all efforts, the LUX project failed to detect any signal, which can be taken confidently to be due to WIMP [14]. The presence of dark matter got support from the analysis of cosmic microwave background radiation, where it was found that the mass density of the universe is larger than the mass density of the observed baryonic matter [15] and [16] (see also the measurements of the Planck project [17] and the results of earlier projects, e.g. [18]).

Another attempt to resolve the problem of the motion of galaxies suggested a modified Newtonian dynamics (MOND) proposal which is claimed to apply in cases of very low acceleration [19]. This is a well-studied proposal [20-23], even though it lacks rigorous theoretical foundations.

The emergent gravity proposal by Erik Verlinde suggests the presence of entropic force showing an elastic effect that causes higher gravity than expected on the basis of standard general relativity [24]. Hence, the higher velocity of the outer parts of the galaxy is not necessarily caused by the presence of larger mass, but by other effects in Verlinde's proposal. However, a recent study has shown that the calculations based on emergent gravity do not explain the rotation curves of the galaxies [25].

Studies concerning the possible interaction of quantum field with baryonic matter are available. Away from any theoretical formulation in this respect, we assume the existence of an emergent viscous force that might result from the interaction of baryonic matter of the moving stars with the virtual quantum states surrounding such stars during their motion. Such emergent force will cause a drag that will cause the stars to have ultimate constant radial velocity.

Interaction of Baryonic Matter with Vacuum

Introducing the vacuum fluctuations into the spacetime induces many effects; the most famous of them in the curved spacetime might

be the Casimir effect and the Hawking effect, where particles get created in the vicinity of the event horizon of a black hole. But, in the simplest case, one can assume that vacuum will experience some sort of polarization, which is due to the presence of the massive object, no matter whether it enjoys a horizon or not. Several phenomena where the quantum vacuum interacts with geometry and with baryonic matter and light are thoroughly explained in ref. [26]. It is expected that such a vacuum polarization will certainly induce a concentration of virtual states with density that could be proportional to the distance from the center of the object. Accordingly, a viscous drag is expected to emerge in this case. However, it remains a challenge to show the existence of such a force and show that such an emergent viscosity is inversely proportional to the distance from the center of the massive body. Incidentally, in the Casimir effect, the drag force is proportional to $1/d$, where d is the distance from the massive object.

The Model

In this article, we are going to test a proposal that may suggest a new model to explain the rotation curves of spiral galaxies. We assume that the individual stars which are located at the peripheral parts of the galaxy are experiencing a drag force acting upon them radially. Such a force might be produced by some sort of dynamically generated viscous medium and would balance the centripetal acceleration of the star, thus resulting in a terminal velocity. We will not make any attempt here to explain the origin of the assumed drag force or show how it could be generated, but will only try to test such an assumption by fitting the calculated velocity curves of some galaxies to actual observations and see whether they comply with the assumed dynamics. If the fitting results are satisfactory, then the idea might become worthwhile to be considered for further studies in a more profound theoretical context.

As the galaxy rotates, its central part will certainly behave like a disk because of the high density of celestial objects in that region. The outer parts of the galaxy are in motion like any planetary system. This motion can be approximated to be in the state of free fall, as it is taking place under the acceleration of the gravity. As such is the motion of the stars, then

once a viscous medium of any sort is assumed to exist, a radial drag force will be generated which will have the mechanical status similar to what happens when a metal ball is dropped into a vessel filled with oil. The viscous drag force will eventually balance the gravitational force and consequently the falling body will attain a terminal velocity. In this model, stars falling under the act of gravity will also attain such a terminal velocity and move with constant speed throughout their path. This proposal may solve the problem of dark matter on the cosmological scale too, since the expansion of the space between large structures in the universe would generate similar effect to that taking place by motion of individual stars of the galaxy.

We assume the presence of a drag force acting radially perpendicular to the velocity vector of the star and balancing the gravitational force acting on it. Therefore, we may equate the emergent viscous force taken here to be described by Stokes' formula with the gravitational force causing the motion of the star. Therefore, we have:

$$F_d = F_g. \quad (1)$$

This means that:

$$6\pi a \eta v = \frac{G m M}{r^2}, \quad (2)$$

where m is the mass of the star, M is the mass of the inner part of the galaxy, η is the coefficient of the emergent vacuum viscosity, a is the radius of the star, r is the distance of the star measured from the galactic center and v is its observed velocity.

Eq. (2) may be written as:

$$6\pi \left(\frac{a}{m} \right) \eta v = \frac{G M}{r^2}.$$

Assuming a circular orbit, the velocity of the star is given by:

$$v^2 = \frac{G M}{r}. \quad (3)$$

Thus, substituting Eq. (3) into Eq. (2), the velocity of the star under this mechanism of the drag force will be given by:

$$v = 6\pi \left(\frac{a}{m} \right) \eta r. \quad (4)$$

Phenomenologically, since v is nearly constant, the viscosity coefficient η should be proportional to $1/r$. Let us, for the sake of argument, assume a more generalized form of the variation of η with the distance r and set:

$$\eta = \frac{C}{B+r}, \quad (5)$$

where B and C are constants that would be determined in this model by fitting the observational data. Accordingly, the velocity of a star located at a distance r from the center of the galaxy will be given by:

$$v = 6\pi \left(\frac{a}{m} \right) \frac{C r}{B+r}. \quad (6)$$

We will try to test this formula by correlating it with actual observations from our galaxy, the Milky Way. In the next step, we will check whether this formula fits well with observational results obtained for the rotation curves of other spiral galaxies.

Calculations and Results

Primarily, we have no idea about the value of the viscosity coefficient η . Let us first evaluate this coefficient empirically using Eq. (4) and the available data about the sun's kinematics given in [26]. The aim is to know the order of magnitude of η in order to obtain an estimation for the viscosity of the medium near the sun. Consequently, we will be able to find the viscosity function along the whole galaxy. To do this, we plot the observed circular velocities v_c of the stars belonging to our galaxy *versus* their distance from the galactic center. The basic data for the sun used in our calculations is the same as that used by ref. [27], with: the mass $M = 1.9889 \times 10^{30}$ kg, the radius $a = 6.953 \times 10^8$ m, the distance from galactic center $r = 2.57 \times 10^{20}$ m, $v = 2.5 \times 10^5$ m/s. From this basic data, we can have a rough estimate of the order of magnitude of the viscosity coefficient η ; using Eq. (4) we get:

$$\eta = 1.47 \times 10^5 \text{ kg/m.s.} \quad (7)$$

Now, in order to find an estimate of the viscosity function along the whole galaxy, we plot the observed circular velocities of the stars

versus their distances. For this, we use the observational data given in [6] shown in Table 1.

TABLE 1. observational data [6].

r (kpc)	v_c (km/s)
1.61	217.83
2.57	229.58
3.59	223.11
4.51	247.88
5.53	253.14
6.50	270.95
7.56	267.80
8.34	270.52
9.45	235.58
10.50	249.72
11.44	261.96
12.51	284.30
13.53	271.54
14.59	251.43
16.05	320.70
18.64	286.46

The results for the rotation curve of our galaxy are shown in Fig. 1. This distribution of velocities can be taken as a base for a simple fitting out of which we obtain a functional description of the velocity profile. Once we obtain this functional profile, we will have an estimate for a trial function that might be used to check the adherence of the velocity profile of other galaxies to our model.

From the fitting of the rotation curve of our galaxy shown in Fig. 1, we obtain the circular velocity as a function of the radial distance from the galactic center. This is given by:

$$v_c = \frac{286.41148}{0.68598 + r}. \quad (8)$$

Then, using Eq. (6), the dependence of the viscosity coefficient on the radial distance will be given by:

$$\eta(r) = \frac{m}{6\pi a} \frac{286.41148}{0.68598 + r}. \quad (9)$$

To simplify the model, we will take the ratio a/m for the stars to be equal to that of the sun, which is 2.86×10^{21} kg/m. Accordingly, we get:

$$\eta(r) = \frac{4.346 \times 10^{25}}{2.116 \times 10^{16} + r}, \quad (10)$$

where now r is in kilometers and η is in kg/km.s.

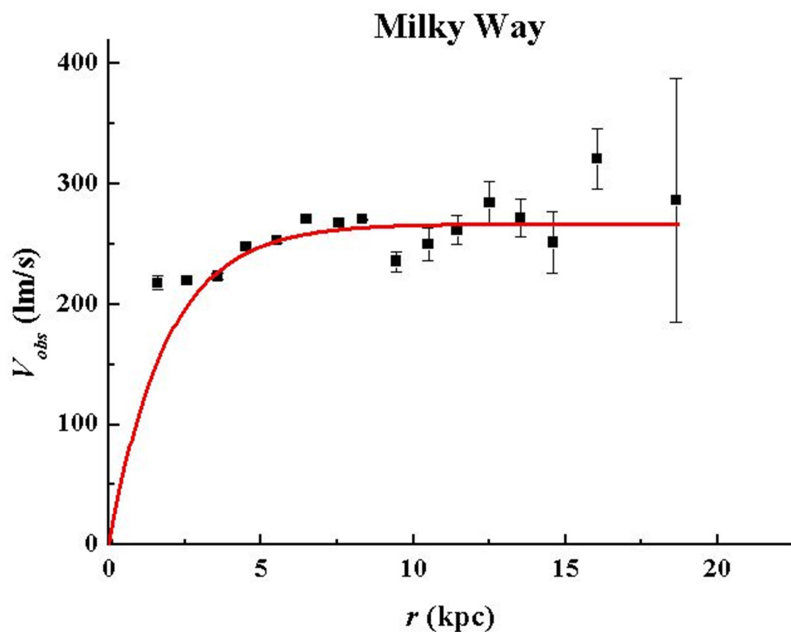


FIG. 1. Fitting of the rotation curve of Milky Way.

Fitting the Rotation Curves of Other Galaxies

Lelli et al. [8] employ the new Spitzer Photometry and Accurate Rotation Curves (SPARC) database. SPARC is a sample of 175 disk galaxies representing all rotationally supported morphological types. It includes near-infrared observations that trace the distribution of stellar mass and 21-cm observations that trace the atomic gas. The 21-cm data also provides velocity fields from which the rotation curves are derived. In some cases, these are supplemented by high spatial resolution observations of ionized interstellar gas. SPARC is the largest galaxy sample to date with spatially resolved data on the distribution of both stars and gas as well as rotation curves for every galaxy.

We have chosen data for 18 spiral galaxies from the SPARC with different distances, as shown in Table 2. These galaxies are chosen from the available set with radii near that of our galaxy. We calculate the viscosity function $\eta(r)$ and then calculate the velocity function for these galaxies. For this purpose, we find that the best fitting function can be expressed in terms of an exponential function as:

$$v(r) = b(1 - e^{-r/c}), \quad (11)$$

where b and c are constants that vary from one galaxy to another. Accordingly, the viscosity coefficient function will be given by:

$$\eta(r) = \frac{1}{6\pi} \left(\frac{m}{a} \right) \frac{b(1 - e^{-r/c})}{r}. \quad (12)$$

The constants b and c for the 18 galaxies under consideration are given in the last two columns of Table 2. It is noticeable that the constants b and c in Eq. (11) and Eq. (12) correspond to the terminal velocity at the far rim and the galactic bulge, respectively. This has been found as we compare the values given in Table 2 with the data known about the galaxies. However, this correspondence will be better explained in a model establishing the detailed vacuum fluctuation interaction effect.

We plot the calculated fitting curves against the observational data for the 18 galaxies listed

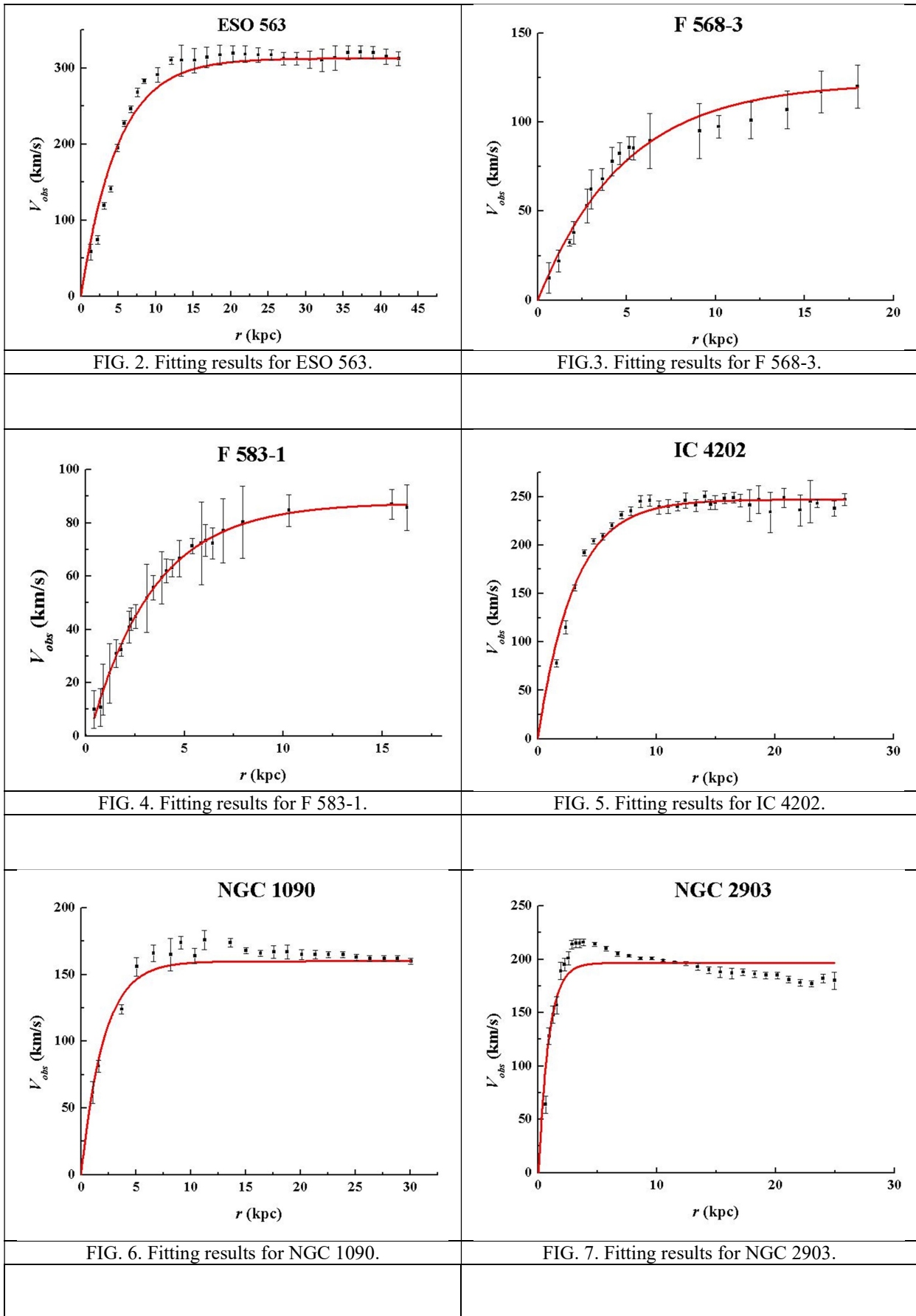
in Table 2, where the square dots stand for the observational data and the fitting is represented by the solid line. It is interesting to note that some curves show excellent fit even better than that obtained for our galaxy shown in Fig. 1. The novelty of our work is the ability to adopt the fitting of the rotation curves of so many galaxies with the identification of two parameters only, the radius of the galactic bulge and the terminal velocity of their far rims.

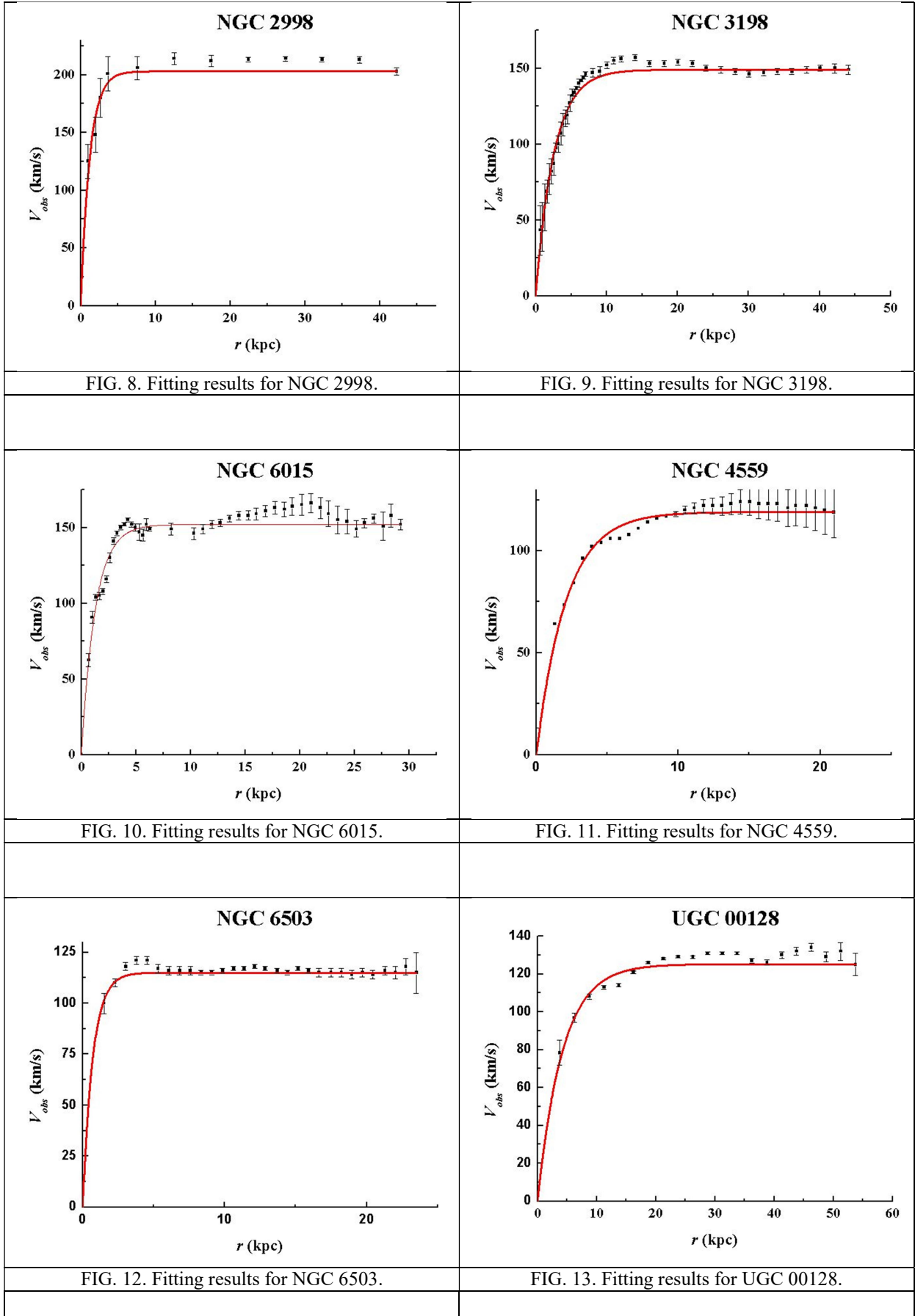
TABLE 2. data for the 18 spiral galaxies from SPARC.

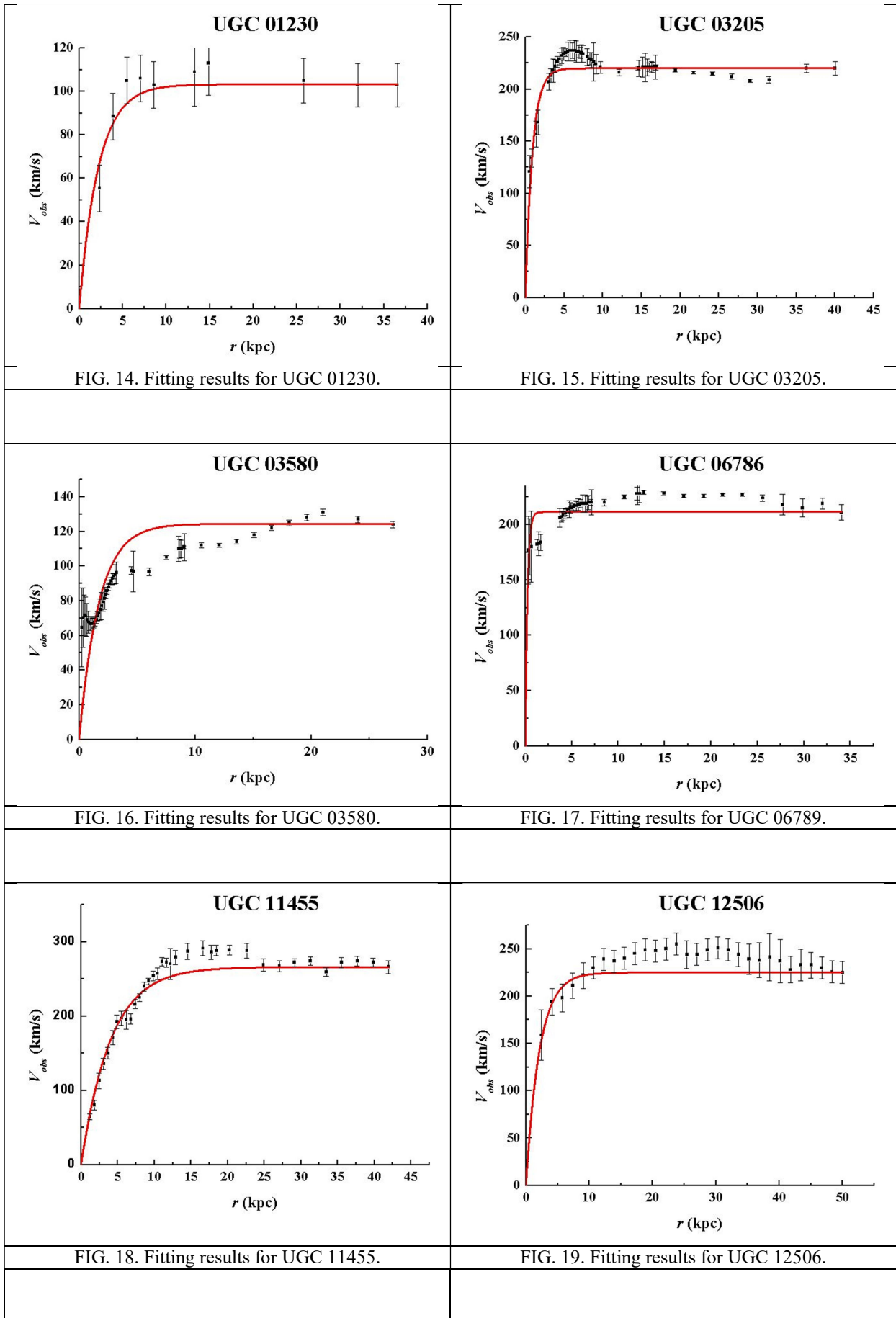
Galaxy Name	Distance (Mpc)	b (km/s)	c (kpc)
ESO 563	60.8	312.7	4.85
F-568-3	82.4	122.4	4.86
F-583-1	35.4	86.3	3.37
IC 4202	100.4	247.1	3.02
NGC 1090	37.0	160.0	2.05
NGC 2903	6.60	180.6	0.73
NGC 2998	68.1	203.0	1.20
NGC 3198	13.8	149.0	2.58
NGC 4559	9.00	119.1	2.07
NGC 6015	17.0	152.0	1.27
NGC 6503	6.26	115.0	0.70
UGC 00128	64.5	125.2	4.19
UGC 01230	53.7	103.3	2.22
UGC 03205	50.0	220.0	0.91
UGC 03580	20.7	124.4	1.69
UGC 06786	29.3	211.5	0.23
UGC 11455	78.6	266.0	4.03
UGC 12506	100.6	225.0	2.10
Milky Way	0	266.9	1.9

Figures

Below are the fitting figures that we obtained for the 18 spiral galaxies we have considered in this work.







Discussion and Conclusions

In this paper, we have tried to test the idea that the rotation curves of spiral galaxies could be resulting from the motion of their parts in a viscous medium, where a drag force perpendicular to the direction of motion is applied. No attempt in this work is made to show how such force is generated. The aim is only to test the assumption that once the stars are assumed to be moving under the effect of such a force, the rotation curves of the galaxies can be explained accordingly as a dynamic effect rather than being due to the existence of some sort of dark matter.

As for the viscosity function and since the viscosity of the medium is thought to be emerging through the interaction of baryonic matter with virtual states of the vacuum, it is quite reasonable to expect that the viscosity of the medium will not be constant all through, but will be some function of position. Accordingly, we have assumed certain position dependence that satisfies the very general boundary conditions in such a case. The fitting results we have obtained show that such an assumption is quite plausible.

Taking into consideration the approximations adopted by our model and the inevitable observational error bars shown in the figures, the results depicted in Figs. 2-19 show good agreement with observational data, at 95% confidence level. There are some discrepancies in some cases; for example, the predicted rotation curve of galaxy NGC 2903 in Fig. 7 shows poor agreement with observations, where the velocity profile is peaking at the rim of the galactic bulge. This might be due to the internal structural circumstances inside this galaxy, as it is known that the central region of this galaxy has a very high rate of star formation [28], a factor indicating the existence of a strong gravitational potential within the galactic bulge. The high slope of velocity profile within the bulge is also in support of this explanation. A similar discrepancy is noticed in Fig. 15 for UGC 3205 depicting a cusp-core-like shape in the bulge region. Such a discrepancy was also obtained in MOND rotation curve for this galaxy [29]. Here, we agree with the explanation that this may be a result of streaming motions in the weak bar in this galaxy which cause the observed velocities to deviate significantly from

the local circular velocity and lead to asymmetries in the observed HI velocity field. We also notice that our fitting of the rotation curve for UGC 03580 in Fig. 16 is poor. Our results are similar to those obtained for the MOND curve [29]. Generally, the morphology of the galaxies seems to play an important role in forming the velocity profile and such role can be accounted for within the detailed theory. It should be noted that in our simplified model proposed here, we have considered the ratio of the radius of the stars to their mass a/m to be unity. Obviously, this will be a crude approximation when it comes to consider the detailed morphology of the galaxies.

If the hypothesis proposed in this work is accepted, then an urgent need appears to develop a theory that should rigorously demonstrate how vacuum viscosity emerges out of the interaction of moving baryonic matter with the vacuum states. However, it should be noted that such a medium does not need to have its viscosity as an independent intrinsic property; rather, the proposed viscosity is an emergent dynamic property, which becomes available as masses move through the quantum vacuum. Evidently, here at this point, the theory is not yet established and some serious theoretical work is needed.

It is worth mentioning here that the drag force will cause the parts of the galaxy at the far rim to move with very low acceleration as these parts reach their terminal velocity. Here, our model meets with the MOND proposal [19], though the reasoning provided here is more profound and may have better physical explanation.

It would be worth mentioning that the emergent gravity proposal by Erik Verlinde [24] suggests the presence of an entropic force showing an elastic effect that causes higher gravity than expected on the basis of standard general relativity. This might be compared with the viscous force we are suggesting here, which causes a drag that effectively might be compared with the extra emergent gravity. However, recent investigations show that there are some reservations on the emergent gravity proposal in relation to that the radial acceleration relation does not explain rotation curves of spiral galaxies except on applying certain constraints on the mass-to-light ratio [25].

McGaugh, Lelli and Schombert [30] studied the radial acceleration traced by rotation curves and that predicted by the observed distribution of baryons in galaxies with different morphologies. They found a strong correlation clearly indicating that the dark matter contribution is fully specified by that of the baryons. Now, if we take the dark matter effect to be replaced by the emergent viscosity effect proposed in this work, we can fairly consider this finding as a supporting evidence for the case of emergent viscosity suggested here; such a viscosity is thought to be generated out of an interaction between quantum vacuum states and the baryonic matter.

If the notion of emergent viscosity is to be adopted, then the proposal of dark matter could be applied entirely on a cosmic scale too; the

motion of the galaxies in space is hampered by the emergent viscosity. This makes the universe expand slower than expected. A slower expansion might indicate that the universe contains more matter; as such, the average density of the universe will appear higher than expected and consequently a dark matter assumption may be invoked. Therefore, if the drag force due to the emergent viscosity is adopted, then there is no need for dark matter. Certainly, some detailed calculations are needed once the theory for such an emergent viscosity is established to calculate the actual value of Hubble's parameter and compare it with observations. This will be another test of the theory besides what has been suggested for the rotation curves of the galaxies.

References

- [1] Zwicky, F., *The Astrophysical Journal*, 86 (1937) 217.
- [2] Einasto, J., *Brazilian Journal of Physics*, 43 (2013) 369 and "Dark Matter and Cosmic Web Story", (World Scientific, Singapore, 2014).
- [3] Rubin, V.C. and Ford, W.K., Jr., *The Astrophysical Journal*, 159 (1970) 379.
- [4] Roberts, M.S. and Rots, A.H., *Astronomy and Astrophysics*, 26 (1973) 483.
- [5] Rubin, V.C., Burstein, D., Ford, W.K., Jr. and Thonnard, N., *The Astrophysical Journal*, 289 (1985) 81.
- [6] Bhattacharjee, P., Chaudhury S. and Kundu, S., *The Astrophysical Journal*, 785 (2014) 63.
- [7] Lelli, F., McGaugh S.S. and Schombert J.M., *The Astronomical Journal*, 152 (2016) 157.
- [8] Lelli, F. et al., *The Astrophysical Journal*, 836 (2) (2017) 152 and: http://astroweb.case.edu/SPARC/MassModels_Lelli2016c.mrt. Last access on Sep. 01, 2019.
- [9] Massey, R., Kitching T. and Richard H., *Reports on Progress in Physics*, 73 (2010) 086901.
- [10] Feng, J.L., *Annual Review of Astronomy and Astrophysics*, 48 (2010) 495.
- [11] O'Hare, C.A.J., Ph.D. Thesis, University of Nottingham, (2017), UK.
- [12] Roszkowski L., Sessolo E.M. and Trojanowski S., *Rep. Prog. Phys.*, 814 (2018) 066201.
- [13] Aprile, E., "The XENON1T dark matter search experiment", in: "Sources and Detection of Dark Matter and Dark Energy in the Universe". Cline, D. (Springer, 2013) Chapter 14, pp. 93-96.
- [14] Akerib, D.S. et al., *Phys. Rev. Lett.*, 118 (2017) 021303.
- [15] Schramm, D.N., *Nuclear Physics B-Proceedings Supplements*, 28A (1992) 243.
- [16] Luković, V., Cabella, P. and Vittorio, N., *Int. J. Mod. Phys. A*, 29 (2014) 1443001.
- [17] Ade, P.A.R. et al., *Astronomy & Astrophysics*, 594 (2016) A13.
- [18] Hinshaw, G. et al., *The Astrophysical Journal Supplement Series*, 208 (2013) 19.
- [19] Milgrom, M., *ApJ*, 270 (1983) 365.
- [20] Sanders, R.H. and McGaugh, S.S., *Annual Review of Astronomy and Astrophysics*, 40 (2002) 263-317.
- [21] Famaey, B. and McGaugh S.S., *Living Reviews in Relativity*, 15 (2012) 10.

- [22] Famaey, B. and Binney, J., Mon. Not. R. Astron. Soc., 363 (2005) 603.
- [23] Sanders, R.H., Mon. Not. R. Astron. Soc., 342 (2003) 901.
- [24] Verlinde, E., JHEP, 4 (2011) 029.
- [25] Lelli F., McGaugh S.S. and Schombert, J.M., Mon. Not. R. Astron. Soc. Lett., 468 (2017) L68.
- [26] Milonni, P.W., “The Quantum Vacuum: An Introduction to Quantum Electrodynamics”, (The Academic Press, New York, 1994).
- [27] NASA, "Solar System Exploration: Planets: Sun: Facts & Figures". Archived from the original on 2 January 2008.
- [28] Alonso-Herrero, A., Ryder, S.D. and Knapen, J.H., Mon. Not. R. Astron. Soc., 322 (2001) 757.
- [29] Sanders, R.H. and Noordermeer, E., Mon. Not. R. Astron. Soc., 379 (2007) 702.
- [30] McGaugh, S.S., Lelli, F. and Schombert, J.M., Phys. Rev. Lett. 117 (2016) 201101.

Solution of the Hamilton – Jacobi Equations in an Electromagnetic Field Using Separation of Variables Method – Staeckel Boundary Conditions

B. M. Al-Khamiseh^a, R. S. Hijjawi^b and J. M. Khalifeh^a

^a Department of Physics, The University of Jordan, 11942-Amman, Jordan.

^b Department of Physics, Mutah University, Al-Karak, Jordan.

Received on: 07/07/2019;

Accepted on: 25/11/2019

Abstract: This manuscript aims to resolve the Hamilton-Jacobi equations in an electromagnetic field by two methods. The first uses the separation of variables technique with Staeckel boundary conditions, whereas the second uses the Newtonian formalism to solve the same example. Our results demonstrate that the Hamilton-Jacobi variables can be completely detached by using separation of variables technique with Staeckel boundary conditions that correspond to other results using Newtonian formalism.

Keywords: Lagrangian mechanics, Electromagnetic field, Hamilton-Jacobi, Staeckel boundary conditions, Newtonian mechanics.

Introduction

The Hamilton's classic Jacobi theory played a huge role in the development of theoretical and mathematical physics. On the one hand, it builds a bridge between classical mechanics and other branches of physics, in particular optics. On the other hand, it generates a link between classical theory and quantum theory [1].

Separation of variables is one of the oldest techniques in mathematical physics, which still remains one of the most effective and powerful tools in the theory of integrable systems. An important method of determining the full integration of the Hamilton-Jacobi equation of the system is the way in which the variables are separated. This method can be generalized to systems with "n" degrees of freedom that allow the separation of variables. It was not known what the most comprehensive separation system was with "n" degrees of freedom. However, it is now known how an orthogonal system with "n" degrees of freedom is separated. This was discovered by Staeckel in his habilitation thesis

[2]. These systems are now called Staeckel systems. Staeckel systems theory can be found in many publications, such as references [3-22].

A standard construction of the action-angle variables from the poles of the Baker-Akhiezer function has been interpreted as a variant [23]. The fundamental elements of the separation variables theory, including the Eisenhart and Robertson theorems, Kalnins – Miller theory and the intrinsic characterization of the separation of the Hamilton – Jacobi equation, are developed in a unitary and geometrical perspective [24].

This work aims to solve the Hamilton-Jacobi equation using the method of separation variables and solve the same equation using Newtonian formalism. Our results demonstrate that the Hamilton-Jacobi variables can be completely detached by using separation of variables technique with Staeckel boundary conditions that correspond to other results using Newtonian formalism.

This paper is organized as follows: the following sections (A, B and C) present some basic definition of the Hamilton-Jacobi equation of a Staeckel system. Section two presents how to solve the Hamilton-Jacobi equation by the method of Staeckel boundary conditions. Section three presents how to solve the problem by Newtonian formalism. Finally, section four is dedicated to our conclusions.

1- Basic Definitions

In this part of the manuscript, we briefly introduce some of the fundamental definitions used in this work [25].

A- Staeckel Matrix Φ and Staeckel Vector Ψ

In a Staeckel system with n degrees of freedom, we will assume an $(n \times n)$ matrix Φ and a vector Ψ with n components Ψ_r . Actually, $n^2 + n$ components of Φ and Ψ solve completely the Staeckel system and that's why we will call it the Staeckel matrix and Staeckel vector. The elements are all functions of the coordinate q_r , but in the upcoming way:

$$\Phi_{rl} = \Phi_{rl}(q_r), \Psi_r = \Psi_r(q_r). \quad (1)$$

In short, one coordinate consists of a row r of both Φ and Ψ . We will say that the rows of Φ are with separated variables; that is, the rows of Φ are separated. It indicates that this separation property controls the whole theory of Staeckel system.

First, we will need the cofactors C_{ij} of the matrix elements Φ_{ij} of the matrix Φ , in addition to the determinant Δ and the inverse v of matrix Φ . We will set the elements of the inverse $v = \Phi^{-1}$ of the matrix Φ by $(\Phi^{-1})_{ij}$ or call them v_{ij} .

We may need some well-known properties of determinants and matrices such as:

$$\sum_j \Phi_{ij} v_{jk} = \sum_j v_{ij} \Phi_{jk} = \delta_{ik} \quad (2)$$

$$v_{ij} = \frac{C_{ij}}{\Delta} \quad (3)$$

$$\sum_i \Phi_{ji} C_{ik} = \Delta \sum_i \Phi_{ji} v_{ik} = \Delta \delta_{jk} \quad (4)$$

A direct consequence of the separation property (1) is that the cofactor C_{ij} will depend on $(n-1)$ coordinates only: C_{ij} does not contain the variable q_i . This will simplify several partial derivatives; for instance,

$$\frac{\partial \Delta}{\partial q_k} = \sum_i C_{ki} \frac{\partial \Phi_{ik}}{\partial q_k} \quad (5)$$

B- The Hamiltonian of a Staeckel System

In terms of the notations and initial developments (given in section A), we can now easily define a Staeckel system. The Staeckel system can be defined as:

$$H = \sum_{k=1}^n \left[\frac{\dot{q}_k^2}{2v_{1k}} + v_{1k} \Psi_k \right] = \sum_{k=1}^n v_{1k} \left[\frac{\dot{q}_k^2}{2v_{1k}^2} + \Psi_k \right] \quad (6)$$

where the kinetic energy is given by: $T = \sum_{k=1}^n \frac{\dot{q}_k^2}{2v_{1k}}$ and the potential energy is: $V = \sum_{k=1}^n v_{1k} \Psi_k$.

We can see that all the ingredients are the Staeckel vector Ψ and the first row of the inverse of the Staeckel matrix Φ . The second form of the Hamiltonian shown in Eq. (6) is the product of a row vector, v_{1k} , by a column vector, Ψ_k . The elements g_{kk} of the diagonal metric tensor are thus given by:

$$g_{kk} = \frac{1}{v_{1k}} = \frac{1}{(\Phi^{-1})_{1k}} = \frac{\Delta}{C_{k1}} \quad (\text{with } \sum_k \frac{\Phi_{ks}}{g_{kk}} = \delta_{1s}) \quad (7)$$

As a result of the notes of section A, we have:

$$\frac{\partial g_{kk}}{\partial q_k} = \frac{1}{C_{k1}} \frac{\partial \Delta}{\partial q_k} = \sum_i \frac{C_{ki}}{C_{k1}} \frac{\partial \Phi_{ki}}{\partial q_k}. \quad (8)$$

In the following part, we simply derive the Hamiltonian equations of motion, $\dot{P}_l = -\frac{\partial H}{\partial q^l}$ from Eq. (6), thus:

$$\frac{d}{dt} \left[\frac{\dot{q}_l}{v_{1l}} \right] = - \sum_{k=1}^n \left[\frac{\dot{q}_k^2}{2v_{1k}^2} - \Psi_k \right] \frac{\partial v_{1k}}{\partial q_l} + v_{1l} \frac{\partial \Psi_l}{\partial q_l}. \quad (9)$$

The Staeckel Hamiltonian does not depend explicitly on time; that is, we have a conservative system with the classical energy integral given as follows:

$$\sum_{k=1}^n v_{1k} \left[\frac{\dot{q}_k^2}{2v_{1k}^2} + \Psi_k \right] = \alpha_1 = \text{constant}. \quad (10)$$

It will be useful to write this first integral also in a different form. Let us take benefit of the relation in Eq. (2); adding to Eq. (10) some terms which are zeros or ones:

$$\sum_{k=1}^n v_{1k} \left[\frac{\dot{q}_k^2}{2v_{1k}^2} + \Psi_k \right] = \alpha_1 \sum_k v_{1k} \Phi_{k1} + \alpha_2 \sum_k v_{1k} \Phi_{k2} + \dots + \alpha_n \sum_k v_{1k} \Phi_{kn}, \quad (11)$$

where the α 's are all arbitrary constants. Compiling the terms differently leads to:

$$\sum_{k=1}^n v_{1k} \left[\frac{\dot{q}_k^2}{2v_{1k}^2} + \Psi_k - \sum_{r=1}^n \Phi_{kr} \alpha_r \right] = 0, \quad (12)$$

where the constants α 's are sometimes called separation constants. The interest of the above form of energy integral is actually that the two last terms in the brackets are now with separated variables. The second and third terms are function of k ; i.e., n separable equations.

The most important property of Staeckel systems exists in the following theorem:

"Not only the expression given in Eq. (12) is zero, but also each bracket separately", Pars [8]:

$$\frac{\dot{q}_k^2}{2v_{1k}^2} + \Psi_k = \sum_{r=1}^n \Phi_{kr} \alpha_r. \quad (13)$$

C- Completion of the Solution of the Staeckel System

The first integral in Eq. (12) can be written in another form as:

$$\frac{\dot{q}_k^2}{v_{1k}^2} = 2(\sum_{r=1}^n \Phi_{kr} \alpha_r - \Psi_k) = f_k(q_k). \quad (14)$$

We have also:

$$\frac{\dot{q}_k}{\sqrt{f_k(q_k)}} = v_{1k}. \quad (15)$$

Multiplying by Φ_{kr} and summing over k produce:

$$\sum_{k=1}^n \frac{\dot{q}_k \Phi_{kr}}{\sqrt{f_k(q_k)}} = \sum_{k=1}^n v_{1k} \Phi_{kr} = \delta_{1r}. \quad (16)$$

We see that each term in the sum on the left-hand side is a function of one variable q_k only:

$$\sum_{k=1}^n \int \frac{\Phi_{kr} dq_k}{\sqrt{f_k(q_k)}} = \beta_r = \text{constant } r = 2, 3, 4, \dots, n \quad (17.A)$$

$$\sum_{k=1}^n \int \frac{\Phi_{k1} dq_k}{\sqrt{f_k(q_k)}} = t - t_0 \quad r = 1. \quad (17.B)$$

This inserts n new constants of integration; altogether $2n$ constants of integration are inserted. Finally, n equations can be solved and give the n coordinates q_k as a function of time t and the constants, β_r . The velocities are then given by Eq. (13). We have to use Eqs. (17.A) and (17.B) to calculate the values of the constants of integrations with the initial conditions.

2- Separation of Variables of Hamilton-Jacobi by Using Staeckel Boundary Conditions

The separation of Hamilton-Jacobi equations is a characteristic of the dynamic system as well as the coordinates that are described. A simple

criterion cannot be given to refer to a coordinate system that results in a separate Hamilton-Jacobi equation for a particular system [26]. However, if:

- the Hamiltonian is conserved and takes the form:

$$H = \frac{1}{2}(\mathbf{P} - \mathbf{a})\mathbf{T}^{-1}(\mathbf{P} - \mathbf{a}) + V(\mathbf{q}). \quad (A)$$

Here, \mathbf{a} is a column matrix, \mathbf{T} is a square $n \times n$ matrix and \mathbf{p} is a row matrix.

- The set of generalized coordinates q_i forms an orthogonal system of coordinates, so that the matrix \mathbf{T} is diagonal. It follows that the inverse matrix \mathbf{T}^{-1} is also diagonal with non-vanishing elements:

$$(\mathbf{T}^{-1})_{ii} = \frac{1}{T_{ii}}. \quad (B)$$

- For problems and coordinates satisfying this description, the Staeckel conditions state that the Hamilton-Jacobi equation will be completely separable if the vector \mathbf{a} has elements \mathbf{a}_i that are functions only of the corresponding coordinate; that is, $\mathbf{a}_i = \mathbf{a}_i(q_i)$ and the potential function $V(\mathbf{q})$ can be written as a sum of the form:

$$V(\mathbf{q}) = \sum_i \frac{V_i(q_i)}{T_{ii}}. \quad (C)$$

- There exists an $n \times n$ matrix Φ with elements $\Phi_{ij} = \Phi_{ij}(q_i)$ such that:

$$(\Phi^{-1})_{1j} = \frac{1}{T_{jj}}. \quad (D)$$

Consider the motion of a particle of mass m and charge e that moves in uniform crossed electric and magnetic fields, \mathbf{E} is in the x -direction and \mathbf{B} is in the z -direction. The Hamilton-Jacobi is given as:

$$H = \frac{1}{2m} \left[p_x^2 + \left(p_y - \frac{eB}{c} x \right)^2 + p_z^2 \right] - eEx. \quad (18)$$

Comparing Eq. (18) with the equation: $H = \frac{1}{2}(\mathbf{P} - \mathbf{a})\mathbf{T}^{-1}(\mathbf{P} - \mathbf{a}) + V(\mathbf{q})$, we get:

$$\mathbf{T}^{-1} = \begin{pmatrix} \frac{1}{m} & 0 & 0 \\ 0 & \frac{1}{m} & 0 \\ 0 & 0 & \frac{1}{m} \end{pmatrix}. \quad (19)$$

Applying Staeckel boundary conditions, we satisfy:

$$(T^{-1})_{ii} = \frac{1}{T_{ii}} = \begin{pmatrix} \frac{1}{m} & 0 & 0 \\ 0 & \frac{1}{m} & 0 \\ 0 & 0 & \frac{1}{m} \end{pmatrix}. \quad (20)$$

In addition to the following two conditions:

$$(\Phi^{-1})_{1j} = \frac{1}{T_{jj}} = \begin{pmatrix} \frac{1}{m} & \frac{1}{m} & \frac{1}{m} \\ 0 & \frac{1}{m} & 0 \\ 0 & \frac{1}{m} & \frac{1}{m} \end{pmatrix}. \quad (21)$$

And we get:

$$V(q) = \frac{V_i(q_i)}{T_{ii}} = \left(\frac{\psi_1(x)}{m} \right). \quad (22)$$

If the Staeckel conditions are satisfied, then Hamilton's characteristic function is completely separable:

$$W(q) = \sum_i W_i(q_i). \quad (23)$$

Inserting H from Eq. (18) into equation $H\left(q, \frac{\partial W}{\partial q}\right) + \frac{\partial S_0}{\partial t} = 0$ and using the definition of momentum $p = \frac{\partial W}{\partial q}$, we obtain:

$$\frac{1}{2m} \left[\left[\frac{\partial W_x}{\partial x} \right]^2 + \left[\frac{\partial W_y}{\partial y} - \frac{eB}{c} x \right]^2 + \left[\frac{\partial W_z}{\partial z} \right]^2 \right] - eEx = \alpha. \quad (24)$$

Here, z is a cyclic coordinate and y is a cyclic coordinate; we get:

$$\left[\frac{\partial W_y}{\partial y} \right]^2 = \alpha_{y'}^2, \quad (25)$$

$$\left[\frac{\partial W_z}{\partial z} \right]^2 = \alpha_{z'}^2. \quad (26)$$

Integrating Eq. (25) and Eq. (26), we find:

$$W_{y'} = \int_0^{y'} \alpha_{y'} dy = \alpha_{y'} y' \quad (27)$$

$$W_{z'} = \int_0^{z'} \alpha_{z'} dz = \alpha_{z'} z'. \quad (28)$$

Substituting Eqs. (27) and (28) in Eq. (24), we get:

$$\frac{1}{2m} \left[\left[\frac{\partial W_x}{\partial x} \right]^2 + \left[\alpha_{y'} - \frac{eB}{c} x \right]^2 + \alpha_{z'}^2 \right] - eEx = \alpha. \quad (29)$$

Rewriting Eq. (29), we obtain:

$$\left[\frac{\partial W_x}{\partial x} \right]^2 = 2m\alpha + 2meEx - \left(\alpha_{y'} - \frac{eBx}{c} \right)^2 - \alpha_{z'}^2. \quad (30)$$

Integrating Eq. (30), we get:

$$W_x = \int \sqrt{\left(2m\alpha + 2meEx - \left(\alpha_{y'} - \frac{eBx}{c} \right)^2 - \alpha_{z'}^2 \right)} dx. \quad (31)$$

The Hamilton's characteristic function becomes:

$$W = W_{x'} + W_{y'} + W_{z'}$$

$$W = \int_0^{x'} \sqrt{\left(2m\alpha + 2meEx - \left(\alpha_{y'} - \frac{eBx}{c} \right)^2 - \alpha_{z'}^2 \right)} dx + \alpha_{y'} y' + \alpha_{z'} z'. \quad (32)$$

Substituting Eq. (32) in equation $S(q, \alpha, t) = W(q, \alpha) - \alpha t$, we obtain:

$$S(q, \alpha, t) = \int_0^{x'} \sqrt{\left(2m\alpha + 2meEx - \left(\alpha_{y'} - \frac{eBx}{c} \right)^2 - \alpha_{z'}^2 \right)} dx + \alpha_{y'} y' + \alpha_{z'} z' - \alpha t. \quad (33)$$

Differentiating Eq. (33) with respect to α_i , we obtain:

$$\beta_{x'} + t = \int_0^{x'} \frac{m}{\sqrt{2m\alpha + 2meEx - \left(\alpha_{y'} - \frac{eBx}{c} \right)^2 - \alpha_{z'}^2}} dx \quad (34)$$

$$y' - \beta_{y'} = \int_0^{x'} \frac{\left(\alpha_{y'} - \frac{eBx}{c} \right)}{\sqrt{\left(2m\alpha + 2meEx - \left(\alpha_{y'} - \frac{eBx}{c} \right)^2 - \alpha_{z'}^2 \right)}} dx \quad (35)$$

$$z' - \beta_{z'} = \int_0^{x'} \frac{\alpha_{z'}}{\sqrt{\left(2m\alpha + 2meEx - \left(\alpha_{y'} - \frac{eBx}{c} \right)^2 - \alpha_{z'}^2 \right)}} dx. \quad (36)$$

Substituting $\omega = \frac{eB}{mc}$, $(m\omega a)^2 = 2m\alpha + 2meEx - \frac{2eE}{\omega} \alpha_{y'} + \left(\frac{eE}{\omega} \right)^2 - \alpha_{z'}^2$, and replacing $2m\alpha + 2meEx - \left(\alpha_{y'} - m\omega x \right)^2 - \alpha_{z'}^2 = (m\omega a)^2 - (m\omega)^2 \left(x - \frac{1}{m\omega} \left(\alpha_{y'} + \frac{eE}{\omega} \right) \right)^2$, Eq. (35) becomes:

$$y' - \beta_{y'} = \int_0^{x'} \frac{-\left(x - \frac{\alpha_{y'}}{m\omega} \right)}{\sqrt{\left(a^2 - \left(x - \frac{1}{m\omega} \left(\alpha_{y'} + \frac{eE}{\omega} \right) \right)^2 \right)}} dx. \quad (37)$$

Let $x = \frac{1}{m\omega} \left(\alpha_{y'} + \frac{eE}{\omega} \right) - a \cos \Omega$, where Ω is a function of t ; substituting in Eq. (37) after integration, Eq. (37) becomes:

$$y' - \beta_{y'} = \frac{-eE}{m\omega^2} \Omega + a \sin \Omega. \quad (38)$$

Multiplying Eq. (34) by ω , substituting $\omega = \frac{eB}{mc}$, $(m\omega a)^2 = 2m\alpha + 2meEx - \frac{2eE}{\omega} \alpha_{y'} + \left(\frac{eE}{\omega} \right)^2 - \alpha_{z'}^2$, and replacing $2m\alpha + 2meEx -$

$$(\alpha_{y'} - m\omega x)^2 - \alpha_{z'}^2 = (m\omega a)^2 - (m\omega)^2 \left(x - \frac{1}{m\omega} \left(\alpha_{y'} + \frac{eE}{\omega} \right) \right)^2 \quad \text{R.H.S., Eq. (34)}$$

becomes:

$$\omega(\beta_{x'} + t) = \int_0^{x'} \frac{dx}{\sqrt{\left(a^2 - \left(x - \frac{1}{m\omega} \left(\alpha_{y'} + \frac{eE}{\omega} \right) \right)^2 \right)}}. \quad (39)$$

Let $x = \frac{1}{m\omega} \left(\alpha_{y'} + \frac{eE}{\omega} \right) - a \cos \Omega$; substituting in Eq. (39) after integration, Eq. (39) becomes:

$$\omega(\beta_{x'} + t) = \Omega. \quad (40)$$

Multiplying Eq. (36) by m , the equation becomes:

$$z' - \beta_{z'} = \frac{\alpha_{z'}}{m} \int_0^{x'} \frac{m}{\sqrt{\left(2m\alpha + 2meEx \left(\alpha_{y'} - \frac{eBx}{c} \right)^2 - \alpha_{z'}^2 \right)}} dx \quad (41)$$

In Eq. (41), similar to Eq. (34), we can replace $\int_0^{x'} \frac{m}{\sqrt{\left(2m\alpha + 2meEx \left(\alpha_{y'} - \frac{eBx}{c} \right)^2 - \alpha_{z'}^2 \right)}} dx = (\beta_{x'} + t)$. Eq. (41) becomes:

$$z' - \beta_{z'} = \frac{\alpha_{z'}}{m} (\beta_{x'} + t). \quad (42)$$

Rewriting Eqs. (40), (38) and (42) and substituting the value of Ω , the equations become:

$$x'(t) = \frac{1}{m\omega} \left(\alpha_{y'} + \frac{eE}{\omega} \right) - a \cos \omega(\beta_{x'} + t) \quad (43)$$

$$y'(t) = \beta_{y'} - \frac{eE}{m\omega} (\beta_{x'} + t) + a \sin \omega(\beta_{x'} + t) \quad (44)$$

$$z'(t) = \beta_{z'} + \frac{\alpha_{z'}}{m} (\beta_{x'} + t). \quad (45)$$

The above equations, (43) and (44), express x and y in terms of the parameter $\Omega = \omega(\beta_{x'} + t)$, giving the projection of the trajectory onto the xy -plane. We recognize the curve as a cycloid. The particle moves along the trajectory in the z -direction at constant velocity $\frac{\alpha_{z'}}{m}$.

3- Solving the Problem within Newtonian Formalism

Consider the motion of a particle of mass m and charge e moving in uniform crossed electric and magnetic fields, where \mathbf{E} is in the x -direction and \mathbf{B} is in the z -direction.

Initially, the particle is at rest; thus, the magnetic force is zero, while the electric field accelerates the charge in the x -direction. In the absence of force in the z -direction, the position of this particle at any time t can be described by the vector $(x(t), y(t), z(t))$. Therefore, the velocity is calculated as follows:

$$\mathbf{v} = (\dot{x}, \dot{y}, \dot{z}). \quad (46)$$

Hence, applying Newton's second law dots indicates time derivatives. Thus,

$$\mathbf{v} \times \mathbf{B} = \begin{vmatrix} \hat{x} & \hat{y} & \hat{z} \\ \dot{x} & \dot{y} & \dot{z} \\ 0 & 0 & B \end{vmatrix} = B\dot{y}\hat{x} - B\dot{x}\hat{y}. \quad (47)$$

And therefore, applying Newton's second law,

$$\mathbf{F} = e(\mathbf{E} + \mathbf{v} \times \mathbf{B}) = m\mathbf{a}. \quad (48)$$

Substituting Eq. (47) and $\mathbf{a} = \ddot{x}\hat{x} + \ddot{y}\hat{y} + \ddot{z}\hat{z}$ in Eq. (48), we get:

$$e(E\hat{x} + B\dot{y}\hat{x} - B\dot{x}\hat{y}) = m(\ddot{x}\hat{x} + \ddot{y}\hat{y} + \ddot{z}\hat{z}). \quad (49)$$

Or, treating the \hat{x} , \hat{y} and \hat{z} components separately,

$$m\ddot{x} = e(E + B\dot{y}) \quad (50)$$

$$m\ddot{y} = -eB\dot{x} \quad (51)$$

$$m\ddot{z} = 0. \quad (52)$$

For the sake of convenience, let:

$$\omega = \frac{eB}{m}. \quad (53)$$

(This is referred to as the **cyclotron frequency**; at this frequency, the particle would revolve in the absence of any electric field). Thereafter, the equations of motion take the forms:

$$\ddot{x} = \omega \left(\frac{E}{B} + \dot{y} \right) \quad (54)$$

$$\ddot{y} = -\omega \dot{x} \quad (55)$$

$$m\ddot{z} = 0. \quad (56)$$

Derivation of Eqs. (54) and (55) and substitution of Eqs. (54) and (55) in Eqs. (54) and (55) after derivation, we get:

$$\ddot{y} = -\omega \ddot{x} = -\omega^2 \left(\frac{E}{B} + \dot{y} \right) \quad (57)$$

$$\ddot{x} = \omega \ddot{y} = -\omega^2 \dot{x}. \quad (58)$$

Substituting $\dot{y}(t) = q(t)$ in Eq. (57), we get:

$$\ddot{q} + \omega^2 q = \frac{-\omega^2 E}{B}. \quad (59)$$

The general solution of the second-order nonhomogeneous linear Eq. (59) can be expressed as follows:

$$q = q_c + Q, \quad (60)$$

where Q denotes any specific function that satisfies the nonhomogeneous equation and q_c is the complementary solution; $q_c = c_1 q_1 + c_2 q_2$ refers to a general solution of the corresponding homogeneous equation $\ddot{q} + \omega^2 q = 0$. (In other words, q_1 and q_2 are a pair of fundamental solutions of the corresponding homogeneous equation; c_1 and c_2 are arbitrary constants).

The complementary solution in Eq. (59) is:

$$q_c = B \cos \omega t - A \sin \omega t. \quad (61)$$

Let $Q = f$ for some unknown coefficient f ; thereafter, substitute them back into the original differential Eq. (59).

$$\text{Hence, } = -\frac{E}{B}.$$

$$\text{Therefore, } q = q_c + Q = B \cos \omega t - A \sin \omega t - \frac{E}{B}.$$

The solution of Eq. (57) is:

$$\dot{y}(t) = q(t) = B \cos \omega t - A \sin \omega t - \frac{E}{B}. \quad (62)$$

Integrating Eq. (62), we get:

$$y(t) = c_1 \sin \omega t + c_2 \cos \omega t - \frac{E}{B} t + c_3. \quad (63)$$

Let $\dot{x} = q$ and substitute in Eq. (58); thereafter, we get:

$$\ddot{q} + \omega^2 q = 0. \quad (64)$$

The general solution in Eq. (64) is:

$$q(t) = A \cos \omega t + B \sin \omega t. \quad (65)$$

The general solution in Eq. (58) is:

$$\dot{x} = q = A \cos \omega t + B \sin \omega t. \quad (66)$$

Upon integrating Eq. (66), we obtain:

$$x(t) = c_2 \sin \omega t - c_1 \cos \omega t + c_4. \quad (67)$$

The solution in Eq. (56) is:

$$z(t) = c_5 t + c_6. \quad (68)$$

However, the particle started from the origin ($x(0) = y(0) = z(0) = 0$) and ($\dot{x}(0) = 0, \dot{y}(0) = \frac{\alpha_y}{m}, \dot{z}(0) = \frac{\alpha_z}{m}$), where α_y, α_z are constants; these six conditions determine the constants c_1, c_2, c_3, c_4, c_5 and c_6 :

$$c_1 = c_4 = \frac{1}{\omega} \left(\frac{\alpha_y}{m} + \frac{E}{B} \right)$$

$$c_2 = c_3 = c_6 = 0$$

$$c_5 = \frac{\alpha_z}{m}.$$

After applying six boundary conditions, the equations of motion are:

$$x(t) = \frac{1}{\omega} \left(\frac{\alpha_y}{m} + \frac{E}{B} \right) (1 - \cos \omega t) \quad (69)$$

$$y(t) = \frac{1}{\omega} \left(\frac{\alpha_y}{m} + \frac{E}{B} \right) \sin \omega t - \frac{E}{B} t \quad (70)$$

$$z(t) = \frac{\alpha_z}{m} t. \quad (71)$$

Let $R = \frac{1}{\omega} \left(\frac{\alpha_y}{m} + \frac{E}{B} \right)$ and then rewrite Eq. (69) and Eq. (70) in such a way to exploit

$(\cos \omega t)^2 + (\sin \omega t)^2 = 1$. Here is what you get:

$$(x - R)^2 + \left(y + \frac{E}{B} t \right)^2 = R^2. \quad (72)$$

This is the equation of a circle of radius R in the xy plane; it gives the projection of the trajectory onto the xy -plane. Here again, the trajectory is a cycloid. The particle moves along the trajectory in the z -direction at constant velocity $\frac{\alpha_z}{m}$.

In the second and third sections of the manuscript, we found the equations of motion (Hamilton – Jacobi equations) in an electromagnetic field in two ways; Staeckel boundary conditions and Newton's laws, where when substituting $\omega = \frac{eB}{m}$, $\beta_{x'} = \beta_{y'} = \beta_{z'} = 0$ and $a = \frac{1}{m\omega} \left(\alpha_y + \frac{eE}{\omega} \right)$, Equations (43), (44) and (45) will be the same Equations as (69), (70) and (71).

4- Conclusion

We considered the appropriate Hamilton-Jacobi equation in the electromagnetic field example and separated the variables using Staeckel boundary conditions. This method applies to some Hamiltonians in which certain conditions are satisfied, such as: conservative Hamiltonian and orthogonal coordinates. When applying this method on the Hamilton – Jacobi in the electromagnetic field, we found Hamilton's characteristic function and Hamilton's principal function, then we separated completely the variables of the Hamilton – Jacobi equation in the electromagnetic field and solved the same

example using Newtonian formalism to find equations of motion. Our results are in agreement with those of Newtonian formalism [27].

There are two very important reasons for working with Lagrange equations instead of Newton's equations:

- (i) the Lagrange equations adhere to any coordinate system, while Newton is confined to an inertial frame.
- (ii) the second reason is the ease with which we can deal with constraints in the Lagrange system.

References

- [1] Rudolph, G. and Schmidt, M., "Differential Geometry and Mathematical Physics", Theoretical and Mathematical Physics, (Springer Science and Business Media, Dordrecht, 2013),
- [2] Staeckel, P., "Über die Integration der Hamilton-Jacobischen Differentialgleichung mittels Separation der Variablen". (Habilitationsschrift, Halle, 1891).
- [3] Stackel, P., Math. Ann., (35) (1890) 91.
- [4] Staeckel, P., Journal für reine und angewandte Mathematik, 111 (1893) 290.
- [5] Charlier, C.V.L., "Die Mechanik des Himmels: Vorlesungen", 1, (Leipzig, Veit, 1902).
- [6] Eisenhart, L.P., Annals of Mathematics, 35 (2) (1934) 284.
- [7] Pars, L.A., The American Mathematical Monthly, 56 (6) (1949) 394.
- [8] Pars, L.A.A., "Treatise on Analytical Dynamics", (John Wiley and Sons, New York, 1965) pp. 320-326.
- [9] Ibort, A., Magri, F. and Marmo, G., Journal of Geometry and Physics, 33 (3-4) (2000) 210.
- [10] Daskaloyannis, C. and Tanoudis, Y., Physics of Atomic Nuclei, 71 (5) (2008) 853.
- [11] Błaszak, M. and Marciniak, K., Journal of Mathematical Physics, 47 (3) (2006) 032904.
- [12] Ballesteros, Á., Enciso, A., Herranz, F.J., Ragnisco, O. and Riglioni, D., Symmetry, Integrability and Geometry: Methods and Applications, 7 (2011) 048.
- [13] Famaey, B. and Dejonghe, H., Monthly Notices of the Royal Astronomical Society, 340 (3) (2003) 752.
- [14] Garfinkel, B., Lectures in Applied Mathematics, Space Mathematics, Part One, 5 (1966) 40.
- [15] Rauch-Wojciechowski, S. and Waksjö, C., arXiv preprint online, (2003) 0309048.
- [16] Kalnins, E.G., Kress, J.M. and Miller Jr, W., Journal of Mathematical Physics, 47 (4) (2006) 043514.
- [17] Marikhin, V.G., Journal of Physics A: Mathematical and Theoretical, 47 (17) (2014) 175201.
- [18] Marikhin, V.G. and Sokolov, V.V., Russian Mathematical Surveys, 60 (5) (2005) 981.
- [19] Minesaki, Y. and Nakamura, Y., Journal of Physics A: Mathematical and General, 39 (30) (2006) 9453.
- [20] Prus, R. and Sym, A., Physics Letters A, 336 (6) (2005) 459.
- [21] Sergyeyev, A. and Błaszak, M., Journal of Physics A: Mathematical and Theoretical, 41 (10) (2008) 105205.
- [22] Tsiganov, A.V., arXiv preprint arXiv, (2018) 1809.05824.
- [23] Sklyanin, E.K., Progr. Theor. Phys. Suppl., 118 (1995) 35.
- [24] Benenti, S., Chanu, C. and Rastelli, G., Journal of Mathematical Physics, 43 (11) (2002) 5183.
- [25] Broucke, R., Celestial Mechanics, 25 (2) (1981) 185.
- [26] Goldstein, H., "Classical Mechanics", 2nd Edition, (Addison-Wesley, Reading, 31, 1980).
- [27] Griffiths, D.J., "Introduction to Electrodynamics", 3rd Edition, (Prentice Hall, Reed College. 2005).

Reformulation of Degasperis-Procesi Field by Functional Derivatives

Y. M. Alawaideh^a, R. S. Hijjawi^b and J. M. Khalifeh^a

^a Department of Physics, The University of Jordan, Amman 11942, Jordan.

^b Department of Physics, Mutah University, Karak, Jordan.

Received on: 07/07/2019;

Accepted on: 25/11/2019

Abstract: We reformulated the Degasperis-Procesi equation using functional derivatives. More specifically, we used a semi-inverse method to derive the Lagrangian of the Degasperis-Procesi equation. After introducing the Hamiltonian formulation using functional derivatives, we applied this new formulation to the Degasperis-Procesi Equation. In addition, we found that both Euler-Lagrange equation and Hamiltonian equation yield the same result. Finally, we studied an example to elucidate the results.

Keywords: Functional derivatives, Hamiltonian systems, Degasperis-Procesi equation, Euler-Lagrange.

Introduction

The Degasperis-Procesi equation was discovered by Degasperis and Procesi [1] in a search for integrable equations similar in form to that of Camassa-Holm equation. Notably, this equation is widely used in the field of fluid dynamics, as well as in biology, aerodynamics, continuum mechanics, image processing, physics, control theory, oceanology and geometry. Additionally, Degasperis-Procesi equation has been used to describe a wide range of physical phenomena as a model for the evolution as well as interaction of nonlinear waves [1]. It was first derived as an evolution equation that governs one-dimensional, small amplitude, long surface gravity waves propagating in a shallow channel of water [2, 3]. Fuchssteiner and Fokas [4], Lenells [5] and Camassa and Holm [6] proposed the derivation of solution forward as a model for dispersive shallow water waves, subsequently discovering that it is a formally integrable dimensional Hamiltonian system.

It is well known that the use of the Euler-Lagrange equation in setting up equations of

motion for certain physical systems is more convenient and useful as compared to that of Newtonian mechanics. The important benefit imparted is that when Lagrangian and momenta for a certain system are known, the Hamiltonian function can be written. Once the Hamiltonian is known, the system then becomes amenable to the techniques of quantum mechanics which cannot be implemented using Newtonian mechanics. However, although the formalism developed by Newton is applicable for both conservative and non-conservative systems, it is not possible to use traditional Lagrangian and Hamiltonian mechanics with non-conservative systems. Several methods have been proposed and implemented to introduce dissipative effects, such as friction, into classical Hamiltonian and Lagrangian mechanics. One such method is the Rayleigh dissipation function, which can be used when the frictional forces are found to be proportional to the velocity [7, 8]. However, another scalar function is needed in addition to the Lagrangian in this method to specify the equations of motion. This function cannot appear in the Hamiltonian function, which is why it is of

no use when attempting to quantize friction. Another method [9, 10] introduces an auxiliary coordinate system in the Lagrangian that describes a reverse-time system with negative friction. Notably, this method leads to the desired equations of motion, but the Hamiltonian yields extraneous solutions that must be rejected, whereas the physical meaning of the momenta remains unclear. Against this backdrop, a good and realistic method is to include the microscopic details of the dissipation directly in the Lagrangian or the Hamiltonian [11]. This method constitutes a valuable tool in the study of quantum dissipation, but it is not intended to be a general method for introducing the friction force into Lagrangian mechanics. Thus, we see that none of the above techniques exhibit the same directness and simplicity that are found in the mechanics of conservative systems. El-Wakil et al. recently studied the interaction between the structure and propagation of the resulting solitary waves obtained from TFKdV using fractional order derivatives [12]. The authors obtained fractional Euler-Lagrange equations resulting from the Lagrangian densities and then solved the derived time-fractional KdV equation using the variational-iteration method.

In another study, Riewe [13, 14] formulated a version of the Euler-Lagrange equation for problems in calculus of variation with fractional derivatives. Furthermore, a new development of systems with higher-order fractional derivatives was discussed in [15, 16]. Over the past decades, additional studies relating to the fractional Euler-Lagrange equations can be found in Muslih and Baleanu [17] and Dreisigmeyer and Young [18]. They were also able to obtain the fractional variational principle and the differential equations of motion for a fractional mechanical system.

This present paper is a generalization of the aforementioned work on Hamilton's equation for Degasperis-Procesi field using functional derivatives. It is organized as follows: In Sec.1, the form of Euler-Lagrangian equation is presented in terms of functional derivative of the Lagrangian. In Sec.2, the Euler-Lagrange Equation in terms of Momentum Density is succinctly discussed. This is followed by Sec. 3, which deals with equations of motion in terms of Hamiltonian density in functional derivative form. Sec. 4 encompasses the semi-inverse method, whereas in Sec. 5, we study one

example of classical fields that leads to Degasperis-Procesi equation in functional derivatives form. The work ends with some concluding remarks (Sec. 6).

1. Euler-Lagrange Equation in Terms of Functional Derivatives of the Lagrangian

The Lagrangian of the classical field that contains partial derivatives is a function of the form:

$$\mathcal{L} = \mathcal{L}(\psi, \psi_t, \psi_x, \psi_{xx}, \psi_{xxt}, \psi_{xxx}, t). \quad (1)$$

The Lagrangian L can be written as:

$$L = \int \mathcal{L}(\psi, \psi_t, \psi_x, \psi_{xx}, \psi_{xxt}, \psi_{xxx}, t) d^3r. \quad (2)$$

Using the variational principle, the following can be written:

$$\delta \int L dt = \delta \iint \mathcal{L} d^3r dt = \int (\delta \mathcal{L}) d^3r dt. \quad (3)$$

Using Eq. (3), the variation of \mathcal{L} is:

$$\begin{aligned} \delta \mathcal{L} = & \frac{\partial \mathcal{L}}{\partial \psi} \delta \psi + \frac{\partial \mathcal{L}}{\partial \psi_t} \delta \psi_t + \frac{\partial \mathcal{L}}{\partial \psi_x} \delta \psi_x + \\ & \frac{\partial \mathcal{L}}{\partial \psi_{xx}} \delta \psi_{xx} + \frac{\partial \mathcal{L}}{\partial \psi_{xxt}} \delta \psi_{xxt} + \frac{\partial \mathcal{L}}{\partial \psi_{xxx}} \delta \psi_{xxx} = \\ & 0. \end{aligned} \quad (4)$$

Substituting Eq. (4) into Eq. (3) yields:

$$\iint \left[\frac{\partial \mathcal{L}}{\partial \psi} \delta \psi + \frac{\partial \mathcal{L}}{\partial \psi_t} \delta \psi_t + \frac{\partial \mathcal{L}}{\partial \psi_x} \delta \psi_x + \frac{\partial \mathcal{L}}{\partial \psi_{xx}} \delta \psi_{xx} + \frac{\partial \mathcal{L}}{\partial \psi_{xxt}} \delta \psi_{xxt} + \frac{\partial \mathcal{L}}{\partial \psi_{xxx}} \delta \psi_{xxx} \right] d^3r dt = 0 \quad (5)$$

and using the following commutation relation,

$$\left. \begin{aligned} \delta \psi_t &= \delta \frac{\partial \psi}{\partial t} = \frac{\partial}{\partial t} \delta \psi \\ \delta \psi_x &= \delta \frac{\partial \psi}{\partial x} = \frac{\partial}{\partial x} \delta \psi \\ \delta \psi_{xx} &= \delta \frac{\partial^2 \psi}{\partial x^2} = \frac{\partial^2}{\partial x^2} \delta \psi \\ \delta \psi_{xxt} &= \delta \frac{\partial^3 \psi}{\partial x^2 \partial t} = \frac{\partial^3}{\partial x^2 \partial t} \delta \psi \\ \delta \psi_{xxx} &= \delta \frac{\partial^3 \psi}{\partial x^3} = \frac{\partial^3}{\partial x^3} \delta \psi \end{aligned} \right\} \quad (6)$$

We obtain the following equation:

$$\iint \left[\underbrace{\frac{\partial \mathcal{L}}{\partial \psi} \delta \psi}_{\text{first}} + \underbrace{\frac{\partial \mathcal{L}}{\partial \psi_t} \frac{\partial}{\partial t} \delta \psi}_{\text{second}} + \underbrace{\frac{\partial \mathcal{L}}{\partial \psi_{xx}} \frac{\partial^2}{\partial x^2} \delta \psi}_{\text{third}} + \underbrace{\frac{\partial \mathcal{L}}{\partial \psi_{xxt}} \frac{\partial^3}{\partial x^2 \partial t} \delta \psi}_{\text{fourth}} + \underbrace{\frac{\partial \mathcal{L}}{\partial \psi_{xxx}} \frac{\partial^3}{\partial x^3} \delta \psi}_{\text{fifth}} \right] d^3 r dt = 0 . \quad (7)$$

Integrating by parts the indicated terms in Eq. (7) with respect to space and time yields the following expression:

$$\iint \left[\frac{\partial \mathcal{L}}{\partial \psi} \delta \psi - \frac{\partial}{\partial t} \left(\frac{\partial \mathcal{L}}{\partial \psi_t} \right) \delta \psi - \frac{\partial}{\partial x} \left(\frac{\partial \mathcal{L}}{\partial \psi_x} \right) \delta \psi + \frac{\partial^2}{\partial x^2} \left(\frac{\partial \mathcal{L}}{\partial \psi_{xx}} \right) \delta \psi - \frac{\partial^3}{\partial x^2 \partial t} \left(\frac{\partial \mathcal{L}}{\partial \psi_{xxt}} \right) \delta \psi - \frac{\partial^3}{\partial x^3} \left(\frac{\partial \mathcal{L}}{\partial \psi_{xxx}} \right) \delta \psi \right] d^3 r dt = 0 . \quad (8)$$

This, in turn, results in the Euler-Lagrange equations of motion:

$$\frac{\partial \mathcal{L}}{\partial \psi} - \frac{\partial}{\partial t} \left(\frac{\partial \mathcal{L}}{\partial \psi_t} \right) - \frac{\partial}{\partial x} \left(\frac{\partial \mathcal{L}}{\partial \psi_x} \right) + \frac{\partial^2}{\partial x^2} \left(\frac{\partial \mathcal{L}}{\partial \psi_{xx}} \right) - \frac{\partial^3}{\partial x^2 \partial t} \left(\frac{\partial \mathcal{L}}{\partial \psi_{xxt}} \right) - \frac{\partial^3}{\partial x^3} \left(\frac{\partial \mathcal{L}}{\partial \psi_{xxx}} \right) = 0 . \quad (9)$$

Using Eq. (7) and integrating by parts the indicated terms with respect to space only results in:

$$0 = \int dt \int \left[\frac{\partial \mathcal{L}}{\partial \psi} \delta \psi - \frac{\partial}{\partial x} \left(\frac{\partial \mathcal{L}}{\partial \psi_x} \right) \delta \psi + \frac{\partial^2}{\partial x^2} \left(\frac{\partial \mathcal{L}}{\partial \psi_{xx}} \right) \delta \psi - \frac{\partial^3}{\partial x^2 \partial t} \left(\frac{\partial \mathcal{L}}{\partial \psi_{xxt}} \right) \delta \psi - \frac{\partial^3}{\partial x^3} \left(\frac{\partial \mathcal{L}}{\partial \psi_{xxx}} \right) \delta \psi \right] d\tau \delta \psi + \int dt \int \left[\left(\frac{\partial \mathcal{L}}{\partial \psi_t} \right) \delta \frac{\partial}{\partial t} \psi \right] d\tau . \quad (10)$$

Now, Eq. (10) can also be integrated with respect to space before converting it into summation, resulting in:

$$\sum_i \left[\frac{\partial \mathcal{L}}{\partial \psi} - \frac{\partial}{\partial x} \left(\frac{\partial \mathcal{L}}{\partial \psi_x} \right) + \frac{\partial^2}{\partial x^2} \left(\frac{\partial \mathcal{L}}{\partial \psi_{xx}} \right) - \frac{\partial^3}{\partial x^2 \partial t} \left(\frac{\partial \mathcal{L}}{\partial \psi_{xxt}} \right) - \frac{\partial^3}{\partial x^3} \left(\frac{\partial \mathcal{L}}{\partial \psi_{xxx}} \right) \right] \delta \psi_i \delta \tau_i + \sum_i \left[\frac{\partial \mathcal{L}}{\partial \psi_t} \right] \delta (\psi_t)_i \delta \tau_i = 0 . \quad (11)$$

Eq. (11) can be expressed in terms of Lagrangian density as follows:

$$\sum_i [\delta \mathcal{L}]_i \delta \tau_i = 0 , \quad (12)$$

where the left-hand side in Eqs. (11 and 12) represents the variation of L (i.e. δL) which is now produced by independent variations in $\delta \psi_i, \delta (\psi_t)_i$. Suppose now that all $\delta \psi_i, \delta (\psi_t)_i$

are zeros except for a particular $\delta \psi_j$. It is natural to define the functional derivative of the Lagrangian (∂L) with respect to $\delta \psi_i, \delta (\psi_t)_i$ for a point in the j^{th} cell to the ratio of δL to $\delta \psi_j$ [20].

$$\frac{\partial L}{\partial \psi_t} = \lim_{\delta \tau_j \rightarrow 0} \frac{\delta L}{\delta \psi_t \delta \tau_j} . \quad (13)$$

Using Eq. (12) and noting that the left-hand side represents δL yields:

$$\frac{\partial L}{\partial \psi} = \frac{\partial \mathcal{L}}{\partial \psi} - \frac{\partial}{\partial x} \left(\frac{\partial \mathcal{L}}{\partial \psi_x} \right) + \frac{\partial^2}{\partial x^2} \left(\frac{\partial \mathcal{L}}{\partial \psi_{xx}} \right) - \frac{\partial^3}{\partial x^2 \partial t} \left(\frac{\partial \mathcal{L}}{\partial \psi_{xxt}} \right) - \frac{\partial^3}{\partial x^3} \left(\frac{\partial \mathcal{L}}{\partial \psi_{xxx}} \right) \quad (14)$$

$$\frac{\partial L}{\partial \psi_t} = \lim_{\delta \tau_j \rightarrow 0} \frac{\delta L}{\delta \psi_t \delta \tau_j} = \frac{\partial \mathcal{L}}{\partial \psi_t} . \quad (15)$$

Now, using Eq. (14) and Eq. (15), we can rewrite Eq. (9), Euler-Lagrange equation, in terms of the Lagrangian L in terms of functional derivatives in the form:

$$\frac{\partial L}{\partial \psi} - \frac{\partial}{\partial t} \left(\frac{\partial L}{\partial \psi_t} \right) = 0 . \quad (16)$$

And we can write the variation of Lagrangian in terms of functional derivatives and variations of $\psi, \dot{\psi}$ as:

$$\delta L = \int \left[\frac{\partial L}{\partial \psi} \delta \psi + \frac{\partial L}{\partial \dot{\psi}} \delta \dot{\psi} \right] d^3 r . \quad (17)$$

2. Euler-Lagrange Equation in Terms of Momentum Density

The form of momentum can be written as [19]:

$$P_j^a = \frac{\delta L}{\delta \dot{\psi}_j} . \quad (18)$$

Using Eq. (13) and Eq. (14), we get:

$$P_j^a = \frac{\partial L}{\partial \dot{\psi}} \delta \tau_j = \frac{\partial \mathcal{L}}{\partial \dot{\psi}} \delta \tau_j \quad (19)$$

From Eq. (19), the momentum density π can be defined as:

$$\pi = \frac{\partial L}{\partial \dot{\psi}} = \frac{\partial \mathcal{L}}{\partial \dot{\psi}} . \quad (20)$$

Now, substituting Eq. (20) into Eq. (16), we get:

$$\dot{\pi} = \frac{\partial L}{\partial \psi} . \quad (21)$$

The above equation represents the form of Euler- Lagrange equation in terms of momentum density and the functional derivative of Lagrangian.

3. Equations of Motion in Terms of Hamiltonian Density in Functional Derivative Form

The Hamiltonian density is defined as:

$$h = \pi \dot{\psi} - \mathcal{L}(\psi_x, \psi_{xx}, \psi_t, \psi_{xt}, \psi_{xx}) . \quad (22)$$

Hamiltonian H can also be written in terms of the Hamiltonian density h as follows:

$$H = \sum_i h_i \delta \tau_i . \quad (23)$$

Substituting Eq. (22) into Eq. (23), the following is obtained:

$$H = \sum_i (\pi \dot{\psi}) \delta \tau_i - \sum_i \mathcal{L}_i \delta \tau_i . \quad (24)$$

Eq. (24) can be presented in continuous form as follows:

$$\mathcal{H} = \int [\pi \dot{\psi}] d^3r - \int \mathcal{L} d^3r \quad (25)$$

As explained in **Appendix A**, taking the variation of H and using Eq. (17) and Eq. (21), we get:

$$\delta \mathcal{H} = \int [-\dot{\pi} \delta \psi + \dot{\psi} \delta \pi] d^3r . \quad (26)$$

By analogy with the variation in L ; i.e., Eq. (17), the variation of Hamiltonian produced by variations of independent variables in terms of functional derivative can be expressed as follows (Case 1 and 2).

Case 1: All variables are independent ψ, π

$$\delta H = \int \left[\frac{\partial H}{\partial \psi} \delta \psi + \frac{\partial H}{\partial \pi} \delta \pi \right] d^3r . \quad (27)$$

Comparing Eq. (27) with Eq. (26), we get the separate equations of motion in terms of Hamiltonian:

$$\left. \begin{aligned} \frac{\partial H}{\partial \psi} &= -\dot{\pi} \\ \frac{\partial H}{\partial \pi} &= \dot{\psi} \end{aligned} \right\} \quad (28)$$

By analogy with Eq. (14) for functional derivative of Lagrangian in terms of derivative of Lagrangian density, we can simply define the functional derivative of H in terms of a Hamiltonian-density derivative with respect to the general variable field ϕ as [20]:

$$\frac{\partial H}{\partial \phi} = \frac{\partial h}{\partial \phi} - \frac{\partial}{\partial x} \left(\frac{\partial h}{\partial \phi_x} \right) + \frac{\partial^2}{\partial x^2} \left(\frac{\partial h}{\partial \phi_{xx}} \right) - \frac{\partial^3}{\partial x^2 \partial t} \left(\frac{\partial h}{\partial \phi_{xxt}} \right) - \frac{\partial^3}{\partial x^3} \left(\frac{\partial h}{\partial \phi_{xxx}} \right) . \quad (29)$$

Using the definition given in Eq. (29), we can rewrite the equations of motion given in Eq. (28) in terms of Hamiltonian density such that:

$$\frac{\partial h}{\partial \psi} - \frac{\partial}{\partial x} \left(\frac{\partial h}{\partial \psi_x} \right) + \frac{\partial^2}{\partial x^2} \left(\frac{\partial h}{\partial \psi_{xx}} \right) - \frac{\partial^3}{\partial x^2 \partial t} \left(\frac{\partial h}{\partial \psi_{xxt}} \right) - \frac{\partial^3}{\partial x^3} \left(\frac{\partial h}{\partial \psi_{xxx}} \right) = -\dot{\pi} \quad (30)$$

$$\frac{\partial h}{\partial \psi} - \frac{\partial}{\partial x} \left(\frac{\partial h}{\partial \pi_x} \right) + \frac{\partial^2}{\partial x^2} \left(\frac{\partial h}{\partial \pi_{xx}} \right) - \frac{\partial^3}{\partial x^2 \partial t} \left(\frac{\partial h}{\partial \pi_{xxt}} \right) - \frac{\partial^3}{\partial x^3} \left(\frac{\partial h}{\partial \pi_{xxx}} \right) = \dot{\psi} \quad (31)$$

Case 2: π depends on ψ

So that we take the variation just only for independent variable ψ , we have:

$$\delta H = \int \left[\frac{\partial H}{\partial \psi} \delta \psi \right] d^3r . \quad (32)$$

To state the equations of motion from Eq. (27), let us define $\pi = g(\psi)$, so that we can write the variation as:

$$\delta \pi = \frac{\partial g}{\partial \psi} \delta \psi . \quad (33)$$

Now, substituting Eq. (33) into Eq. (27) and comparing with Eq. (32), we obtain the general equations of the Hamiltonian density for this case:

$$\frac{\partial H}{\partial \psi} = \frac{\partial h}{\partial \psi} - \frac{\partial}{\partial x} \left(\frac{\partial h}{\partial \psi_x} \right) + \frac{\partial^2}{\partial x^2} \left(\frac{\partial h}{\partial \psi_{xx}} \right) - \frac{\partial^3}{\partial x^2 \partial t} \left(\frac{\partial h}{\partial \psi_{xxt}} \right) - \frac{\partial^3}{\partial x^3} \left(\frac{\partial h}{\partial \psi_{xxx}} \right) = -\dot{\pi} + \frac{\partial g}{\partial \psi} \dot{\psi} . \quad (34)$$

Eq. (34) represents the Hamilton's Equation in a form of functional derivatives, by replacing $\phi \rightarrow \psi$ in Eq. (29).

4- Semi-Inverse Method

Degasperis – Procesi Equation

The Degasperis-Procesi equation in (1+1) dimensions is given as [1]:

$$\begin{aligned} \phi_t(x, t) - \phi_{xxt}(x, t) + 4\phi^2(x, t)\phi_x(x, t) - \\ 3\phi_x(x, t)\phi_{xx}(x, t) - \phi_x(x, t)\phi_{xx}(x, t) = 0, \end{aligned} \quad (35)$$

where $\phi(x, t)$ is a field variable, $x \in R$ is a space coordinate in the propagation direction of the field and $t \in T$ ($[= [0, T_0]]$) is the time. Using a potential function $\phi(x, t)$, where $\phi(x, t) = \psi_x(x, t)$ provides the potential equation of the Degasperis-Procesi equation (35) in the form:

$$\begin{aligned} \psi_{xt}(x, t) - \psi_{xxxt}(x, t) + \\ 4\psi_x^2(x, t)\psi_{xx}(x, t) + \\ 3\psi_{xx}(x, t)\psi_{xxx}(x, t) + \\ \frac{3}{2}\psi_x(x, t)\psi_{xxxx}(x, t) = 0. \end{aligned} \quad (36)$$

The Lagrangian of this Degasperis-Procesi equation (35) can be defined using the semi-inverse method [20, 21] as follows. The functional of the potential equation (36) can be represented as the Lagrangian density in the following form:

$$\begin{aligned} j(\psi) = \int_R dx \int_T \psi(x, t) (A_1 \psi_{xt}(x, t) - \\ A_2 \psi_{xxxt}(x, t) + 4A_3 \psi_x^2 \psi_{xx}(x, t) - \\ 3A_4 \psi_{xx} \psi_{xxx}(x, t) - \\ A_5 \psi_x(x, t) \psi_{xxxx}(x, t)) dt, \end{aligned} \quad (37)$$

where A_1, A_2, A_3, A_4 and A_5 are constants to be determined later. Integrating (37) by parts and taking $\psi_t|_{\partial R} = \psi_x|_{\partial R} = \psi_x|_{\partial T} = \psi_{xx}|_{\partial R} = \psi_{xxt}|_{\partial R} = 0$ lead to:

$$\begin{aligned} j(\psi) = \\ \int_R dx \int_T \left(-A_1 \psi_t(x, t) + \right. \\ A_2 \psi_x(x, t) \psi_{xxt}(x, t) - \frac{4}{3} A_3 \psi_x^4(x, t) + \\ \frac{3}{2} (A_4 - A_5) \psi_x(x, t) \psi_{xx}^2(x, t) + \\ \left. \frac{1}{2} A_5 \psi_x^2(x, t) \psi_{xxx}(x, t) \right) dt. \end{aligned} \quad (38)$$

The constants A_i ($i = 1, 2, \dots, 6$) can be determined by taking the variation of the functional (38) to make it optimal. Applying the variation of this functional and integrating each term by parts using the variation optimum condition yield the following expression:

$$\begin{aligned} -2A_1 \psi_{xt}(x, t) - 2A_2 \psi_{xxxt}(x, t) + \\ 16A_3 \psi_x^2(x, t) \psi_{xx}(x, t) + \left(-\frac{15}{2} A_4 + \right. \\ \left. \frac{13}{2} A_5 \right) \psi_{xx}(x, t) \psi_{xxx}(x, t) (A_5 - \\ 3A_4) \psi_x(x, t) \psi_{xxxx}(x, t) = 0. \end{aligned} \quad (39)$$

Notice that the above equation (39) is equivalent to (36), so the constants A_i ($i = 1, 2, \dots, 5$) are obtained:

$$A_1 = A_2 = \frac{1}{2}, A_3 = \frac{1}{4}, A_4 = \frac{7}{24}, A_5 = -\frac{1}{8},$$

In addition, the functional expression given by (38) obtains directly the Lagrangian form of the Degasperis-Procesi equation:

$$\begin{aligned} L(\psi_x, \psi_{xx}, \psi_t, \psi_{xxt}, \psi_{xxx}) = -\frac{1}{2} \psi_x \psi_t + \\ \frac{1}{2} \psi_x \psi_{xxt} - \frac{1}{3} \psi_x^4 + \frac{5}{8} \psi_x \psi_{xx}^2 - \frac{1}{16} \psi_x^2 \psi_{xxx}. \end{aligned} \quad (40)$$

5. Illustrative Example

The Lagrangian density is:

$$\begin{aligned} L(\psi_x, \psi_{xx}, \psi_t, \psi_{xxt}, \psi_{xxx}) \\ = -\frac{1}{2} \psi_x \psi_t + \frac{1}{2} \psi_x \psi_{xxt} - \frac{1}{3} \psi_x^4 + \frac{5}{8} \psi_x \psi_{xx}^2 - \\ \frac{1}{16} \psi_x^2 \psi_{xxx}. \end{aligned} \quad (41)$$

Applying Euler-Lagrange equation (Eq. (9)), we get:

$$\begin{aligned} \psi_{xt}(x, t) - \psi_{xxxt}(x, t) + \\ 4\psi_x^2(x, t)\psi_{xx}(x, t) + \\ 3\psi_{xx}(x, t)\psi_{xxx}(x, t) + \\ \frac{3}{2}\psi_x(x, t)\psi_{xxxx}(x, t) = 0. \end{aligned} \quad (42)$$

First, we determine π using Eq (20):

$$\pi = \frac{\partial \mathcal{L}}{\partial \psi_t} = -\frac{1}{2} \psi_x. \quad (43)$$

Then, using Eq. (22), the Hamiltonian density can be written as

$$\begin{aligned} h = -\frac{1}{2} \psi_x \psi_{xxt} + \frac{1}{3} \psi_x^4 - \frac{5}{8} \psi_x \psi_{xx}^2 + \\ \frac{1}{16} \psi_x^2 \psi_{xxx}. \end{aligned} \quad (44)$$

Now, because π is ψ -dependent, we have to use equations of motion for case 2. Applying Eq. (34), we get:

$$\begin{aligned} \psi_{xt}(x, t) - \psi_{xxxt}(x, t) + 4\psi_x^2(x, t)\psi_{xx}(x, t) \\ + 3\psi_{xx}(x, t)\psi_{xxx}(x, t) + \\ \frac{3}{2}\psi_x(x, t)\psi_{xxxx}(x, t) = 0. \end{aligned} \quad (45)$$

The above equation is equivalent in form to Eq. (42) that has been derived by Euler-Lagrange.

If we do not consider the dependency of π on ψ and apply Eq. (30) in case 1, then we get:

$$\begin{aligned} &\psi_{xt}(x, t) - \psi_{xxx}(x, t) + \\ &4\psi_x^2(x, t)\psi_{xx}(x, t) + \\ &3\psi_{xx}(x, t)\psi_{xxx}(x, t) + \\ &\frac{3}{2}\psi_x(x, t)\psi_{xxxx}(x, t) = 0. \end{aligned} \quad (46)$$

This is not equivalent to Degasperis-Procesi equation given by Eq. (42).

6. Conclusion

The Hamiltonian formulation of the Degasperis-Procesi field systems is developed and the Hamilton equations are presented. Additionally, we derived the Euler-Lagrange equations. The Hamilton's equations of motion are obtained for Degasperis-Procesi density.

Two cases are considered here: (i) dependent conjugate momenta and (ii) independent conjugate momenta. It is noteworthy that the results are consistent with those derived using the formulation of Euler-Lagrange equations.

Appendix A

Variation of the Hamiltonian

We can rewrite Eq. (36) as:

$$\mathcal{H} = \int [\pi \dot{\psi}] d^3r - L. \quad (A.1)$$

Now, taking the variation of H, we get:

$$\delta \mathcal{H} = \int \delta [\pi \dot{\psi}] d^3r - \delta L. \quad (A.2)$$

Using Eqs. (27) and (28), we rewrite the variation of Lagrangian given by Eq. (A.2) as:

$$\delta L = \int [\dot{\pi} \delta \psi + \pi \delta \dot{\psi}] d^3r. \quad (A.3)$$

The above equation can be rearranged as:

$$\delta L = \int [\dot{\pi} \delta \psi + \delta [\pi \dot{\psi}] - \dot{\psi} \delta \pi] d^3r. \quad (A.4)$$

Substituting Eq. (A4) into Eq. (A2), one gets:

$$\delta \mathcal{H} = \int [-\dot{\pi} \delta \psi + \dot{\psi} \delta \pi] d^3r. \quad (A.5)$$

References

- [1] Degasperis, A. and Procesi, M., Symmetry and Perturbation Theory, 1 (1) (1999) 23.
- [2] Johnson, R.S., Journal of Nonlinear Mathematical Physics, 10 (sup.1) (2003) 72.
- [3] Dullin, H.R., Gottwald, G.A. and Holm, D.D., Physica D: Nonlinear Phenomena, 190 (1-2) (2004) 1.
- [4] Fuchssteiner, B. and Fokas, A.S., Physica D: Nonlinear Phenomena, 4 (1) (1981) 47.
- [5] Lenells, J., Journal of Physics A: Mathematical and General, 38 (4) (2005) 869.
- [6] Camassa, R. and Holm, D.D., Physical Review Letters, 71 (11) (1993) 1661.
- [7] Meirovitch, L., Elements of vibration analysis, (McGraw-Hill Science, Engineering and Mathematics, 1975).
- [8] Hietarinta, J., Physics Reports, 147 (2) (1987) 87.
- [9] Celeghini, E., Rasetti, M., Tarlini, M. and Vitiello, G., Modern Physics Letters B, 3 (16) (1989) 1213.
- [10] Kac, M., Bulletin of the American Mathematical Society, 62 (1) (1956) 52.
- [11] Yu, L.H. and Sun, C.P., Physical Review A, 49 (1) (1994) 592.
- [12] El-Wakil, S.A., Abulwafa, E.M., Zahran, M.A. and Mahmoud, A.A., Nonlinear Dynamics, 65 (1-2) (2011) 55.
- [13] Riewe, F., Physical Review E, 53 (2) (1996) 1890.
- [14] Riewe, F., Physical Review E, 55 (3) (1997) 3581.
- [15] Diab, A.A., Hijjawi, R.S., Asad, J.H. and Khalifeh, J.M., Meccanica, 48 (2) (2013) 323.
- [16] El-Zalan, H.A., Muslih, S.I., Rabei, E.M. and Baleanu, D., International Journal of Theoretical Physics, 47 (9) (2008) 2195.
- [17] Muslih, S.I. and Baleanu, D., Journal of Vibration and Control, 13 (9-10) (2007) 1209.
- [18] Dreisigmeyer, D.W. and Young, P.M., Journal of Physics A: Mathematical and General, 36 (30) (2003) 8297.
- [19] Morse, P. and Feshbach, H., "Methods of Theoretical Physics", (McGraw-Hill, New York, 1953).
- [20] Jihuan, H., Applied Mathematics and Mechanics, 21 (7) (2000) 797.
- [21] He, J.H., Chaos, Solitons and Fractals, 19 (4) (2004) 847.

Assessment of Natural Radionuclides in Local and Imported Cements in Erbil Governorate, Kurdistan Region- Iraq

Ali H. Ahmed, Adeeb O. Jafir and Hallo M. Abdullah

Department of Physics, College of Science, Salahaddin University-Hawler, Kurdistan Region, Iraq.

Received on: 30/07/2019;

Accepted on: 16/12/2019

Abstract: A total of 10 cement samples were collected from the manufactures and markets. Spectrometry analysis of Sodium Iodide NaI (TI) detector was used for measuring the samples' specific activity. The obtained specific activities of (^{226}Ra , ^{232}Th and ^{40}K) were (35, 30 and 400) Bq/kg, respectively, which are below the critical values suggested by UNSCEAR2000. The radiological hazard indices of radium equivalent activities (Ra_{eq}), the indoor absorbed dose $D_{\text{in}}(\text{nGyh}^{-1})$, the internal annual effective dose equivalent (E_{in}) and the internal index (H_{in}) were calculated. All of the obtained values were below the world wide recommendation values. Fortunately, from the analyzed results, it was concluded that the local and imported cements in Erbil governorate will make no risk when used in building constructions.

Keywords: Radionuclides, Gamma-ray spectrometer, Cement.

Introduction

Radioactivity can be regarded as a process by which an unstable atomic nucleus loses energy by emitting radiation, such as an alpha particle, beta particle and gamma ray [1].

All living organisms are continuously exposed to natural background radiation mainly coming from external background radiation, due to ^{238}U , ^{232}Th and ^{40}K , which are present in the earth's crust [2].

Building raw materials and products are derived from rock and soil that contain various amounts of natural radionuclides. They are considered as the source of direct radiation, since people spend more than 80% of their time indoors [3].

The radioactive contamination in building raw materials was specified and recognized as the major source of gamma indoor exposure [4].

Cement has been used widely throughout the world as a basic material in building constructions. Many local and international studies have been conducted to investigate and

assess the natural radioactivity due to cement [5-10].

Erbil, the capital of Kurdistan region-Iraq, lives a huge investment period in the infrastructure building and dwelling constructions; so, beside the local products, different imported raw materials including cements were inserted into markets. Thus, it is very important to study the activity concentration of primordial radionuclides (^{238}U , ^{232}Th and ^{40}K) in cement types existing in Erbil governorate, and to calculate the derived radiological parameters.

Materials and Methods

A total of 10 samples from the available cement types in Erbil markets were taken, see Table 1. From each cement type, 1.1 kg had been taken and left in a sealed Marinelli beaker for one month to reach secular equilibrium, where the rate of decay of the daughters becomes equal to that of the parents. This step is necessary to ensure that radon gas is confined within the volume and the decay products will also remain in the sample.

TABLE 1. Cement types used in the study.

Sample code	Name	Color	Origin
S1	DELTA	white	Kurdistan-Sulaymanyah
S2	ILAM	green	Iran
S3	White Portland cement	white	Iran
S4	ÇİMSA WHITE	white	Iran
S5	Baomix 101	green	Turkey
S6	Ademix 333	brown-red	Turkey
S7	Kurdistan Cement	green	Kurdistan-Erbil
S8	Kalekim 1054	white	Turkey
S9	SIBRE	brown-green	Turkey
S10	YaTIS	white	Turkey

Gamma Ray Spectrometry Analysis

The gamma spectrometer that exists in the post-graduate nuclear laboratory at Salahaddin University-Erbil consists of a 3"×3" NaI (Tl) detector (SILENA type model 3S3), a preamplifier, an amplifier, a multi-channel analyzer of 512 channels of (CASSY type and model 524058) and a high voltage power supply (521681 LYBOLD) with the range and operating voltage of 0-1500 (800 Volts). The detector resolution was measured by full width at half maximum (FWHM) of 7.4 at the 662 KeV gamma line of ^{137}Cs . The detector is shielded by two layers starting with copper (20mm) and lead (10 cm) in order to reduce background radiation. The energy calibration for NaI (Tl) gamma ray spectrometry was carried out using the point source of ^{226}Ra with its progenies: ^{214}Pb (242, 295 and 352 KeV) and ^{214}Bi (609 and 1120 KeV). Full energy peak efficiency calibration was performed using the three standard well-known activity sources of ^{137}Cs , ^{60}Co and ^{152}Eu . A CASSY software program was used to acquire and analyze the spectrum. The cement samples were counted within the calibrated spectrometer

for 21600 sec. The obtained net cement spectra (after subtracting the background) have been analyzed using indirect methods to determine the specific activities of ^{238}U and ^{232}Th . The sample concentrations of (^{238}U , ^{232}Th and ^{40}K) for the cements were determined in Bq/kg from gamma ray photo peaks of 352 KeV (^{214}Pb), 911 KeV (^{228}Ac) and 1460 (^{40}K). The activity concentration in cement samples was calculated using the following equation [5].

$$A_s = \frac{Ns}{\varepsilon_{\gamma} I_{\gamma} t m_c} (Bq Kg^{-1}), \quad (1)$$

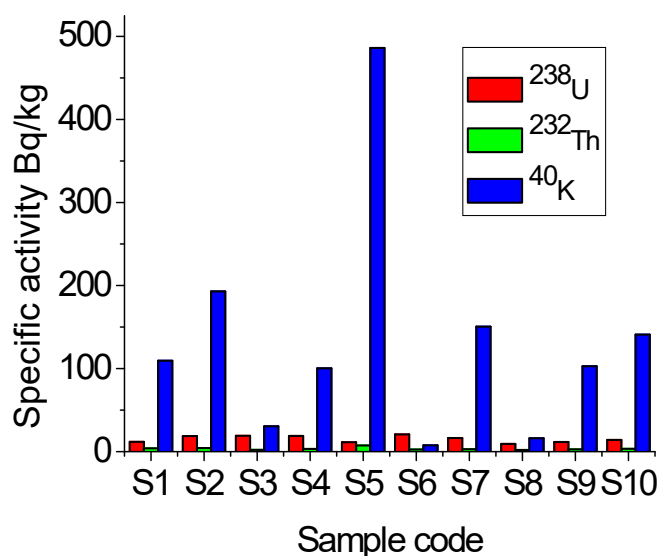
where Ns is the net peak area at a certain energy, ε_{γ} is the efficiency of the detector for a specific gamma ray energy, I_{γ} is the emission probability of radionuclide of interest, t is the total counting time and m_c is the mass of the sample.

Results and Discussion

The measured activity concentrations of three naturally occurring radionuclides (^{226}Ra , ^{232}Th and ^{40}K) in different cement samples are given in Table 2. The results are provided as a bar graph in Fig. 1.

TABLE 2. Specific activities of primordial radionuclides in cement samples.

Sample code	^{238}U Bq/kg	^{232}Th Bq/kg	^{40}K Bq/kg
S1	11.804±0.143	3.98±0.167	109.432±1.661
S2	18.678±0.18	4.308±0.174	192.974±2.206
S3	19.009±0.181	2.152±0.123	30.461±0.876
S4	18.958±0.181	3.191±0.15	100.369±1.591
S5	11.284±0.14	7.416±0.228	486.029±3.501
S6	20.768±0.189	2.678±0.137	7.654±0.439
S7	16.444±0.169	2.94±0.144	150.554±1.948
S8	9.234±0.126	2.089±0.121	16.073±0.637
S9	11.548±0.141	2.735±0.139	102.86±1.61
S10	14.162±0.156	3.359±0.154	140.95±1.885

FIG. 1. ²³⁸U, ²³²Th and ⁴⁰K activity concentrations across sample codes.

As can be seen from Table 2, the activity concentrations of ²²⁶Ra and ²³²Th of cements were lower than those of the world average for soil of 35 Bqkg⁻¹ and 30 Bqkg⁻¹, respectively [2]. For all cement samples under investigation, the measured ²³²Th activities were in the range 2.08-7.41 Bq /kg, lower than the ²³⁸U activities, while the observed ⁴⁰K activities were in the range 30.4-486 Bq/kg.

Determination of Hazard Indices

Radium Equivalent Activity (Ra_{eq})

The distribution of natural radioactivity in building material is not uniform; so, the specific activity of ²²⁶Ra, ²³²Th and ⁴⁰K can be represented by a single quantity (Ra_{eq}) which is

introduced by [11] and mathematically calculated as

$$Ra_{eq.} = A_{Ra} + 1.43A_{Th} + 0.077A_K \quad (2)$$

where A_{Ra} , A_{Th} and A_K are the activity concentration of ²²⁶Ra, ²³²Th and ⁴⁰K, respectively. It has been assumed that 1 Bq/kg of ²²⁶Ra, 0.7 of ²³²Th and 13 Bq/kg of ⁴⁰K produces the same gamma ray dose rate.

The measured values of Ra_{eq} of cement samples ranged from 13.45 (S8) to 59.3 (S5) Bq/kg, as shown in Table 3, which are all below the admissible level of 370 Bq/kg suggested by [2]. Table 4 presents a comparison of the reported values of mean radium equivalent for selected cements obtained in other countries with those determined in the present study.

TABLE 3. The radioactive doses and radiological hazard indices of primordial Radionuclides in cement samples.

Sample code	$Ra_{eq.}$ (Bq/kg)	$D_{in}(nGyh^{-1})$	$E_{in}(mSv/y)$	H_{in}
S1	25.922	24.172	0.118	0.101
S2	39.697	37.665	0.184	0.157
S3	24.433	22.437	0.109	0.117
S4	31.251	29.195	0.142	0.135
S5	59.314	57.975	0.284	0.19
S6	25.187	22.800	0.111	0.124
S7	32.242	30.656	0.149	0.131
S8	13.459	12.150	0.059	0.061
S9	24.873	22.034	0.117	0.104
S10	30.254	28.226	0.142	0.133

TABLE 4. Comparison of mean radium equivalent values with those of previous studies.

Country	Ra _{eq.} (Bq/kg)	References
Iran	103.32	[10]
Nigeria	98.1	[12]
Iraq	68.21	[13]
Turkey	73	[14]
India	102.011	[6]
Egypt	63.4	[7]
Slovakia	47.1	[8]
Italy	159	[15]
Greece	132	[15]
Netherlands	174	[15]
Erbil, Kurdistan	30.46	Present work

Indoor Annual Effective Dose Rate (E_{in})

Indoor Annual Effective Dose Rate can be defined as the amount of dose received by individuals inside buildings. (E_{in}) can be obtained from the indoor absorbed dose $D_{in}(nGyh^{-1})$ given as:

$$D_{in}(nGyh^{-1}) = 0.926A_{Ra} + 1.1A_{Th} + 0.081A_K. \quad (3)$$

The calculated $D_{in}(nGyh^{-1})$ values are shown in Table 3.

Using the dose conversion factor (0.7) and the time (0.8) of stay in the indoor during the year, the indoor annual effective dose is defined as follows [7]:

$$E_{in}(mSv\ y^{-1}) = D_{in}(nGyh^{-1}) \times 8760h \times 0.8 \times 0.7Sv\ Gy^{-1} \times 10^{-6}. \quad (4)$$

Table 3 presents the calculated E_{in} for cements. E_{in} values varied from 0.059 (S8) to 0.284 (S5) mSv/y. All the obtained values are below the average recommendation value of 0.41 mSv/y declared by [2] for indoor annual effective dose rates.

Internal Hazard Index (H_{in})

Internal exposure of radon and its progenies is defined by estimating internal hazard index, which is given by the formula [7]:

$$H_{in} = \frac{A_{Ra}}{185} + \frac{A_{Th}}{259} + \frac{A_K}{4810}. \quad (5)$$

The H_{in} values are shown in Table 3. The range of H_{in} varied from 0.061 (S8) to 0.19 (S5) with an average value of 0.287. All the obtained values of H_{in} are well below the critical value of one. This means that there are no risks to inhabitants owing to harmful effects of ionizing radiation from the natural radionuclides in cements; so, hazards can be neglected [7].

Conclusion

The specific activity of the three radionuclides ^{226}Ra , ^{232}Th and ^{40}K has been determined for local and imported cements in Erbil governorate. Based on the activity concentrations, the indoor dose rate was estimated for individuals in dwellings. The indoor dose rate was increased over life period for all cement samples. Fortunately, all the obtained values are well below the critical values presented by EPA. So, the cements used in Erbil governorate are safe and do not pose any radiological risks to dwellers.

References

- [1] Gilmore, G., "Practical Gamma-Ray Spectroscopy", (John Wiley & Sons, 2008).
- [2] UNSCEAR. "Sources and Effects of Ionizing Radiation", Report to the General Assembly, with Scientific Annexes, United Nations Publications, Vol. 1: Sources, (2000).
- [3] European Commission, "Radiological Protection Principles Concerning the Natural Radioactivity of Building Materials". In: EC Radiation Protection 112. (Directorate-General Environment, Nuclear Safety and Civil Protection, 1999).
- [4] UNSCEAR, "Effects and Risks of Ionizing Radiation", Report to the General Assembly, with Annexes, United Nations, NewYork, (1982).
- [5] Al-Sulaiti, H. et al., Nuclear Instruments and Methods in Physics Research-Section A: Accelerators, Spectrometers, Detectors and Associated Equipment, 652 (1) (2011) 915.
- [6] Rafique, M. et al., Journal of Radiation Research and Applied Sciences, 7 (1) (2014) 29.
- [7] Shoeif, M.Y. and Thabayneh, K.M., Journal of Radiation Research and Applied Sciences, 7 (2) (2014) 174.
- [8] Estokova, A. and Palascakova, L., Chemical Engineering Transactions, 32 (2013) 1675.
- [9] Kovler, K. and Schroeyers, W., Natural Radioactivity in Construction, Special Issue (2017).
- [10] Mehdizadeh, S., Faghihi, R. and Sina, S., Nukleonika, 56 (4) (2011) 363.
- [11] Beretka, J. and Matthew, P.J., Health Physics, 48 (1) (1985) 87.
- [12] Meindinyo, R.K., Agbalagba, E. and Olali, S.A., IOSR Journal of Research & Methods in Education (IOSR-JRME), 7 (2) (2017) 56.
- [13] Abojassim, A.A., Al-Taweel, M.H. and Abdulwahid, T.A., International Journal of Science & Engineering Research, 5 (3) (2014) 218.
- [14] Özdiş, B.E., Çam, N.F. and Öztürk, B.C., Journal of Radioanalytical and Nuclear Chemistry, 311 (1) (2017) 307.
- [15] Trevisi, R. et al., Journal of Environmental Radioactivity, 105 (2012) 11.

Thermoelectric Properties of ALiF_3 (A= Ca, Sr and Ba): First-Principles Calculation

Nada T. Mahmoud^a, Ahmad A. Mousa^b and Jamil M. Khalifeh^a

^a Physics Department, The University of Jordan, 11942-Amman, Jordan.

^b Middle East University (MEU), 11831-Amman, Jordan.

Received on: 28/10/2019;

Accepted on: 4/3/2020

Abstract: The energy band structure obtained from WIEN2k calculations is used to calculate the transport coefficients *via* the semi-classical Boltzmann transport theory with constant relaxation time (τ) as employed in the BoltzTraP package for ALiF_3 (A= Ca, Sr and Ba) using mBJ-GGA potential. The thermoelectric properties of the above compounds are investigated through the calculation of the main transport properties: Seebeck coefficient (S), electrical (σ) and electronic thermal (k_e) conductivity, figure of merit (ZT) and power factor. All compounds show insulating behavior.

Keywords: Fluoroperovskite, Band gap, BoltzTraP, Thermoelectric properties, Figure of merit.

Introduction

Searching for new materials with efficient thermoelectric (TE) properties has attracted great interest from researchers in order to obtain a better conversion of energy from waste heat to electricity [1, 2]. To date, it has been shown that many classes of material have promising TE properties, such as complex oxides [3, 4], Skutterudites [5, 6], Clathrates [7, 8] and half Heusler [9, 10].

We previously investigated the optical and electronic properties of XLiF_3 (X = Ca, Sr and Ba) using first-principles calculation. The study has shown the presence of a direct band gap (Γ - Γ) [11]. Furthermore, we have shown that the electronic, structural, optical and magnetic properties of SrLiF_3 compounds have been changed by inserting Eu ions in Sr sites [12].

Perovskite compounds have an interesting history of being considered for thermoelectric applications due to their low thermal conductivity and high Seebeck coefficient. Some of perovskite materials can be used as an

alternate source for renewing waste heat caused by industries. In a very recent investigation, the electronic, structural and thermoelectric transport properties of KCaF_3 compounds by ab-initio method were studied. The calculated electronic structures indicated that KCaF_3 is an insulator [13].

Calculation Method

We performed self-consistent calculations based on density functional theory (DFT) [14] using the full-potential linearized augmented plane wave (FP-LAPW) approach as implemented in the Wien2k package [15]. In this approach, we partitioned the unit cell into two regions: the first is atomic muffin-tin centered spheres with radii RMT and the second is interstitial region [16]. The exchange and correlation potential is used within the modified Becke-Johnson (mBJ) [17]. Our compounds are in Pm-3m (#221) space group with a cubic structure. The maximum quantum number ℓ for the wave function expansion inside the atomic

muffin-tin spheres is taken up to $\ell_{\max} = 10$. The core cut-off energy is -6 Ry and the plane wave cut-off 16 Ry is chosen for the expansion of wave functions in the interstitial region. The charge density is Fourier expanded up to $G_{\max} = 12$. For the Kmesh sampling, we used the $14 \times 14 \times 14$ mesh of points for structural and electronic properties' calculations. The lattice parameters are calculated using the Murnaghan's equation of state [18]. The calculations are carried out self-consistently and the results are taken when the convergence tolerance of charge is less than 10^{-4} electron charge.

Band structure energies obtained from WIEN2k calculations, using mBJ approximations, enable us to calculate the transport properties of ALiF_3 (A= Ca, Sr and Ba). The different transport coefficients are calculated using the semi-classical Boltzmann transport theory within the constant relaxation time (τ) approximation as employed in the BoltzTraP computer package [19, 20]. Dense k-mesh of $40 \times 40 \times 40$ in the full Brillouin zone is used to gain meaningful results. The main transport coefficients are electrical conductivity (σ), electronic thermal conductivity (K_e) and Seebeck coefficient (S). They are given by the following formulae [21]:

$$\sigma = e^2 \int dE \left(\frac{\partial f_0}{\partial E} \right) \Sigma(E) \quad (1)$$

$$K_e = \frac{1}{T} \int dE \left(-\frac{\partial f_0}{\partial E} \right) \Sigma(E) (E - \mu)^2 \quad (2)$$

$$S = \frac{e}{\sigma T} \int dE \left(-\frac{\partial f_0}{\partial E} \right) \Sigma(E) (E - \mu) \quad (3)$$

where,

$$\left(-\frac{\partial f_0}{\partial E} \right) = \frac{1}{K_B T} \frac{\exp\left(\frac{E - \mu}{K_B T}\right)}{\left(\exp\left[\left(\frac{E - \mu}{K_B T}\right)\right] + 1\right)^2} \quad (4)$$

and $\Sigma(E)$ is the transport distribution function given by [21]:

$$\Sigma(E) = \frac{2}{3} \int \frac{d^3 k}{(2\pi)^3} v_k^2 \tau(k) \delta\left(E - E_c - \frac{\hbar^2 k^2}{2m_e^*}\right). \quad (5)$$

Here, v_k and m_e^* are the velocity and the effective mass of the electron in the conduction band, respectively. E_c is the minimum energy of the conduction band.

In the general case, TE's efficiency is characterized by the dimensionless figure of merit ZT. It determines the thermoelectric performance of materials. In other words, the

material having better TE performance has larger ZT value [21], defined as:

$$ZT = \frac{\sigma S^2}{K_e + K_l} T \quad (6)$$

where, $k_e + k_l$ and T are the total thermal conductivity K and temperature, respectively. For practical applications, materials with $ZT \geq 1$ are required. Larger ZT requires greater σ and smaller K (total thermal conductivity) for good practical thermal electric system.

Results and Discussion

Band Gap and Density of States

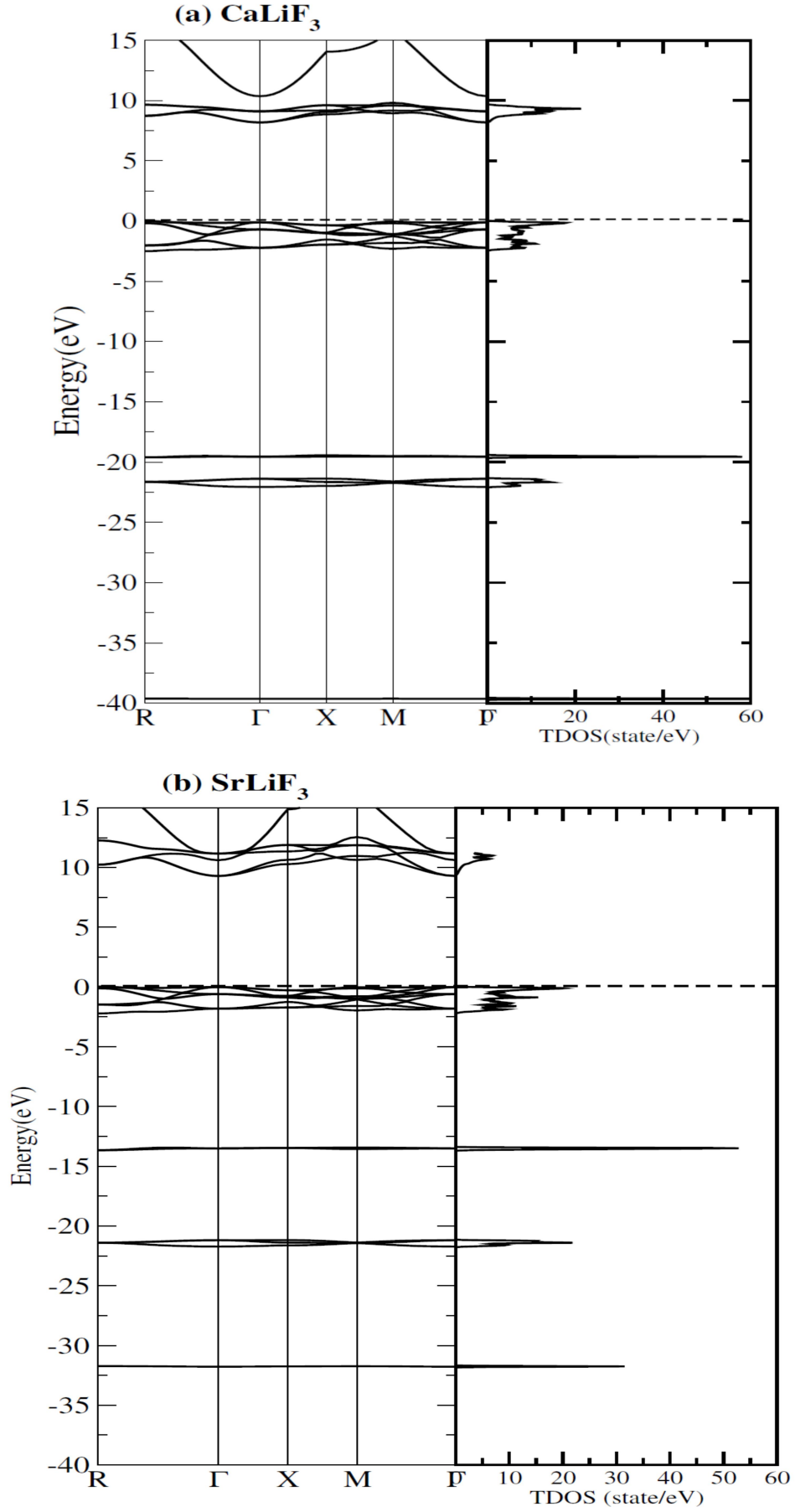
Our previous band structure calculations through DFT indicated that the three perovskite systems ALiF_3 (A= Ca, Sr and Ba) are insulators using GGA approximation [11] and mBJ-GGA potentials [22, 23] and the energy band gap (E_g) values are: 8.202eV, 9.399eV and 8.199eV for CaLiF_3 , SrLiF_3 and BaLiF_3 , respectively.

Fig.1 shows the band structure and density of states for the investigated systems. The energy band gap (E_g) is found to be direct (Γ - Γ) for both SrLiF_3 and BaLiF_3 compounds and indirect (M - Γ) for CaLiF_3 .

Thermoelectric Properties

Using the energy eigenvalues obtained from the DFT calculations by solving the Boltzmann semi-classical equation with constant relaxation time (τ) approximation using the BoltzTrap computer packages, we investigate the electronic transport coefficients. The calculated coefficients are: the electrical conductivity (σ/τ), thermal conductivity (κ/τ), Seebeck coefficient (S), figure of merit (ZT) and power factor as a function of temperature.

The electrical conductivity (σ/τ) is displayed for CaLiF_3 , SrLiF_3 and BaLiF_3 compounds in Fig. 2. It is obvious that electrical conductivity is a function of temperature; this is a typical behavior of insulators [19]. All compounds indicate minimum value of (σ/τ) at low temperature (50 K) equal to $0.591 \times 10^{18} (1/\Omega \cdot \text{m} \cdot \text{s})$, the maximum values reach $26.732 \times 10^{18} (1/\Omega \cdot \text{m} \cdot \text{s})$, $38.000 \times 10^{18} (1/\Omega \cdot \text{m} \cdot \text{s})$ and $30.232 \times 10^{18} (1/\Omega \cdot \text{m} \cdot \text{s})$ at 800K temperature for CaLiF_3 , SrLiF_3 and BaLiF_3 , respectively. The electrical conductivity calculation agrees with band structure calculations (Fig. 1).



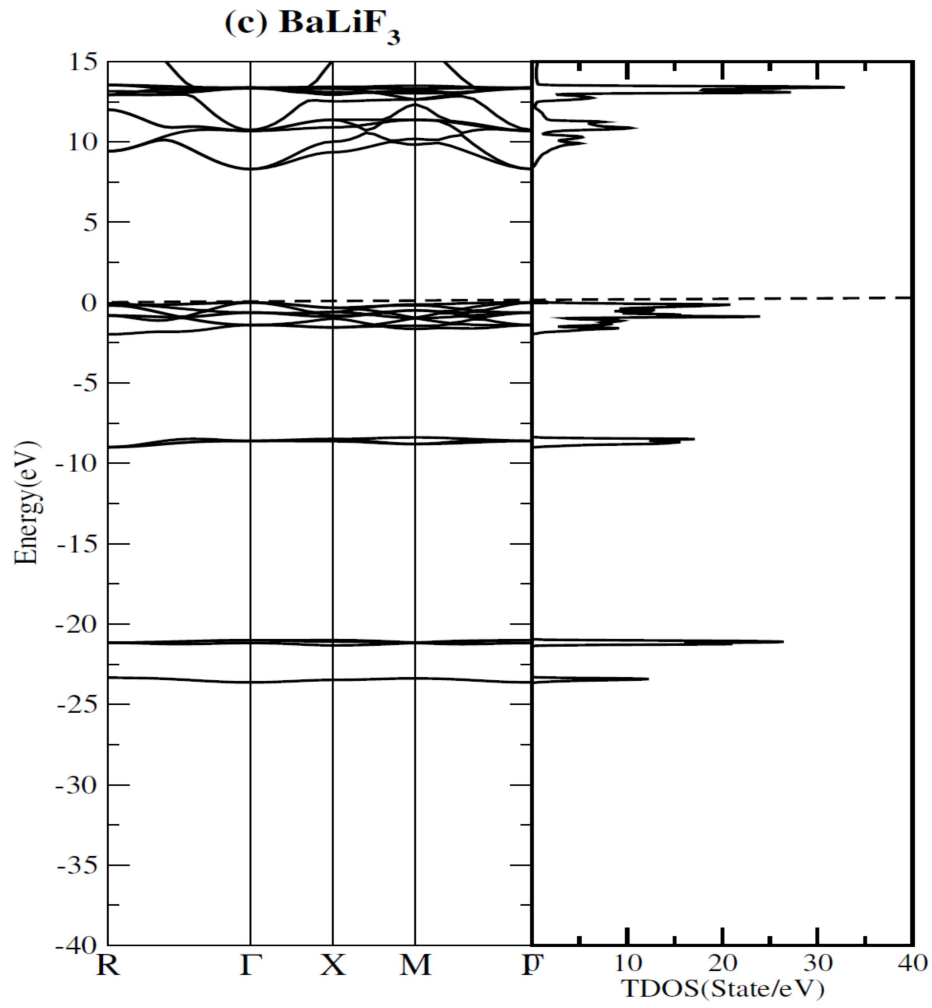


FIG. 1. Electronic band structure and density of states (a) CaLiF₃, (b) SrLiF₃ and (c) BaLiF₃.

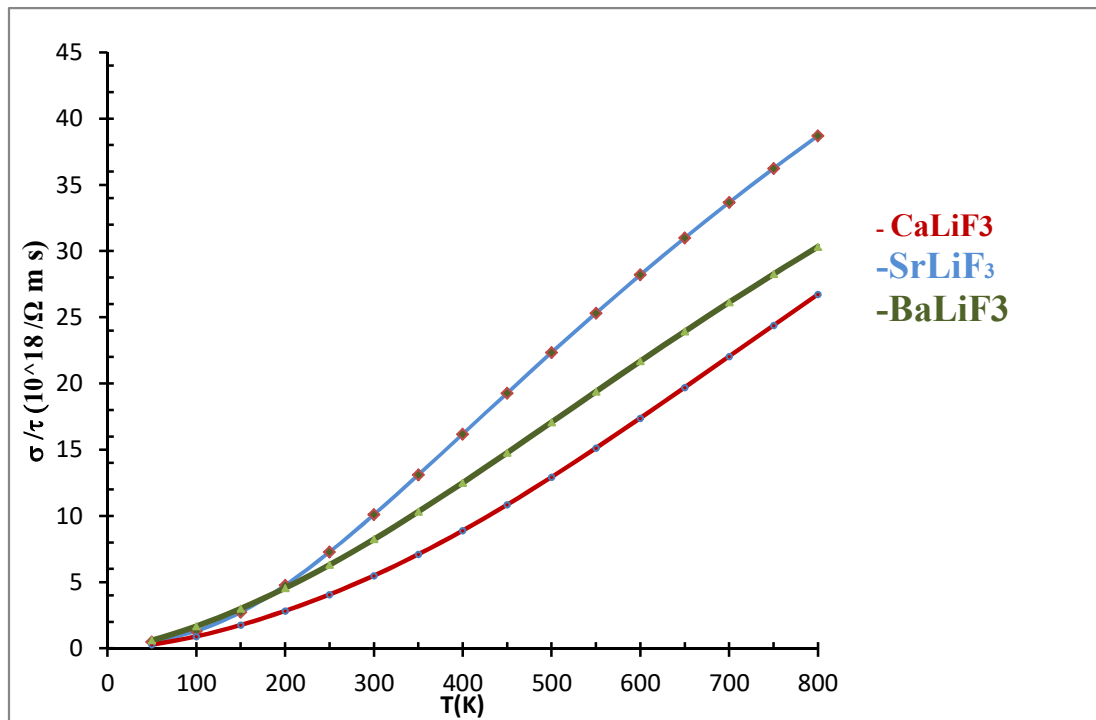


FIG. 2. Electrical conductivity, $\sigma / \tau (10^{18} / \Omega \cdot m \cdot s)$.

In our calculations, CaLiF_3 , SrLiF_3 and BaLiF_3 show thermal insulating behavior, where thermal conductivity k_e/τ increases as temperature increases (Fig. 3). The increase in k_e/τ arises from heating material which increases atomic vibrations to a limit such that they transmit energy in the form of kinetic energy. The values of k_e/τ , at the whole range of temperature, for both CaLiF_3 and BaLiF_3 compounds are comparable, since E_g for both of them is almost equal. At low temperature (zero Kelvin), the material is an insulator (8.202eV, 9.399eV and 8.199eV for CaLiF_3 , SrLiF_3 and BaLiF_3 , respectively). The total thermal conductivity (k_e+k_l) increases at high temperature. The contribution of the lattice thermal conductivity (k_l) resulting from phonon-phonon interaction is responsible of the total thermal conductivity. Thermal conductivity here is due to the electronic part only, which is equal to 3.2 (W/ m.K), 1.9 (W/ m.K) and 1.2 (W/ m.K) for SrLiF_3 , BaLiF_3 and CaLiF_3 , respectively, at $T=300$ K. If k_l were (not calculated here) considered in the calculations, then the estimated total K would be larger than k_e . As a result, ZT value is expected to be smaller than the observed one [24, 25]. That is; the total thermal conductivity is enhanced by increasing temperature.

Fig. 4 illustrates the temperature dependence of Seebeck coefficient. The S values for CaLiF_3 and BaLiF_3 show very small decrement after

300K, and almost constant in all the range of temperature for CaLiF_3 perovskite.

SrLiF_3 perovskite shows a decreasing trend of S value beyond 300K (room temperature) which is a typical behavior for insulators in agreement with band structure calculations. The minimum value of S is found at 50K for all compounds. Meanwhile, the maximum value of Seebeck coefficient occurs almost at room temperature (300K), as listed in Table (1).

TE efficiency of the device can be described in terms of ZT. For practical applications, $ZT \geq 1$ for good heat conversion [17]. ZT for both CaLiF_3 and BaLiF_3 show a small increase beyond 300K. On the other hand, ZT value of SrLiF_3 tends to decrease beyond 300K; one can notice this behavior clearly in Fig. 5. The value of ZT at room temperature (300K) for the three compounds is presented in Table 1; it is obvious that ZT values are less than one.

Using the values of (S) and (σ/τ) , one can calculate the power factor ($S^2\sigma$). The electric power factor is reported in Fig.6. The power factor increases monotonically with the increase in temperature from 100K to 800K for all compounds. The maximum value of the calculated power factor is $1.480 \times 10^{12} (\text{W/mK}^2)$, $1.630 \times 10^{12} (\text{W/mK}^2)$ and $1.340 \times 10^{12} (\text{W/mK}^2)$ for CaLiF_3 , SrLiF_3 and BaLiF_3 , respectively.

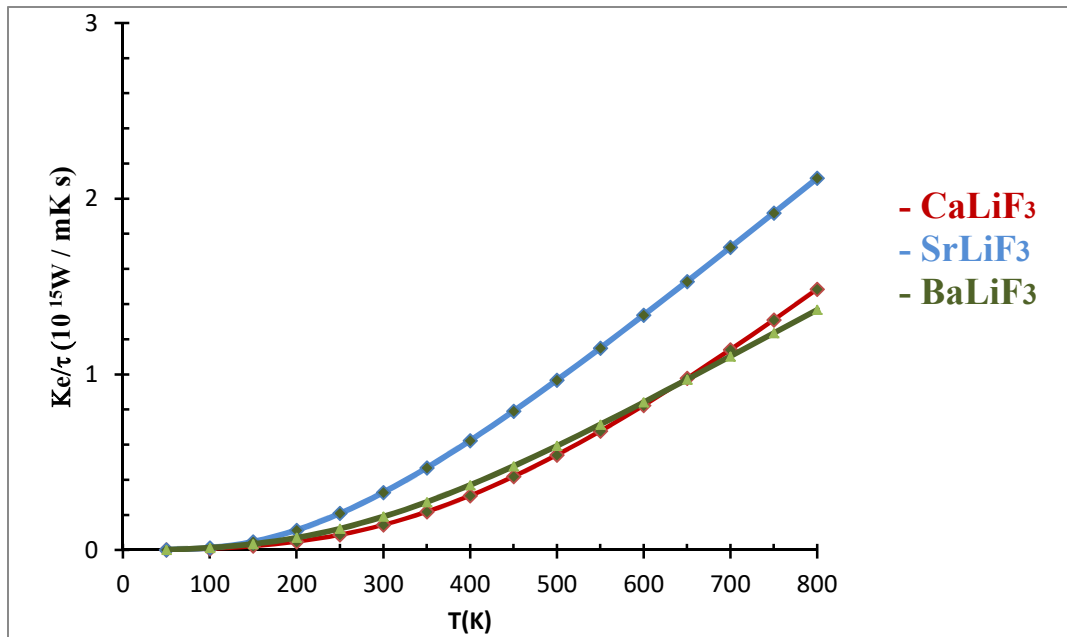
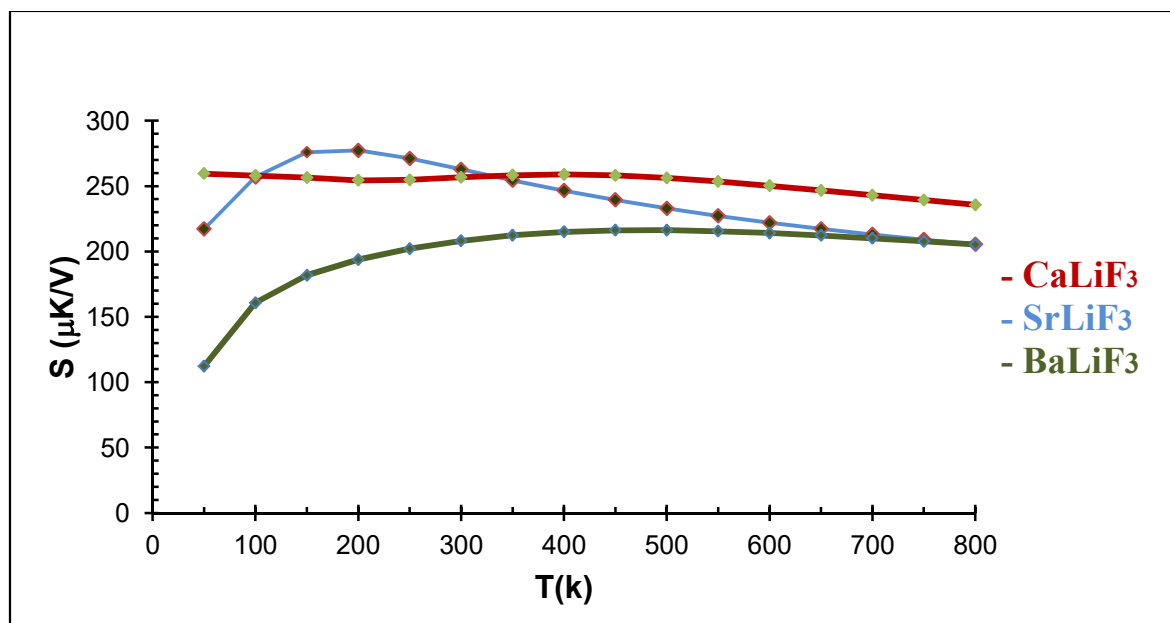
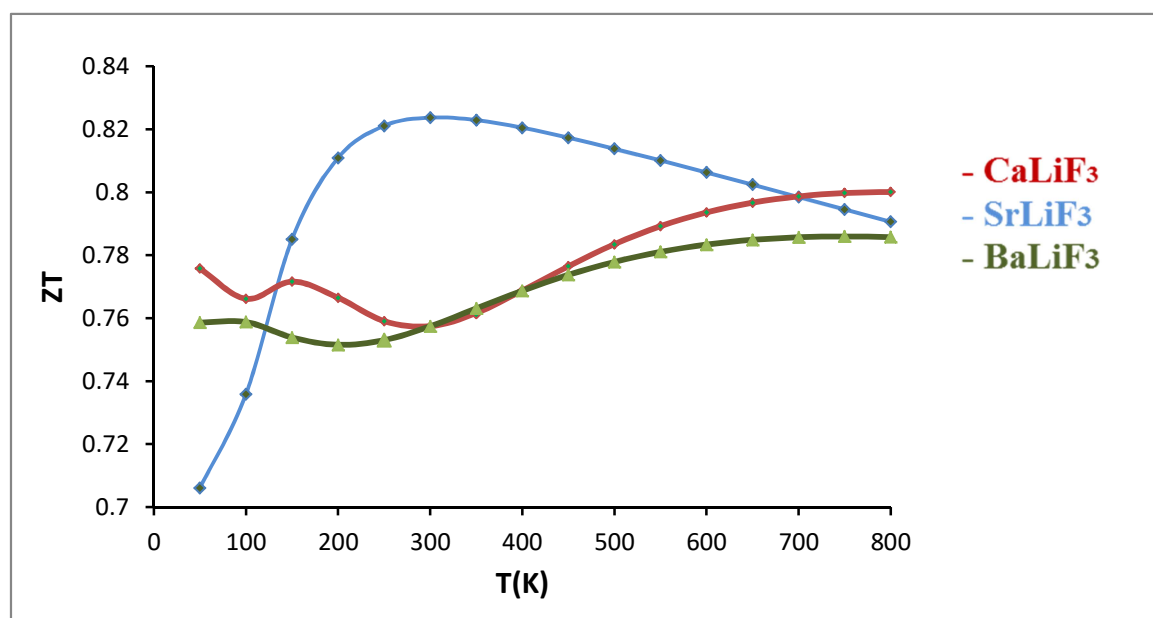
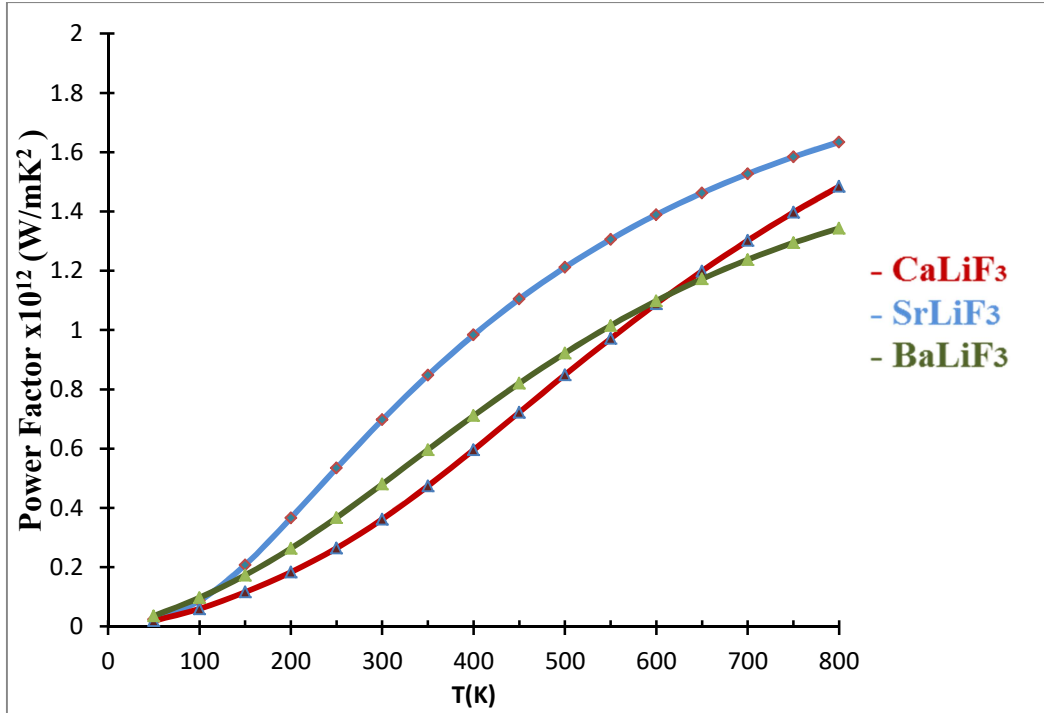


FIG. 3. Electronic thermal conductivity, K_e/τ (10^{15} W / m K s).

FIG. 4. The Seebeck coefficient ($\mu\text{V/K}$).TABLE 1. Seebeck coefficient ($\mu\text{V/K}$) and figure of merit ZT at room temperature 300K.

Compound	Seebeck Coefficient ($\mu\text{V/K}$)	Figure of merit ZT
CaLiF_3	256.665	0.758
SrLiF_3	262.778	0.806
BaLiF_3	241.480	0.757

FIG. 5. The figure of merit (ZT).

FIG. 6. The power factor (10^{12}W/mK^2).

Conclusion

Thermoelectric properties of ALiF_3 (A= Ca, Sr and Ba) perovskite are calculated using the energy eigenvalues obtained from the DFT calculations by solving the Boltzmann semi-classical equation using the BoltzTrap code. The calculations of the (σ/τ) and (κ/τ) as a function of temperature are found in agreement with band structure calculations. Meanwhile, Seebeck coefficient (S) is also calculated for the three systems. The results show that the S value is decreasing with temperature above 300K for all compounds. The values of S for all systems are calculated at 300K.

TE efficiency is characterized by the dimensionless quantity ZT, the value of ZT is almost constant above 300K for BaLiF_3 and increases with temperature for CaLiF_3 compound, while it decreases with temperature for SrLiF_3 .

Although it is often supposed that TE devices made of materials with a higher power factor are capable of generating more energy, this is only true for a thermoelectric device with fixed geometry and unlimited heat source and cooling. If the geometry of the device is designed for specific application, the maximum functionality of TE materials will be determined by their ZT, not $S^2\sigma$ [26]. The investigated systems are not suitable for TE devices, as they act as insulators.

Acknowledgment

This work is carried out during my sabbatical year (2019/2020) at the University of Jordan. A research project supported by the Deanship of Academic Research at the University of Jordan is also acknowledged (J. M. Khalifeh).

References

- [1] Zheng, X., Liu, C., Yan, Y. and Wang, Q., *Renew. Sustain. Energy Rev.*, 32 (2014) 486.
- [2] Twaha, S., Zhu, J., Yan, Y. and Li, B., *Renew. Sustain. Energy Rev.*, 65 (2016) 698.
- [3] Koumoto, K., Terasaki, I. and Funahashi, R., *Mater. Res. Soc. Bull.*, 31 (3) (2006) 206.
- [4] Koumoto, K., Wang, Y., Zhang, R., Kosuga, A. and Funahashi, R., *Annu. Rev. Mater. Res.*, 40 (2010) 363.
- [5] Rogl, G. and Rogl, P., *Green Sustain. Chem.*, 4 (2017) 50.
- [6] Rull-Bravo, M., Moure, A., Fernandez, J. and Martin-Gonzalez, M., *RSC Adv.*, 5 (52) (2015) 41653.
- [7] Iversen, B.B., Palmqvist, A.E., Cox, D.E., Nolas, G.S., Stucky, G.D., Blake, N.P. and Metiu, H., *J. Solid State Chem.*, 149 (2) (2000) 455.
- [8] Norouzzadeh, P., Myles, C.W. and Vashae, D., *Sci. Rep.*, 4 (2014) 7028.
- [9] Kangsabanik, J. and Alam, A., *J. Mater. Chem. A*, 5 (13) (2017) 6131.
- [10] Zhao, D., Wang, L., Bo, L. and Wu, D., *Metals*, 8 (1) (2018) 61.
- [11] Mousa, A.A., Mahmoud, N.T. and Khalifeh, J.M., *Computational Materials Science*, 79 (2013) 201.
- [12] Mahmoud, N.T., Khalifeh, J.M. and Mousa, A.A., *Physica B: Condensed Matter*, 564 (2019) 37.
- [13] Ali, A., Ur Rahman, A. and Rahman, G., *Physica B: Condensed Matter*, 565 (15) (2019) 18.
- [14] Kohn, W. and Sham, L.J., *Phys. Rev.*, 140A (1965) 1133.
- [15] Blaha, P., Schwarz, K., Madsen, G., Kvasnika, D. and Luitz, K., "WIEN2k", (Technical Universität Wien, Austria, 2001). ISBN3-9501031-1-2.
- [16] Blaha, P., Schwarz, K., Sorantin, P. and Trickey, S.B., *Comput. Phys. Commun.*, 59 (2) (1990) 399.
- [17] Tran, F. and Blaha, P., *Phys. Rev. Lett.*, 102 (1-2) (2009) 226401.
- [18] Murnaghan, F.D., *Proc. Natl. Acad. Sci.*, 30 (1944) 244.
- [19] Alrahamneha, M.J., Mousa, A.A. and Khalifeh, J.M., *Physica B: Condensed Matter*, 552 (2019) 227.
- [20] Madsen, G.K. and Singh, D.J., *Computer Physics Communications*, 175 (1) (2006) 67.
- [21] Mahan, G. and Sofo, J., *Proceedings of the National Academy of Sciences*, 93 (15) (1996) 7436.
- [22] Goldsmid, H., *British Journal of Applied Physics*, 11 (6) (1960) 209.
- [23] Mahmoud, N.T., Khalifeh, J.M. and Mousa, A.A., *Computational Condensed Matter*, 21 (2019) e00432.
- [24] Arcroft, N.W. and Mermin, N.D., "Solid state physics", (New York : Holt, Rinehart and Winston, 1976).
- [25] Tan, X., Devlin, K.P., Deng, X., Kang, C. and Croft, M., *Chem. Mater.*, 30 (2018) 4207.
- [26] Baranowski, L.L., Toberer, E.S. and Snyder, G.J., *Journal of Applied Physics*, 115 (2013) 126102.

Jordan Journal of Physics

Technical Note

High Efficiency of Solar Cell Model Based on Two Types of Nanoparticles

Kholoud Kh. Abushaar^a, Mohammed M. Shabat^a, Dena M. El-Amassi^a and Daniel M. Schaadt^b

^a *Departement of Physics, Islamic University of Gaza, P.O. Box 108, Gaza Strip, Palestine..*

^b *Institute of Energy Research and Physical Technologies, Clausthal University of Technology, Leibnizstr. 4, 38678 Clausthal-Zellerfeld, Germany..*

Received on: 02/07/2019;

Accepted on: 13/10/2019

Abstract: Novel solar cell structure based on multi-type nanoparticles layer has been investigated. The transmission and reflection of the incident light have been computed by the Transfer Matrix Method for different physical parameters of the structure and the numerical results are obtained by Maple program software. We found that the types of nanoparticles on the proposed anti-reflective (AR) structure have effectively enhanced transmission and minimized reflection.

Keywords: Anti-reflective, Metallic, Nanoparticles, Reflection, Solar cell, Transmission.

Introduction

Photovoltaic or solar cells are among of the key elements of renewable energy sources which convert sunlight into electrical power. This technology may meet the demand of the increasing need for energy. Absorption, reflection and transmissions are very important parameters which influence photovoltaic solar cell efficiency. Solar cells have attracted the attention of researchers and industry worldwide through research on both raw materials and the fabrication process in order to reduce the processing cost and solar cell size to meet the worldwide demand on energy [1-6].

The basic key concept of effective solar cells depends on increasing the transmitted light and decreasing the reflected light, taking into account the concept of surface plasmons. Surface plasmons (SPs) are two-dimensional (2D) electromagnetic waves confined at the metal-dielectric interface [7-15], resulting from the coupling of the electromagnetic field to the collective plasma excitation. SPs show promise as a possible tool to control light at a

subwavelength scale [9-15], which has prospective uses in many practical applications, such as optical biosensing, waveguide devices and emitters [9-15]. SPs have been investigated in a large variety of metal-based systems as crystalline solar cells. Various solar cell structure models have been extensively investigated containing different materials as nanoparticles. One of the most approaches meeting the requirements of the concept of solar cell is the anti-reflected coating (ARC) by minimizing the reflected light [5-9]. Recently, there have been growing interests in using nanoparticles for designing solar cell models [5-21].

In this communication, we propose theoretically and numerically a novel solar cell model based on two types of nanoparticles.

Simulation Model and Theory

The solar cell model under investigation is a four-layered structure containing one film with nanoparticle materials. We examine the proposed structure for three cases: the first case

is with two nanoparticle materials (Ag and Au), the second case is with one type of nanoparticle either (Ag or Au) as shown in Fig. 1. The nanoparticle film is deposited on SiN and covered by an air layer. The refractive indices

are denoted as n_0 , n_1 , n_2 and n_s for air, (Ag-Au or Ag, Au), SiN and Si, respectively. The nanoparticle layer thickness is d_1 and the SiN layer thickness is d_2 .

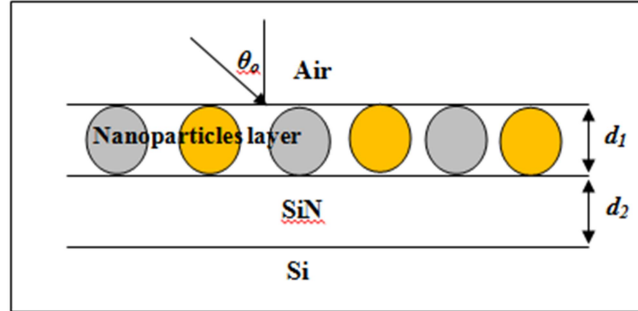


FIG. 1. Sketch of the Air-Nps-SiN-Si multilayer structure (solar cell model). The Np layer with the thickness d_1 and the SiN layer with the thickness d_2 are deposited on the Si substrate.

The effective permittivity of the nanoparticle-film with two types of nanoparticles is described by the Maxwell-Garnett mixing rule as [4]:

$$\varepsilon_{eff} = \varepsilon_o + 3\varepsilon_o \frac{f_1 \left(\frac{\varepsilon_1 - \varepsilon_o}{\varepsilon_1 + 2\varepsilon_o} \right) + f_2 \left(\frac{\varepsilon_2 - \varepsilon_o}{\varepsilon_2 + 2\varepsilon_o} \right)}{1 - \left[f_1 \left(\frac{\varepsilon_1 - \varepsilon_o}{\varepsilon_1 + 2\varepsilon_o} \right) + f_2 \left(\frac{\varepsilon_2 - \varepsilon_o}{\varepsilon_2 + 2\varepsilon_o} \right) \right]} \quad (1)$$

where ε_o is the permittivity of the host (base) material which equals 1, $\varepsilon_1 = (0.13455 - 3.98651i)^2$ is the permittivity of the silver nanoparticles, $\varepsilon_2 = (0.19715 - 3.0899i)^2$ is the permittivity of the gold nanoparticles and f_1 and f_2 are the volume fractions of Ag and Au nanoparticles in the host medium, respectively.

Following the notations and approaches used in [10, 21], both transmission and reflection can easily be derived.

Results and Discussion

The structure under consideration has a film consisting of two types of nanoparticles, (Ag-Au) with $n_{Ag} = 0.13455 - 3.98651i$, $n_{Au} = 0.19715 - 3.0899i$ on SiN ($n_2 = 2.24$) and covered by air with $n_0 = 1$ and the Si substrate with $n_s = 3.5$. The thicknesses d_1 and d_2 are taken to be equal to a

quarter of wavelength at each medium ($d_i = \lambda_i/4$), where $\lambda_i = \lambda/n_i$ and n_i is the refractive index for each medium. The wavelength λ is chosen close to the peak of the solar spectrum ($\lambda = 600\text{nm}$), as well noticed at the spectral response in the range (300-1200 nm). This range is taken to limit the spectrum of incident light. Also, it is worth mentioning that for Si technology, the infrared region is less important due to the gap of Si. The variation of the percentage of the transmitted and reflected light *versus* the wavelength of the incident light was computed and illustrated for different values of light incidence angle. The values of the volume fractions of the two nanoparticles ($f_1 = 0.15$, $f_2 = 0.05$) for Ag and Au, respectively, in the host medium are used in the computations.

Fig. 2 displays the effects of the solar cell model structure based on two types of nanoparticles (Ag-Au) through the concept of transmission. It has been noticed that the transmission coefficients are almost reaching 100% when incidence angle is equal to zero.

Moreover, an enhancement of the results has been observed over a good range, as we saw that the transmission coefficient is above 95% over the wavelength range term 450nm to 1100nm.

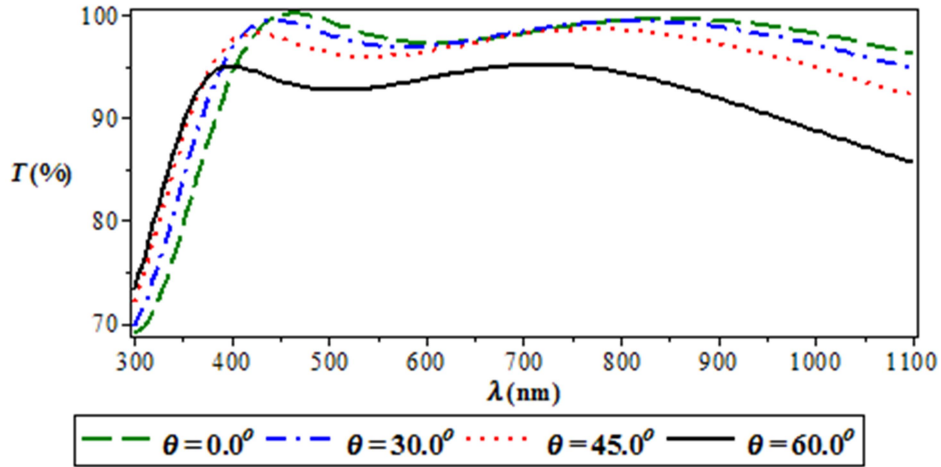


FIG. 2. Percentage of transmitted light *versus* incident light wavelength for different values of light incidence angle, where $d_1 = 600/4n_1$, $d_2 = 600/4n_2$, $\theta = 0.0^\circ$, $f_1 = 0.15$ and $f_2 = 0.05$.

Fig. 3 illustrates the reflection coefficients of the two types of nanoparticles (Ag and Au) *versus* the operating of light incident leading to minimum values. The reflection coefficients almost equal zero or the minimum values for a

long range of light wavelengths leading to remarkable solar enhancement.

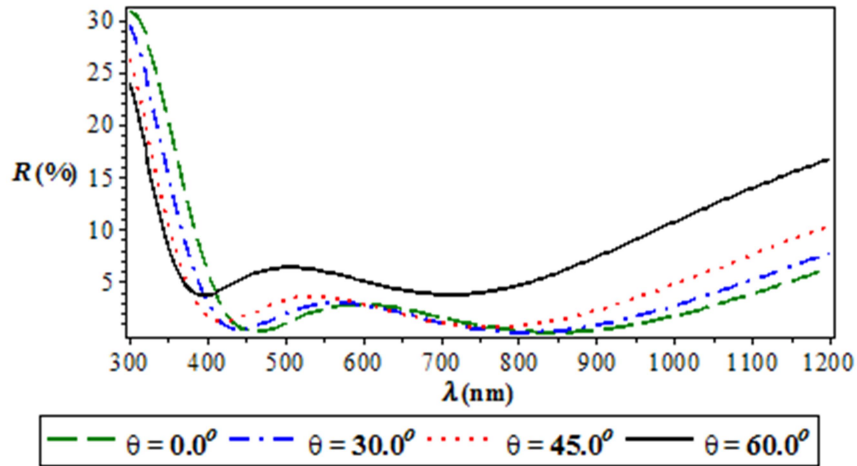


FIG. 3. Percentage of reflected light *versus* incident light wavelength for different values of light incidence angle, where $d_1 = 600/4n_1$ and $d_2 = 600/4n_2$.

Fig. 4 illustrates the effects of the fractions of the two types of nanoparticles (Ag-Au) on the efficiency of solar cell model structure. The percentage of the transmitted light *versus* the incident light wavelength for different values of volume of fraction shows equal fractions of the two types of nanoparticles or quantities of the two nanoparticles as $f_1 = 0.25$, $f_2 = 0.25$. It has been noticed that the mixture of the two equal quantities of nanoparticles as $f_1 = f_2 = 0.25$ is

the best state to achieve higher efficiency by getting lower reflection and higher transmission. Other nice views of the transmission of the proposed structure have been clearly noticed for different values of the nanoparticles of the two recommended types, Au and Ag. So, transmission can be controlled and adjusted by tuning or adopting the fractions of nanoparticles in the manufacturing process.

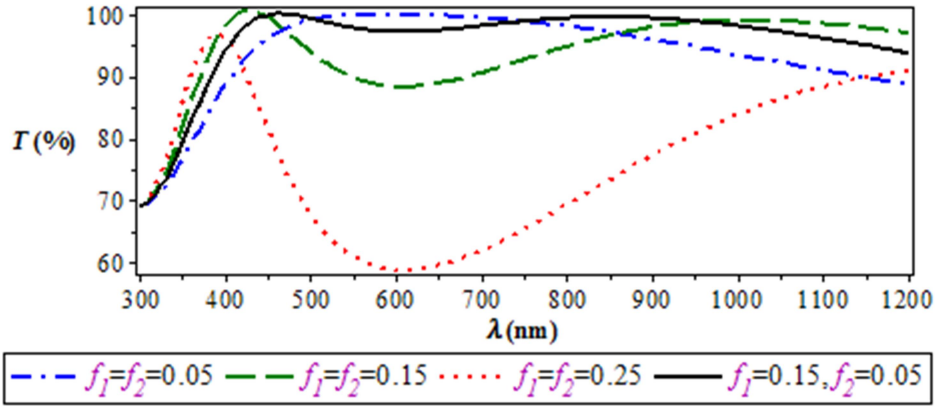


FIG. 4. Percentage of transmitted light *versus* incident light wavelength for different values of volume of fraction, where $d_1 = 600/4n_1$, $d_2 = 600/4n_2$, $\theta = 0.0^\circ$, $f_1 = 0.15$ and $f_2 = 0.05$.

Fig. 5 shows the percentage of the reflected light *versus* incident light wavelength for different values of volume of fraction of the two types of nanoparticles with the same data of the

above figures of transmission. This figure demonstrates a good picture of the high efficiency of solar cells.

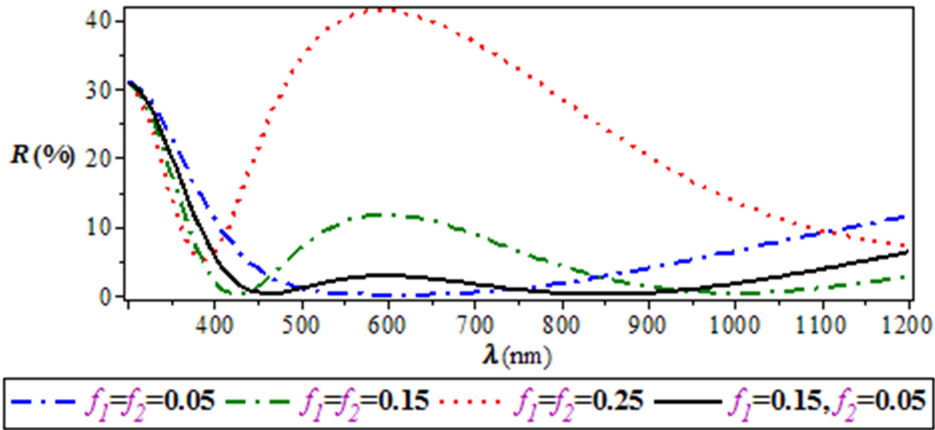


FIG. 5. Percentage of reflected light *versus* incident light wavelength for different values of volume of fraction, where $d_1 = 600/4n_1$, $d_2 = 600/4n_2$ and $\theta = 0.0^\circ$.

Figs. 6 and 7 shoe the effect of a new physical parameter of the proposed solar cells; thickness of the layer of SiN d_2 has been implemented to compute the percentage of transmitted light *versus* the incident light wavelength and the percentage of reflected light *versus* the incident light wavelength for various values of the thickness d_2 .

Widening the SiN layer leads to minimum percentage of reflected light *versus* the incident light wavelength at $d_2 = 60$ nm and $d_2 = 80$ nm, which confirms the concept that minimum reflected light occurs at the thickness equal to a quarter of the wavelength.

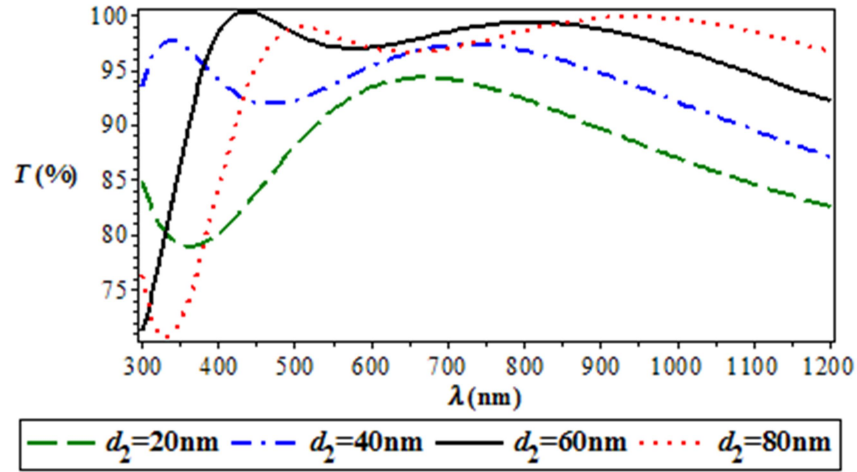


FIG. 6. Percentage of transmitted light *versus* incident light wavelength for various values of the thickness d_2 , $d_1 = 600/4n_1$, $f_1 = 0.15$, $f_2 = 0.05$ and $\theta = 0.0^\circ$.

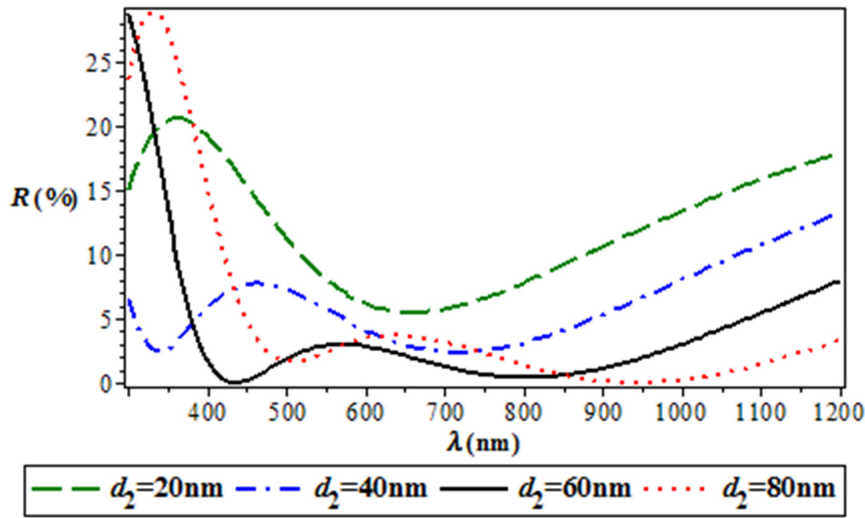


FIG. 7. Percentage of reflected light *versus* incident light wavelength for various values of the thickness d_2 , $d_1 = 600/4n_1$, $f_1 = 0.15$, $f_2 = 0.05$ and $\theta = 0.0^\circ$.

Conclusions

We have numerically investigated a novel proposed solar cell structure model based on two types of nanoparticles. Maximum transmission and minimum reflection have been achieved leading to higher solar cell efficiency. Higher efficiency can be obtained by adjusting the physical parameter of volume fraction of nanoparticles, the film thickness and the incident light angle in the proposed structure. The

obtained promising results of the structure model based on two types of nanoparticles could be used in designing future solar cells.

Acknowledgements

The authors (MMS, and Kh.Kh.Ab) acknowledge the financial support to this research presented by Alquds Academy for Scientific Research, Palestine.

References

- [1] Green, M.A., "Solar Cells: Operating Principles, Technology and System Applications", (Prentice Hall. 1982).
- [2] Hamouche, H. and Shabat, M.M., Applied Physics A, 122 (7) (2016) 1.
- [3] Hamouche, H., Shabat, M.M. and Schaadt, D.M., Superlattices and Microstructures, 101 (2017) 633.
- [4] Chen, L.F., Ong, C.K. and Tan, G.T.G., Journal of Material Science, 33 (1998) 5891.
- [5] Hamouche, H. and Shabat, M.M., Optical and Quantum Electronics, 50 (448) (2018) 1.
- [6] Würfel, P. and Würfel, U., "Physics of Solar Cells: from Basic Principles to Advanced Concepts", (John Wiley & Sons, 2009).
- [7] Ubeid, M.F. and Shabat, M.M., Journal of Nanoelectronics and Optoelectronics, 13 (2018) 1175.
- [8] Ubeid, M.F. and Shabat, M.M., Journal of Modern Optics, 64 (4) (2017) 374.
- [9] Schaadt, D.M., Feng, B. and Yu, E.T., Applied Physics Letters, 86 (2005) 063106.
- [10] Shabat, M.M., El-Amassi, D.M. and Schaadt, D.M., Solar Energy Journal, 137 (2016) 409.
- [11] Mousa, H.M. *et al.*, Modern Physics Letters B, 32 (15) (2018) 1850163.
- [12] Sun, Y. and Xia, Y., Science, 298 (5601) (2002) 2176.
- [13] Pillai, S., Catchpole, K.R., Trupke, T. and Green, M.A., J. Appl. Phys., 101 (2007) 093105.
- [14] Juan, F.C., Chaverri-Ramos, C. and Connolly, J., Journal of Renewable and Sustainable Energy, 5 (3) (2013) 033116.
- [15] Hägglund, C., Zäch, M., Petersson, G. and Kasemo, B., Appl. Phys. Lett., 92 (2008) 053110.
- [16] Atwater, H.A. and Polman, A., Nature Materials, 9 (3) (2010) 213.
- [17] Mousa, H.M., Shabat, M.M. and Ouda, A.K., J. Science and Engineering, B7 (2017) 229.
- [18] Qu, D., Liu, F., Yu, J., Xie, W., Xu, Q., Li, X. and Huang, Y., Appl. Phys. Lett., 98 (2011) 113119.
- [19] McFarland, A.D. and van Duyne, R.P., Nano Lett., 3 (8) (2003) 7433.
- [20] El-Khozondar, H., Alshembari, A.A., Shabat, M.M. and Koch, A., Optik, 181 (2019) 933.
- [21] Shabat, M.M., El-Khozondar, H.J. and AlShembari, A.A., Modern Physics Letters B, 32 (28) (2018) 1850346.

Authors Index

A. A. Mousa	79
A. Awadallah	1
A. Chahed	29
A. H. Ahmed	73
A. O. Jafir	73
A. Sayede	29
B. Amrani	29
B. M. Al-Khamiseh	59
D. M. El-Amassi	87
D. M. Schaadt	87
F. O. Aweda	17
H. M. Abdullah	73
I. Bsoul	1
J. M. Khalifeh	59, 67, 79
K. Benkaddour	29
Kh. Kh. Abushaar	87
M. B. Altaie	47
M. M. Shabat.	87
M. Rahmoune	29
N. M. Ershaidat	47
N. R. Suleiman	47
N. T. Mahmoud	79
O. A. Falaiye	17
Q. Al Sheyab	1
Q. I. Mohaidat	1
R. S. Hijjawi	59, 67
S. H. Mahmood	1
Y. M. Alawaideh	67
Y. Maswadeh	1

Subject Index

AAS.....	17
Anti-reflective	87
Band gap.....	79
BoltzTraP	79
Cement	73
Dark matter.....	47
Degasperis-Procesi equation	67
Electromagnetic field	59
Electronic structures.....	29
Euler-Lagrange.....	67
Figure of merit.....	79
Fluoroperovskite.....	79
FTIR.....	17
Functional derivatives	67
Gamma-ray spectrometer	73
Hamiltonian systems	67
Hamilton-Jacobi	59
Heusler alloys.....	29
Lagrangian mechanics.....	59
Magnetic properties.....	1, 29
Mechanical properties	29
Metallic	87
Mineralogy and element composition	17
Nanoparticles.....	87
Newtonian mechanics	59
PIXE.....	17
Quantum vacuum	47
Radionuclides.....	73
Reflection	87
Rotation curves.....	47
Solar cell.....	87
Spin reorientation transition	1
Staeckel boundary conditions.....	59
Structural properties	1
Thermoelectric properties.....	79
Thermomagnetic measurements.....	1
Transmission	87
W-type hexaferrites	1
XRF	17

المراجع: يجب طباعة المراجع بأسطر مزدوجة ومرقمة حسب تسلسلها في النص. وتكتب المراجع في النص بين قوسين مربعين. ويتم اعتماد اختصارات الدوريات حسب نظام Wordlist of Scientific Reviewers.

الجدول: تعطى الجداول أرقاماً متسلسلة يشار إليها في النص. ويجب طباعة كل جدول على صفحة منفصلة مع عنوان فوق الجدول. أما الحواشي التفسيرية، التي يشار إليها بحرف فوقي، فتكتب أسفل الجدول.

الرسوم التوضيحية: يتم ترقيم الأشكال والرسومات والرسومات البيانية (المخططات) والصور، بصورة متسلسلة كما وردت في النص.

تقبل الرسوم التوضيحية المستخرجة من الحاسوب والصور الرقمية ذات النوعية الجيدة بالأبيض والأسود، على أن تكون أصيلة وليست نسخة عنها، وكل منها على ورقة منفصلة ومعرفة برقمها بالمقابل. ويجب تزويد المجلة بالرسومات بحجمها الأصلي بحيث لا تحتاج إلى معالجة لاحقة، وألا تقل الحروف عن الحجم 8 من نوع Times New Roman، وألا تقل سماكة الخطوط عن 0.5 وبكثافة متجانسة. ويجب إزالة جميع الألوان من الرسومات ما عدا تلك التي ستنتشر ملونة. وفي حالة إرسال الرسومات بصورة رقمية، يجب أن تتوافق مع متطلبات الحد الأدنى من التمايز (1200 dpi Resolution) لرسومات الأبيض والأسود الخطية، و 600 dpi للرسومات باللون الرمادي، و 300 dpi للرسومات الملونة. ويجب تخزين جميع ملفات الرسومات على شكل (jpg)، وأن ترسل الرسوم التوضيحية بالحجم الفعلي الذي سيظهر في المجلة. وسواء أرسل المخطوط بالبريد أو عن طريق الشبكة (Online)، يجب إرسال نسخة ورقية أصلية ذات نوعية جيدة للرسومات التوضيحية.

مواد إضافية: تشجع المجلة الباحثين على إرفاق جميع المواد الإضافية التي يمكن أن تسهل عملية التحكيم. وتشمل المواد الإضافية أي اشتقاق رياضية مفصلة لا تظهر في المخطوط.

المخطوط المنقح (المعدل) والأقراص المدمجة: بعد قبول البحث للنشر وإجراء جميع التعديلات المطلوبة، فعلى الباحثين تقديم نسخة أصلية ونسخة أخرى مطابقة للأصلية مطبوعة بأسطر مزدوجة، وكذلك تقديم نسخة إلكترونية تحتوي على المخطوط كاملاً مكتوباً على Microsoft Word for Windows 2000 أو ما هو استجد منه. ويجب إرفاق الأشكال الأصلية مع المخطوط النهائي المعدل حتى لو تم تقديم الأشكال إلكترونياً. وتخزن جميع ملفات الرسومات على شكل (jpg)، وتقدم جميع الرسومات التوضيحية بالحجم الحقيقي الذي ستظهر به في المجلة. ويجب إرفاق قائمة ببرامج الحاسوب التي استعملت في كتابة النص، وأسماء الملفات على قرص مدمج، حيث يعلم القرص بالاسم الأخير للباحث، وبالرقم المرجعي للمخطوط للمراسلة، وعنوان المقالة، والتاريخ. ويحفظ في مغلف وق.



حقوق الطبع

يُشكّل تقديم مخطوط البحث للمجلة اعترافاً صريحاً من الباحثين بأن مخطوط البحث لم يُنشر ولم يُقدّم للنشر لدى أي جهة أخرى كانت وبأي صيغة ورقية أو إلكترونية أو غيرها. ويُشترط على الباحثين ملء نموذج ينصّ على نقل حقوق الطبع لتصبح ملكاً لجامعة اليرموك قبل الموافقة على نشر المخطوط. ويقوم رئيس التحرير بتزويد الباحثين بنموذج نقل حقوق الطبع مع النسخة المُرسلة للتتقيق. كما ويُمنع إعادة إنتاج أي جزء من الأعمال المنشورة في المجلة من دون إذن خطّي مُسبق من رئيس التحرير.

إخلاء المسؤولية

إن ما ورد في هذه المجلة يعبر عن آراء المؤلفين، ولا يعكس بالضرورة آراء هيئة التحرير أو الجامعة أو سياسة اللجنة العليا للبحث العلمي أو وزارة التعليم العالي والبحث العلمي. ولا يتحمل ناشر المجلة أي تبعات مادية أو معنوية أو مسؤوليات عن استعمال المعلومات المنشورة في المجلة أو سوء استعمالها.

الفهرسة: المجلة مفهرسة في:

 ULRICHSWEB™ GLOBAL SERIALS DIRECTORY	Emerging Sources Citation Index (ESCI)	
--	---	---

المجلة الأردنية للفيزياء هي مجلة بحوث علمية عالمية متخصصة مُحكمة تصدر بدعم من صندوق دعم البحث العلمي، وزارة التعليم العالي والبحث العلمي، عمان، الأردن. وتقوم بنشر المجلة عمادة البحث العلمي والدراسات العليا في جامعة اليرموك، إربد، الأردن. وتنتشر البحوث العلمية الأصلية، إضافة إلى المراسلات القصيرة Short Communications، والملاحظات الفنية Technical Notes، والمقالات الخاصة Feature Articles، ومقالات المراجعة Review Articles، في مجالات الفيزياء النظرية والتجريبية، باللغتين العربية والإنجليزية.

تقديم مخطوط البحث

تقدم البحوث عن طريق إرسالها إلى البريد الإلكتروني : jjp@yu.edu.jo

تقديم المخطوطات إلكترونياً: اتبع التعليمات في موقع المجلة على الشبكة العنكبوتية.

ويجري تحكيمُ البحوث الأصلية والمراسلات القصيرة والملاحظات الفنية من جانب مُحكمين اثنين في الأقل من ذوي الاختصاص والخبرة. وتُشجّع المجلة الباحثين على اقتراح أسماء المحكمين. أما نشر المقالات الخاصة في المجالات الفيزيائية النشطة، فيتم بدعوة من هيئة التحرير، ويُشار إليها كذلك عند النشر. ويُطلب من كاتب المقال الخاص تقديم تقرير واضح يتسم بالدقة والإيجاز عن مجال البحث تمهيداً للمقال. وتنتشر المجلة أيضاً مقالات المراجعة في الحقول الفيزيائية النشطة سريعة التغير، وتشجّع كاتبي مقالات المراجعة أو مُستكثبيها على إرسال مقترح من صفحتين إلى رئيس التحرير. ويُرفق مع البحث المكتوب باللغة العربية ملخص (Abstract) وكلمات دالة (Keywords) باللغة الإنجليزية.

ترتيب مخطوط البحث

يجب أن تتم طباعة مخطوط البحث ببنت 12 نوعه Times New Roman، وبسطر مزدوج، على وجه واحد من ورق A4 (21.6 × 27.9 سم) مع حواشي 3.71 سم، باستخدام معالج كلمات ميكروسوفت وورد 2000 أو ما استُجد منه. ويجري تنظيم أجزاء المخطوط وفق الترتيب التالي: صفحة العنوان، الملخص، رموز التصنيف (PACS)، المقدمة، طرق البحث، النتائج، المناقشة، الخلاصة، الشكر والعرفان، المراجع، الجداول، قائمة بدليل الأشكال والصور والإيضاحات، ثم الأشكال والصور والإيضاحات. وتُكتب العناوين الرئيسية بخط غامق، بينما تُكتب العناوين الفرعية بخط مائل.

صفحة العنوان: وتشمل عنوان المقالة، أسماء الباحثين الكاملة وعناوين العمل كاملة. ويكتب الباحث المسؤول عن المراسلات اسمه مشاراً إليه بنجمة، والبريد الإلكتروني الخاص به. ويجب أن يكون عنوان المقالة موجزاً وواضحاً ومعبراً عن فحوى (محتوى) المخطوط، وذلك لأهمية هذا العنوان لأغراض استرجاع المعلومات.

الملخص: المطلوب كتابة فقرة واحدة لا تزيد على مائتي كلمة، موضحة هدف البحث، والمنهج المتبع فيه والنتائج وأهم ما توصل إليه الباحثون.

الكلمات الدالة: يجب أن يلي الملخص قائمة من 4-6 كلمات دالة تعبر عن المحتوى الدقيق للمخطوط لأغراض الفهرسة.

PACS: يجب إرفاق الرموز التصنيفية، وهي متوفرة في الموقع <http://www.aip.org/pacs/pacs06/pacs06-toc.html>.

المقدمة: يجب أن توضح الهدف من الدراسة وعلاقتها بالأعمال السابقة في المجال، لا أن تكون مراجعة مكثفة لما نشر (لا تزيد المقدمة عن صفحة ونصف الصفحة مطبوعة).

طرائق البحث (التجريبية / النظرية): يجب أن تكون هذه الطرائق موضحة بتفصيل كاف لإتاحة إعادة إجرائها بكفاءة، ولكن باختصار مناسب، حتى لا تكون تكراراً للطرائق المنشورة سابقاً.

النتائج: يستحسن عرض النتائج على صورة جداول وأشكال حيثما أمكن، مع شرح قليل في النص ومن دون مناقشة تفصيلية.

المناقشة: يجب أن تكون موجزة وتركز على تفسير النتائج.

الاستنتاج: يجب أن يكون وصفاً موجزاً لأهم ما توصلت إليه الدراسة ولا يزيد عن صفحة مطبوعة واحدة.

الشكر والعرفان: الشكر والإشارة إلى مصدر المنح والدعم المالي يكتبان في فقرة واحدة تسبق المراجع مباشرة.

Jordan Journal of

PHYSICSAn International Peer-Reviewed Research Journal issued by the
Support of the Scientific Research Support Fund

Published by the Deanship of Research & Graduate Studies, Yarmouk University, Irbid, Jordan

Name: الأسم:
 Specialty: التخصص:
 Address: العنوان:
 P.O. Box: صندوق البريد:
 City & Postal Code: المدينة/الرمز البريدي:
 Country: الدولة:
 Phone: رقم الهاتف:
 Fax No: رقم الفاكس:
 E-mail: البريد الإلكتروني:
 No. of Subscription: عدد الاشتراكات:
 Method of Payment: طريقة الدفع:
 Amount Enclosed: المبلغ المرفق:
 Signature: التوقيع:

Cheques should be paid to Deanship of Research and Graduate Studies - Yarmouk University.

I would like to subscribe to the Journal
For

- ☐ One Year
☐ Two Years
☐ Three Years

One Year Subscription Rates

	Inside Jordan	Outside Jordan
Individuals	JD 8	€ 40
Students	JD 4	€ 20
Institutions	JD 12	€ 60

Correspondence**Subscriptions and Sales:**

Prof. Ibrahim O. Abu Al-Jarayesh
 Deanship of Research and Graduate Studies
 Yarmouk University
 Irbid – Jordan
Telephone: 00 962 2 711111 Ext. 2075
Fax No.: 00 962 2 721121



جامعة اليرموك



المملكة الأردنية الهاشمية

المجلة الأردنية للفيزياء

مجلة بحوث علمية عالمية متخصصة محكمة
تصدر بدعم من صندوق دعم البحث العلمي

المجلة الأردنية
للفيزياء
مجلة بحوث علمية عالمية محكمة

المجلد (13)، العدد (1)، نيسان 2020م / رمضان 1441هـ

المجلة الأردنية للفيزياء: مجلة علمية عالمية متخصصة محكمة تصدر بدعم من صندوق دعم البحث العلمي، عمان، الأردن، وتصدر عن عمادة البحث العلمي والدراسات العليا، جامعة اليرموك، إربد، الأردن.

رئيس التحرير:

ابراهيم عثمان أبو الجرايش

قسم الفيزياء، جامعة اليرموك، إربد، الأردن.

ijaraysh@yu.edu.jo

هيئة التحرير:

نبيل يوسف أيوب

رئيس الجامعة الأمريكية في مادبا، مادبا، الأردن.

nabil.ayoub@gju.edu.jo

جميل محمود خليفة

قسم الفيزياء، الجامعة الأردنية، عمان، الأردن.

jkalifa@ju.edu.jo

طارق فتحي حسين

قسم الفيزياء، الجامعة الأردنية، عمان، الأردن.

t.hussein@ju.edu.jo

مروان سليمان موسى

قسم الفيزياء، جامعة مؤتة، الكرك، الأردن.

mmousa@mutah.edu.jo

محمد خالد الصغير

قسم الفيزياء، الجامعة الهاشمية، الزرقاء، الأردن.

msugh@hu.edu.jo

عبد المجيد الياسين

قسم الفيزياء، جامعة اليرموك، إربد، الأردن.

alyassin@yu.edu.jo

محمد العمري

قسم الفيزياء، جامعة العلوم والتكنولوجيا، إربد، الأردن.

alakmoh@just.edu.jo

إبراهيم البصول

قسم الفيزياء، جامعة آل البيت، المفرق، الأردن.

Ibrahimbsoul@yahoo.com

سكرتير التحرير: مجدي الشناق

ترسل البحوث إلى العنوان التالي:

الأستاذ الدكتور إبراهيم عثمان أبو الجرايش
رئيس تحرير المجلة الأردنية للفيزياء
عمادة البحث العلمي والدراسات العليا، جامعة اليرموك
إربد، الأردن

هاتف 00 962 2 7211111 فرعي 2075

E-mail: jjp@yu.edu.jo Website: <http://Journals.yu.edu.jo/jjp>